sid.inpe.br/mtc-m21c/2020/02.11.12.10-TDI

NUMERICAL MODELING OF A HEAT PIPE TRANSIENT MODES

Cristiano Enke

Master's Dissertation of the Graduate Course in Engineering and Space Technology/Spatial Mechanics and Control, guided by Dr. Valeri Vlassov Vladimirovich, approved in February 20, 2020.

URL of the original document:
<http://urlib.net/8JMKD3MGP3W34R/3UTNQ28>

INPE
São José dos Campos
2020

PUBLISHED BY:

Instituto Nacional de Pesquisas Espaciais - INPE
Gabinete do Diretor (GBDIR)
Serviço de Informação e Documentação (SESID)
CEP 12.227-010
São José dos Campos - SP - Brasil
Tel.:(012) 3208-6923/7348
E-mail: pubtc@inpe.br

BOARD OF PUBLISHING AND PRESERVATION OF INPE INTELLECTUAL PRODUCTION - CEPPII (PORTARIA Nº 176/2018/SEI-INPE):
Chairperson:
Dra. Marley Cavalcante de Lima Moscati - Centro de Previsão de Tempo e Estudos Climáticos (CGCPT)
Members:
Dra. Carina Barros Mello - Coordenação de Laboratórios Associados (COCTE)
Dr. Alisson Dal Lago - Coordenação-Geral de Ciências Espaciais e Atmosféricas (CGCEA)
Dr. Evandro Albiach Branco - Centro de Ciência do Sistema Terrestre (COCST)
Dr. Evandro Marconi Rocco - Coordenação-Geral de Engenharia e Tecnologia Espacial (CGETE)
Dr. Hermann Johann Heinrich Kux - Coordenação-Geral de Observação da Terra (CGOBT)
Dra. Ieda Del Arco Sanches - Conselho de Pós-Graduação - (CPG)
Silvia Castro Marcelino - Serviço de Informação e Documentação (SESID)
DIGITAL LIBRARY:
Dr. Gerald Jean Francis Banon
Clayton Martins Pereira - Serviço de Informação e Documentação (SESID)
DOCUMENT REVIEW:
Simone Angélica Del Ducca Barbedo - Serviço de Informação e Documentação (SESID)
André Luis Dias Fernandes - Serviço de Informação e Documentação (SESID)
ELECTRONIC EDITING:
Ivone Martins - Serviço de Informação e Documentação (SESID)
Cauê Silva Fróes - Serviço de Informação e Documentação (SESID)

sid.inpe.br/mtc-m21c/2020/02.11.12.10-TDI

NUMERICAL MODELING OF A HEAT PIPE TRANSIENT MODES

Cristiano Enke

Master's Dissertation of the Graduate Course in Engineering and Space Technology/Spatial Mechanics and Control, guided by Dr. Valeri Vlassov Vladimirovich, approved in February 20, 2020.

URL of the original document:
<http://urlib.net/8JMKD3MGP3W34R/3UTNQ28>

INPE
São José dos Campos
2020

Cataloging in Publication Data

Enke, Cristiano.
En48n Numerical modeling of a heat pipe transient modes / Cristiano Enke. – São José dos Campos : INPE, 2020.
xxvi + 105 p. ; (sid.inpe.br/mtc-m21c/2020/02.11.12.10-TDI)

Dissertation (Master in Engineering and Space Technology/Spatial Mechanics and Control) – Instituto Nacional de Pesquisas Espaciais, São José dos Campos, 2020.
Guiding : Dr. Valeri Vlassov Vladimirovich.

1. Heat pipes. 2. Transient analysis. 3. Noncondensable gas. I.Title.

CDU 621.387:536.2

Esta obra foi licenciada sob uma Licença Creative Commons Atribuição-NãoComercial 3.0 Não Adaptada.

This work is licensed under a Creative Commons Attribution-NonCommercial 3.0 Unported License.

Aluno (a): ***Cristiano Enke***

Título: **"NUMERICAL MODELING OF A HEAT PIPE TRANSIENT MODES"**

Aprovado (a) pela Banca Examinadora em cumprimento ao requisito exigido para obtenção do Título de *Mestre* em

Engenharia e Tecnologia Espaciais/Mecânica Espacial e Controle

Dr. Rafael Lopes Costa

Presidente / INPE / São José dos Campos - SP

( ) Participação por Video - Conferência

(X) Aprovado ( ) Reprovado

Dr. Valeri Vlassov Vladimirovich

Orientador(a) / INPE / São José dos Campos - SP

( ) Participação por Video - Conferência

(V) Aprovado ( ) Reprovado

Dra. Nadjara dos Santos

Membro da Banca / INPE / São José dos Campos - SP

( ) Participação por Video - Conferência

(X) Aprovado ( ) Reprovado

Dr. Lamartine Nogueira Frutuoso Guimarães

Membro da Banca / IEAv/CTA / SJCampos - SP

( ) Participação por Video - Conferência

(X) Aprovado ( ) Reprovado

Dra. Claudia Regina de Andrade

CRAndrade

Convidado(a) / ITA/DCTA / São José dos Campos - SP

( ) Participação por Video - Conferência

(X) Aprovado ( ) Reprovado

Este trabalho foi aprovado por:

( ) maioria simples

(X) unanimidade

São José dos Campos, 20 de fevereiro de 2020

“Faz o que o teu coração manda.”

Arcanjo Lenzi

ACKNOWLEDGMENTS

To Professor Valeri Vlassov Vladimirovich, for his orientation and for his willingness to share his knowledge and advice, my eternal gratitude.

To the professors of National Institute for Space Research who with their knowledge, helped to develop this work.

To Dr. Rafael Lopes Costa who was friendly and helpful since my first day in INPE.

To Dra. Nadjara dos Santos and to Olga Viktorovna Kchoukina who helped to acoomplish the experiments of this work.

To my friends Olavo Mecias da Silva and André Caetano from the LVA – UFSC for their valuable contributions to this work.

To my friends at the UFSC, Mauricio Kubaski, Cristiano Engel, Pedro Thaines, Jonatan Feldkircher and Larissa Sirtuli who helped in some way for this work to be done.

To CAPES for the financial support.

ABSTRACT

The effect of the presence of noncondensable gas in the heat pipe was investigated experimentally and a one-dimensional numerical model was developed. The mathematical formulation includes vapor-gas compressible mixture flow conservation equations, conjugated wall, wick, and mixture energy conservation, completed with Clausius-Clapeyron saturation condition and ideal gas assumption for noncondensable gas. To solve velocity-pressure coupling a numerical iterative algorithm based on the SIMPLE method with staggered grid was used, resulting in tridiagonal matrix having an effective numerical solution. An extensive program for the model validation was performed. First, some non-trivial cases were selected from the available publications of experimental studies, like multiple heat loading and fast transients during startup and shutdown of a heat pipe with noncondensable gas. Second, some cases were performed to verify the stability of the developed algorithm under sudden changes of number and positions of heat loads and cooling zones, resulting in dynamic redistribution of mixture velocity directions and changes on noncondensable gas concentration rearrangement. Third, an experimental study was conducted in the INPE/ETE thermal laboratory following a new approach to test two identical heat pipes – one with and another without noncondensable gas, under the same conditions. This new approach has allowed improving the model precision by separate adjusting of parameters that are common for both pipes. The results of simulations show that the numerical model is capable to predict the heat pipe transient performance and behavior of noncondensable gas inside the heat pipe, including a gradual formation of vapor-gas diffusion front when heat pipe approaches steady-state condition. Due to test conditions, the presented model accounts for natural and forced convection heat sink but can be easily modified to account for orbital transient heat transfer in space applications. The high dynamic transient rise and fall of temperature at startup and shutdown was in agreement with experimental results for case with and without noncondensable gas. Moreover, the temperature change rate of the condenser proved to be more sensible to the presence of noncondensable gas than temperature itself, becoming an efficient method to detect the presence of gas inside the heat pipes when the gas presence is not desirable.

Keywords: Heat Pipes. Transient Analysis. Noncondensable Gas.

MODELAGEM NUMERICA DOS MODOS TRANSIENTES DE UM TUBO DE CALOR

RESUMO

O efeito da presença de gás não-condensável no tubo de calor foi investigado experimentalmente e um modelo numérico unidimensional de tubos de calor foi desenvolvido. A formulação matemática inclui equações de conservação do escoamento compressível da mistura vapor-gás, conservação de energia da parede, da região porosa e da mistura, incluindo com a condição de saturação de Clausius-Clapeyron e a suposição de gás ideal para o gás não-condensável. Para resolver o acoplamento velocidade-pressão, foi utilizado um algoritmo iterativo numérico baseado no método SIMPLE com grade intercalada, resultando em uma matriz tridiagonal com uma solução numérica. Foi realizado um extenso programa para a validação do modelo. Primeiro, alguns casos não triviais foram selecionados a partir das publicações disponíveis de estudos experimentais, como cargas múltiplas de calor e transientes rápidos durante a inicialização e o desligamento de um tubo de calor com gás não-condensável. Depois, alguns casos foram testados para verificar a estabilidade do algoritmo desenvolvido sob mudanças repentinas do número e das posições das cargas de calor e zonas de resfriamento, resultando em uma redistribuição dinâmica das direções e velocidade da mistura e alterações no rearranjo da concentração de gás não-condensável. Por último, um estudo experimental foi realizado no laboratório térmico do INPE/ETE, seguindo uma nova abordagem para testar dois tubos de calor idênticos - um com e outro sem gás não-condensável, nas mesmas condições. Essa nova abordagem permitiu melhorar a precisão do modelo, ajustando separadamente os parâmetros comuns aos dois tubos. Os resultados das simulações mostram que o modelo numérico é capaz de prever o desempenho do tubo e o comportamento do gás não-condensável dentro do tubo de calor, incluindo uma formação gradual da frente de difusão de vapor-gás quando o tubo de calor se aproxima da condição de estado estacionário. Devido às condições de teste, o modelo apresentado leva em consideração trocas de calor por convecção natural e forçada no dissipador de calor, mas pode ser facilmente modificado para levar em consideração a transferência de calor orbital transiente em aplicações espaciais. A altamente dinâmica elevação e a queda de temperatura na inicialização e desligamento estavam de acordo com os resultados experimentais para casos com e sem gás não-condensável. Além disso, a taxa de mudança de temperatura do condensador provou ser mais sensível à presença de gás não-condensável do que a própria temperatura, tornando-se um método eficiente para detectar a presença de gás não-condensável dentro dos tubos de calor quando a presença de gás não é desejável.

Palavras-chave: Tubos de Calor. Análise Transiente. Gás Não-condensável.

LIST OF FIGURES

Page.

Figure 2.1 – Schematics of Heat Pipe. 5
Figure 2.2 – Operational Limits of a Conventional Heat Pipe. 7
Figure 2.3 – Operational Limits of an Aluminum Ammonia Heat Pipe. 10
Figure 2.4 – Noncondensable Gas Location. 11
Figure 2.5 – Bowman’s Porous Pipe. 14
Figure 2.6 – Vapor Flow Patterns of Issacci’s Model. 14
Figure 2.7 – Mesh Representation of Faghri’s Model. 15
Figure 2.8 – Meniscus and Pool Formation on THROHPUT Code. 15
Figure 2.9 – Liquid Pool Formation on HPTAM Code. 16
Figure 2.10 – Gas Loaded Heat Pipe and Temperature Distribution. 16
Figure 2.11 – Axial Mass Distribution of Rohani and Tien’s Model. 17
Figure 2.12 – Vapor-Gas Dynamics for a High Temperature Heat Pipe. 17
Figure 3.1 – Wall, Wick and Mixture Nodes Representation. 19
Figure 3.2 – Heating Block and Heater Nodes Representation. 24
Figure 3.3 – Flow Chart of Algorithm. 30
Figure 3.4 – The staggered grid. 31
Figure 3.5 – Flow Chart of SIMPLE Algorithm. 34
Figure 4.1 – Experimental Apparatus. 37
Figure 4.2 – Heat Loads Location for Case with One Heat Load. 38
Figure 4.3 – Wall Temperature versus Time for the Case with One Heat Load. 39
Figure 4.4 – Temperatures Along Heat Pipe Axis for the Case with One Heat Load. 40
Figure 4.5 – Vapor Velocity Along Axis for the Case with One Heat Load. 40
Figure 4.6 – Mass Flux Along Axis for the Case with One Heat Load. 41
Figure 4.7 – Heat Loads Location for the Case with Two Heat Loads. 42
Figure 4.8 – Time Dependent Wall Temperatures for the Case with Two Heat Loads. 42
Figure 4.9 – Temperatures Along Axis for the Case with Two Heat Loads. 43
Figure 4.10 – Vapor Velocity Along Axis for the Case with Two Heat Loads. 44
Figure 4.11 – Mass Flux Along Axis for the Case with Two Heat Loads. 44
Figure 4.12 – Cross-section of the Heat Pipe Loaded with Noncondensable Gas. ... 45
Figure 4.13 – Time Dependend Temperature of Wall With Noncondensable Gas. 46
Figure 4.14 – Temperature distribution along axis for selected times. 47
Figure 4.15 – Representation of Heat Load Locations for Symmetry Test. 49
Figure 4.16 – Wall Temperature and Axial Velocity Along Axis for Cases 1 and 2.... 50
Figure 4.17 – Vapor and Gas Distribution Along Axis for Cases 1 and 2. 50
Figure 4.18 – Wall Temperature and Axial Velocity Along Axis for Case 3. 51
Figure 4.19 – Vapor and Gas Distribution Along Axis for Case 3. 52
Figure 4.20 – Wall Temperature and Axial Velocity Along Axis for Case 4. 53
Figure 4.21 – Vapor and Gas Distribution Along Axis for Case 4. 53
Figure 4.22 – Wall Temperature and Axial Velocity Along Axis for Cases 5 and 6.... 54
Figure 4.23 – Vapor and Gas Distribution Along Axis for Cases 5 and 6. 55
Figure 4.24 – Wall Temperature and Axial Velocity Along Axis for the Cases 7 and 8. 56
Figure 4.25 – Vapor and Gas Distribution Along Axis for Cases 7 and 8. 56

Figure 4.26 – Wall Temperature and Axial Velocity Along Axis for the Cases 7 and 8. 57
Figure 4.27 – Vapor and Gas Distribution Along Axis for Cases 7 and 8. 57
Figure 4.28 – Wall Temperature and Axial Velocity Along Axis for Case 9. 58
Figure 4.29 – Vapor and Gas Distribution Along Axis for Case 9. 58
Figure 5.1 – Heat Pipe Cross-Section Profile. 59
Figure 5.2 – Thermocouple Locations. 60
Figure 5.3 – Heating Block. 60
Figure 5.4 – Heating Block Location. 60
Figure 5.5 – Power Source Tectrol TCA 120-20. 61
Figure 5.6 – Data Acquisition System. 61
Figure 5.7 – Experimental Diagram. 62
Figure 5.8 – View of the Experimental Setup. 62
Figure 6.1 – Representation of Heat Load Locations for Experimental Setup. 65
Figure 6.2 – Representation of Experimental Setup With Heat Load of 75 W Cooled by Natural and Forced Convection Without Noncondensable Gas. 66
Figure 6.3 – Experimental and Numerical Time Depentent Wall Temperatures and Temperature Distribution Along Axis for Selected Times. 67
Figure 6.4 – Vapor Distribution Along Axis for Selected Times. 67
Figure 6.5 – Axial Velocity and Evaporation/Condensation Mass Rate Along Axis for Selected Times. 68
Figure 6.6 – Experimental and Numerical Time Depentent Wall Temperatures and Temperature Distribution Along Axis for Selected Times. 69
Figure 6.7 – Experimental and Numerical Outer Wall Distribution Along Axis for Selected Times. 69
Figure 6.8 – Axial Velocity and Evaporation/Condensation Mass Rate Along Axis for Selected Times. 70
Figure 6.9 – Representation of Experimental Setup With Heat Load of 75 W Cooled by Natural and Forced Convection With Noncondensable Gas. 70
Figure 6.10 – Experimental and Numerical Time Depentent Wall Temperatures and Temperature Distribution Along Axis for Selected Times. 71
Figure 6.11 – Vapor and Noncondensable Gas Distribution Along Axis for Selected Times. 71
Figure 6.12 – Axial Velocity and Evaporation/Condensation Mass Rate Along Axis for Selected Times. 72
Figure 6.13 – Experimental and Numerical Time Depentent Wall Temperatures and Temperature Distribution Along Axis for Selected Times. 73
Figure 6.14 – Vapor and Noncondensable Gas Distribution Along Axis for Selected Times. 73
Figure 6.15 – Axial Velocity and Evaporation/Condensation Mass Rate Along Axis for Selected Times. 74
Figure 6.16 – Representation of Experimental Setup With Heat Load of 25 W Cooled by Natural and Forced Convection Without Noncondensable Gas. 74
Figure 6.17 – Experimental and Numerical Time Depentent Wall Temperatures and Temperature Distribution Along Axis for Selected Times. 75
Figure 6.18 – Axial Velocity and Evaporation/Condensation Mass Rate Along Axis for Selected Times. 75
Figure 6.19 – Experimental and Numerical Time Depentent Wall Temperatures and Temperature Distribution Along Axis for Selected Times. 76

Figure 6.20 – Experimental and Numerical Temperature Distribution Along Axis for Selected Times......77
Figure 6.21 – Axial Velocity and Evaporation/Condensation Mass Rate Along Axis for Selected Times......77
Figure 6.22 – Representation of Experimental Setup With Heat Load of 25 W Cooled by Natural and Forced Convection With Noncondensable Gas......78
Figure 6.23 – Experimental and Numerical Time Depentent Wall Temperatures and Temperature Distribution Along Axis for Selected Times. 78
Figure 6.24 – Vapor and Noncondensable Gas Distribution Along Axis for Selected Times. 79
Figure 6.25 – Axial Velocity and Evaporation/Condensation Mass Rate Along Axis for Selected Times......79
Figure 6.26 – Experimental and Numerical Time Depentent Wall Temperatures and Temperature Distribution Along Axis for Selected Times. 80
Figure 6.27 – Vapor and Noncondensable Gas Distribution Along Axis for Selected Times. 80
Figure 6.28 – Axial Velocity and Evaporation/Condensation Mass Rate Along Axis for Selected Times......81
Figure 6.29 – Representation of Experimental Setup With Heat Load of 25 W Cooled by Natural Convection Without Noncondensable Gas......81
Figure 6.30 – Experimental and Numerical Time Depentent Wall Temperatures and Temperature Distribution Along Axis for Selected Times. 82
Figure 6.31 – Vapor Distribution Along Axis for Selected Times. 82
Figure 6.32 – Axial Velocity and Evaporation/Condensation Mass Rate Along Axis for Selected Times......83
Figure 6.33 – Experimental and Numerical Time Depentent Wall Temperatures and Temperature Distribution Along Axis for Selected Times. 84
Figure 6.34 – Vapor Distribution Along Axis for Selected Times. 84
Figure 6.35 – Axial Velocity and Evaporation/Condensation Mass Rate Along Axis for Selected Times......85
Figure 6.36 – Representation of Experimental Setup With Heat Load of 25 W Cooled by Natural Convection With Noncondensable Gas......85
Figure 6.37 – Experimental Numerical Time Depentent Wall Temperatures and Temperature Distribution Along Axis for Selected Times. 86
Figure 6.38 – Vapor and Noncondensable Gas Distribution Along Axis for Selected Times. 86
Figure 6.39 – Axial Velocity and Evaporation/Condensation Mass Rate Along Axis for Selected Times......87
Figure 6.40 – Experimental and Numerical Time Depentent Wall Temperatures and Temperature Distribution Along Axis for Selected Times. 88
Figure 6.41 – Vapor and Noncondensable Gas Distribution Along Axis for Selected Times. 88
Figure 6.42 – Axial Velocity and Evaporation/Condensation Mass Rate Along Axis for Selected Times......89
Figure A.1 – Temperature Change Rate of the Long Run Test, cooled by Forced Convection, with Heat Load of 75 W. 98
Figure A.2 – Temperature Change Rate of the Short Run Test, cooled by Forced Convection, with Heat Load of 75 W. 98
Figure A.3 – Temperature Change Rate of the Long Run Test, cooled by Forced Convection, with Heat Load of 25 W. 99

Figure A.4 – Temperature Change Rate of the Short Run Test, cooled by Forced Convection, with Heat Load of 25 W. 100
Figure A.5 – Temperature Change Rate of the Long Run Test, cooled by Natural Convection, with Heat Load of 25 W. 101
Figure A.6 – Temperature Change Rate of the Short Run Test, cooled by Natural Convection, with Heat Load of 25 W. 101

LIST OF TABLES

Page.

Table 3.1 – Correlation Used on Each Side of Pipe. 28
Table 4.1 – Values of heat transfer coefficients used in numerical tests with one and two heat sources. 38
Table 4.2 – Values of heat transfer coefficients used in numerical tests with noncondensable gas. 46
Table 4.3 – Location of Evaporator and Condenser Nodes of Symmetry Test. 48
Table 6.1 – Performed Combinations of Experimental Test Setups. 66
Table 6.2 – Values of heat transfer coefficients used in numerical models with 75W cooled by natural and forced convection. 68
Table 6.3 – Values of heat transfer coefficients used in numerical models with 25W cooled by natural and forced convection. 76
Table 6.4 – Values of heat transfer coefficients used in numerical models with 25W cooled by natural convection. 83
Table A.1 – Values of maximum of temperature change for long period tests. 102
Table A.2 – Values of maximum of temperature change for short period tests. 102

LIST OF SYMBOLS

[Latin Symbols]

A_b	Surface Area of Polymer Block $[m^2]$
$A_{contact}$	Contact Area Between Solid and Liquid $[m^2]$
A_{vap}	Cross-sectional Area of Vapor Space $[m^2]$
$A_{h,b}$	Heat Exchange Area Between Heater and Polymer Block $[m^2]$
$A_{h,w}$	Heat Exchange Area Between Heater and Wall $[m^2]$
A_{wick}	Cross-sectional Area of Wick $[m^2]$
A_w	Cross-sectional Area of Wall $[m^2]$
$A_{wick,v}$	Heat Exchange Area Between Wick and Vapor $[m^2]$
$A_{wick,w}$	Heat Exchange Area Between Wick and Wall $[m^2]$
B_{up}	Characteristic Length of the upper side of the Tube $[m]$
B_{down}	Characteristic Length of the bottom side Tube $[m]$
B_{side}	Characteristic Length of the Tube $[m]$
B_1	Constant Characteristic of The Corrosion Process
B_2	Constant Represent a Barrier Between Molecules on The Catalytic Surface
$\bar{C}_p$	Specific Heat at Constant Pressure of Mixture $[J/kgK]$
$C_{p,b}$	Specific Heat at Constant Pressure of Polymer Block $[J/kgK]$
$C_{p,h}$	Specific Heat at Constant Pressure of Heater $[J/kgK]$
$C_{p,w}$	Specific Heat at Constant Pressure of Wall $[J/kgK]$
$C_{p,NCG}$	Specific Heat at Constant Pressure of Noncondensable Gas $[J/kgK]$
$C_{p,v}$	Specific Heat at Constant Pressure of Vapor $[J/kgK]$
D_{vg}	Mass Diffusion Coefficient Between Vapor and Gas $[m^2/s]$
D_v	Vapor Channel Diameter $[m]$
E_1	Activation Energy of The Process $[J]$
E_2	Activation Energy of The Process $[J]$
f	Friction Coefficient
F_l	Friction Coefficient for Liquid
F_v	Friction Coefficient for Vapor
g	Acceleration of Gravity $[m/s^2]$
h_{amb}	Heat Transfer Coefficient between Ambient and Wall $[W/m^2K]$

$h_{evap/cond}$	Heat Transfer Coefficient between Wick and Vapor $[W/m^2K]$
$h_{h,b}$	Heat Transfer Coefficient between Heater and Block $[W/m^2K]$
$h_{h,w}$	Heat Transfer Coefficient between Heater and Wall $[W/m^2K]$
h_f	Forced Convection Heat Transfer Coefficient $[W/m^2K]$
h_{nat}	Natural Convection Heat Transfer Coefficient $[W/m^2K]$
$h_{wick,w}$	Heat Transfer Coefficient between Wick and Wall $[W/m^2K]$
j_v	Vapor Mass Flux $[kg/m^2s]$
$\bar{k}$	Thermal Conductivity of Mixture$[W/mK]$
k_{air}	Thermal Conductivity of Air $[W/mK]$
k_b	Thermal Conductivity of Polymer Block $[W/mK]$
k_v	Thermal Conductivity of Vapor $[W/mK]$
k_{NCG}	Thermal Conductivity of Noncondensable Gas $[W/mK]$
k_{eff}	Effective Thermal Conductivity of Wick Structure $[W/mK]$
k_B	Boltzmann’s Constant $[J/K]$
k_w	Thermal Conductivity of Wall $[W/mK]$
k_l	Thermal Conductivity of Liquid Phase of Wick $[W/mK]$
k_s	Thermal Conductivity of Solid Phase of Wick $[W/mK]$
K	Permeability $[m^2]$
L_a	Length of the Adiabatic Section $[m]$
L_c	Length of the Condenser Section $[m]$
L_e	Length of the Evaporator Section $[m]$
L_{eff}	Effective Length of Heat Pipe $[m]$
L_{HP}	Length of Heat Pipe $[m]$
m_{NCG}	Mass of Noncondensable Gas $[kg]$
M_g	Molar Mass of Noncondensable Gas $[g/mol]$
M_v	Molar Mass of Vapor $[g/mol]$
n	Number of Moles
Nu_f	Nusselt Number for Forced Convection
Nu_B	Nusselt Number for Characteristic Length B
p	Pressure $[Pa]$
p^*	Guess Pressure $[Pa]$
p'	Correction Pressure $[Pa]$
p_c	Capillary Pressure $[Pa]$

p_{NCG}	Pressure of Noncondensable Gas $[Pa]$
p_{stag}	Stagnation Pressure $[Pa]$
p_v	Pressure of Vapor $[Pa]$
$\bar{p}$	Mixture Pressure $[Pa]$
Pr	Prandtl Number
q	Heat Flux $[W/m^2]$
$q_{w,in}$	Heat Flux at Wall $[W/m^2]$
$q_{wick,in}$	Heat Flux at Wick $[W/m^2]$
$q_{b,in}$	Heat Flux at Polymer Block $[W/m^2]$
q_h	Heat Flux from Power Source $[W/m^2]$
$q_{h,in}$	Heat Flux at Heater $[W/m^2]$
$Q_{b,max}$	Maximum Heat Transfer Rate on Boiling Limit $[W]$
$Q_{c,max}$	Maximum Heat Transfer Rate on Capillary Limit $[W]$
$Q_{e,max}$	Maximum Heat Transfer Rate on Entrainment Limit $[W]$
$Q_{s,max}$	Maximum Heat Transfer Rate on Sonic Limit $[W]$
$Q_{v,max}$	Maximum Heat Transfer Rate on Viscous Limit $[W]$
Q_{in}	Heat Input from Wick to Vapor $[W]$
r_{eff}	Effective Radius of Wick Structure $[m]$
r_i	Inner Radius of Pipe $[m]$
$r_{h,wick}$	Hydraulic Radius of Wick Structure $[m]$
r_n	Boiling Nucleation Radius $[m]$
r_v	Vapor Core Radius $[m]$
R_{NCG}	Gas Constant of Noncondensable Gas $[J/kgK]$
R_v	Gas Constant of Vapor $[J/kgK]$
Ra	Rayleigh Number
Re	Reynolds Number
X	Concentration of Noncondensable Gas in Mixture
t	Time $[s]$
t_{hours}	Time $[hours]$
T	Temperature $[K]$
T_{amb}	Ambient Temperature$[K]$
T_b	Temperature of Polymer Block $[K]$
T_h	Temperature of Heater $[K]$

T_s	Temperature of Surface $[K]$
T_{stag}	Stagnation Temperature $[K]$
T_{mix}	Temperature of Mixture $[K]$
T_v	Temperature of Vapor $[K]$
T_w	Temperature of Wall $[K]$
T_{wick}	Temperature of Wick Structure $[K]$
u	Velocity in Axial Direction $[m/s]$
u^*	Guess Velocity $[m/s]$
u'	Correction Velocity $[m/s]$
v	Velocity in Radial Direction $[m/s]$
y	Coordinate along y axis $[m]$
z	Coordinate along z axis $[m]$

[Greek Symbols]

α	Thermal Diffusivity $[m^2/s]$
α_{num}	Underrelaxation Factor of Numeric Model
β	Thermal Expansion Coefficient $[1/K]$
γ_v	Ratio of Specific Heats of Vapor
δ_b	Thickness of Polymer Block $[m]$
δ_h	Thickness of Heater $[m]$
δ_w	Thickness of Wall $[m]$
δ_{wick}	Thickness of Wick and Wall Centerlines $[m]$
$\delta_{wick,w}$	Distance of Wick and Wall Centerlines $[m]$
ε	Porosity
λ	Latent Heat of Evaporation $[J/kg]$
μ	Dynamic Viscosity $[Pa.s]$
μ_l	Dynamic Viscosity of Liquid $[Pa.s]$
μ_{NCG}	Dynamic Viscosity of Noncondensable Gas $[Pa.s]$
μ_v	Dynamic Viscosity of Vapor $[Pa.s]$
$\bar{\mu}$	Dynamic Viscosity of Mixture $[Pa.s]$
ν	Kinematic Viscosity $[m^2/s]$
ρ	Density $[kg/m^3]$
ρ_b	Density of Polymer Block $[kg/m^3]$

ρ_h	Density of Heater $[kg/m^3]$
ρ_l	Density of Liquid $[kg/m^3]$
ρ_v	Density of Vapor $[kg/m^3]$
ρ_w	Density of Wall $[kg/m^3]$
ρ_{NCG}	Density of Noncondensable Gas $[kg/m^3]$
$\bar{\rho}$	Density of Mixture $[kg/m^3]$
σ	Surface Tension of Working Fluid $[N/m]$
σ_{vg}	Collision Diameter of Species $[\text{Å}]$
ϕ	Scalar Variable
Ω_{vg}	Collision Integral

[Special Symbols and Constructs]

$(\rho C_p)_l$	Volumetric Specific Heat of Liquid at Constant Pressure $[J/m^3K]$
$(\rho C_p)_s$	Volumetric Specific Heat of Solid at Constant Pressure $[J/m^3K]$
$(\rho C_p)_{wick}$	Volumetric Specific Heat of Wick at Constant Pressure $[J/m^3K]$
Δp_l	Variation in the Pressure of Liquid $[Pa]$
Δp_v	Variation in the Pressure of Vapor $[Pa]$
$\frac{d}{dz}$	Operator for the first derivative with respect to coordinate z
$\frac{\partial}{\partial t}$	Operator for the first partial derivative with respect to time
$\frac{\partial}{\partial z}$	Operator for the first partial derivative with respect to coordinate z
$\frac{\partial^2}{\partial z^2}$	Operator for the second partial derivative with respect to coordinate z
$ln(\cdot)$	Natural Logarithm of argument
$[a]$	Main Diagonal of Matrix in TDMA
$[b]$	Diagonal Below Main Diagonal of Matrix in TDMA
$[c]$	Diagonal Above Main Diagonal of Matrix in TDMA
$[d]$	Column Vector in TDMA
$[x]$	Column Vector with x in TDMA
i	Vector Index

TABLE OF CONTENTS

Page.

1 INTRODUCTION 1
1.1 Problem definition 1
1.2 General objectives 2
1.3 Specific objectives 3
1.4 Structure of document 3
2 LITERATURE REVIEW 5
2.1 Heat pipes operation principles 5
2.2 Startup and shutdown of heat pipes 5
2.2.1 Startup 5
2.2.2 Shutdown 6
2.3 Heat pipe operational limits 6
2.3.1 Viscous limit 7
2.3.2 Sonic limit 7
2.3.3 Entrainment limit 8
2.3.4 Capillary limit 8
2.3.5 Boiling limit 9
2.4 Noncondensable gas formation and effect on heat pipes 10
2.5 Noncondensable gas detection methods 12
2.5.1 Steady-state method 13
2.5.2 Transient method 13
2.6 Previous mathematical models of heat pipes 14
2.7 Previous mathematical models of heat pipes with noncondensable gas 16
3 MATHEMATICAL AND NUMERICAL MODEL 19
3.1 Transient 1D mathematical model of heat pipe 19
3.1.1 Mixture flow model 19
3.1.2 Wall and wick model 23
3.1.3 Heating block and heater model 24
3.2 Starting and boundary conditions 26
3.3 Heat transfer and diffusion coefficients 27
3.3.1 External heat transfer coefficients 27
3.3.2 Internal heat transfer coefficients 29
3.3.3 Diffusion coefficients 29
3.4 Numerical modeling 30
3.5 The staggered grid method 31
3.6 The SIMPLE method 31
3.7 Tridiagonal matrix algorithm 34
4 MODEL VALIDATION 37
4.1 Validation 1: multiple heat sources 37
4.1.1 Case with one heat load 38
4.1.2 Case with two heat loads 41
4.2 Validation 2: evaluation of the presence of noncondensable gas 45
4.3 Validation 3: symmetry test of numerical model 47
4.3.1 Symmetry test of cases 1 and 2 50
4.3.2 Symmetry test of case 3 51
4.3.3 Symmetry test of case 4 52

4.3.4 Symmetry test of cases 5 and 6 54
4.3.5 Symmetry test of cases 7 and 8 55
4.3.6 Symmetry test of case 9 57
5 EXPERIMENTAL SETUP 59
5.1 Heat pipe characteristics 59
5.2 Experimental setup 59
5.3 Experimental setup error analysis 62
6 RESULTS AND DISCUSSION 65
6.1 Experimental and numerical results comparison 65
6.1.1 Long run test without NCG, cooled by natural and forced convection, with 75 W applied to the heater. 66
6.1.2 Short run test without NCG, cooled by natural and forced convection, with 75 W applied to the heater. 68
6.1.3 Long Run Test with NCG, cooled by Natural and Forced Convection, with 75 W Applied to the Heater. 70
6.1.4 Short run test with NCG, cooled by natural and forced convection, with 75 W applied to the heater. 72
6.1.5 Long run test without NCG, cooled by natural and forced convection, with 25 W applied to the heater. 74
6.1.6 Short run test without NCG, cooled by natural and forced convection, with 25 W applied to the heater. 76
6.1.7 Long run test with NCG, cooled by natural and forced convection, with 25 W applied to the heater. 77
6.1.8 Short run test with NCG, cooled by natural and forced convection, with 25 W applied to the heater 80
6.1.9 Long run test without NCG, cooled by natural convection only, with 25 W applied to the heater. 81
6.1.10 Short run test without NCG, cooled by natural convection, with 25 W applied to the heater 83
6.1.11 Long run test with NCG, cooled by natural convection, with 25 W applied to the heater 85
6.1.12 Short run test with NCG, cooled by natural convection, with 25 W applied to the heater 87
7 CONCLUSIONS 91
7.1 Future work 91
REFERENCES 93
APPENDIX A: TEMPERATURE CHANGE RATES 97
APPENDIX B: CALCULATION OF HEAT TRANSFER COEFFICIENTS 103

1 INTRODUCTION

A heat pipe is a device used to transport heat between two interfaces along a certain distance with high efficiency. Gaugler (1944) conceived the principle of the heat pipe, but its applications and effectiveness were proved by Grover and his colleagues from Los Alamos Scientific Laboratory (GROVER et al. 1964).

In its conventional and simplest form, a heat pipe is composed by a closed tube with its inner surfaces lined with a porous material or capillary wick. The wick structure is saturated with liquid and the remaining volume contains the vapor phase of a working fluid.

Being in saturated equilibrium with its phases, the working fluid evaporates promptly even under small temperature rises that eventually occurs in any zone along the heat pipe length. Vapor velocity flows to colder zones where it condenses. A huge amount of latent heat of phase transition of the working fluid results in that even a small magnitude of vapor mass flow rate is enough to transport a relatively high amount of heat. It results that even a relatively small capillary force of the wettable porous structure is enough to provide the return of the liquid phase to the evaporation zones. This is the principal internal mechanism that makes the heat pipe be an ideal device for thermal stabilization and heat transport to a certain distance. Gravity may affect the capillary action, therefore the heat pie is an ideal device for space zero gravity applications.

Different factors may limit the maximum heat transfer rate in heat pipes. One of the problems that can cause a reduction in performance of a heat pipe is the generation of noncondensable gas along the heat pipe lifetime, which is especially important to be considered and predicted for long-term orbital missions or for long periods of mounted tubes storage.

1.1 Problem definition

The generation of noncondensable gas in heat pipes can cause a reduction in the effective length of the condenser due to concentration of the gas at the end of the condenser zone, but there is a lack of understanding on how the mixture with vapor behave during fast transient modes, including startup and shutdown. There are also technical issues involving the indirect detection of noncondensable gas through temperature measurements because it is difficult to detect the exact location of the front vapor-gas position with a limited number of temperature sensors. In separate heat pipes, the usual approach is to perform a laboratory test in steady-state condition with multiple temperature sensors installed along the heat pipe length. Then, the obtained temperature gradient curve along the length shall be analyzed and the eventual temperature distortions may indicate a noncondensable gas presence.

In practical applications, there are problems related to difficulty to access some parts of the heat pipe when it is already inserted into satellite’s panels. After the heat pipe being inserted inside the satellite panel, and satellite equipment be mounted, there is no way to directly access the heat pipe without effectively dismounting part of the panel. These characteristics turn very impractical almost any usual temperature gradient direct steady-state test to be performed on heat pipes embedded to satellite panels. A new methodology shall be developed, based on transient sort period tests and few number of available temperature sensors installed on the heat pipe.

In numerical models, heat pipes are usually simulated with a canonical application of heat load and heat sink is usually applied to the heat pipes, with the heat load being applied to the left side of the pipe becoming the evaporator section, and the heat sink applied to the right side of the pipe becoming the condenser section. But in real applications, the heat pipe must work under a heat load and heat sink at any location of the pipe.

1.2 General objectives

The main objective of the study aims to create a transient one-dimensional mathematical model capable to account non-canonical heat load application, multiple and eventual heat loads and losses along a heat pipe. Furthermore, the model will be able to predict the behavior of this pipe with or without the presence of noncondensable gas at the vapor channel. The model shall be numerically stable and representative, allowing to simulate fast transient processes during startup and shutdown and to simulate the dynamics of vapor-gas concentration redistribution during fast transient processes.

1.3 Specific objectives

This work has the following specific objectives:

a) Develop a mathematical model, capable to simulate a heat pipe with all its characteristics, including heat transfer through the wall and wick, eventual evaporation and condensation process. flow development through the vapor core under changeable direction in accordance to possible sudden changes of external heating or cooling conditions.

b) Develop an enhanced version of the model to tackle the presence of noncondensable gas inside the heat pipe in different concentrations. The model shall be able to simulate any interaction between vapor and gas, including the formation of internal vapor-gas diffusion barriers under changeable or steady-state external conditions, which may reflect in changing the thermal characteristics of the heat pipe.

c) Perform several numerical tests in order to validate the robustness of the model in many different simulated conditions as well as perform model validation through comparison with available published data.

d) Conduct experimental laboratory tests with two identical heat pipes – one with and one without noncondensable gas, to provide enough data to validate the model.

e) Model the experimental tests and compare numerical and experimental data.

1.4 Structure of document

This document is divided into several chapters:

Chapter 1: Introduction, where is presented the context of the problem, and the objectives of this work.

Chapter 2: Literature Review, where is introduced the principles of functioning of heat pipes, generation and detection methods of noncondensable gas, and a review on heat pipe modeling.

Chapter 3: Mathematical and Numerical Model, where is showed the governing equations for phenomena in a conventional heat pipe and is presented a method to couple velocity and pressure. A computational routine to solve tridiagonal systems of equations is also presented.

Chapter 4: Model Validation, where is presented a comparison of results obtained with the present model and two different experiments from literature. It is also presented qualitative results of various symmetry tests.

Chapter 5: Experimental Setup, where is presented how the experiment was done and how the experimental results were obtained.

Chapter 6: Results and Discussion, the results of experiments performed with different power inputs and the presence or absence of noncondensable gas are presented together with results of the numerical model.

Chapter 7: Conclusions obtained and proposals for future works.

References, where is presented the literature cited in this work.

Appendix A: Temperature Changing Rates, where is presented additional results obtained from experimental data.

Appendix B: Calculation of Heat Transfer Coefficients, where is presented an example of how the heat transfer coefficients were calculated in the numerical simulations.

2 LITERATURE REVIEW

This chapter will present a literature review about the functioning principles of conventional heat pipes, the noncondensable gas generation mechanisms, and finally some previous works in heat pipe modeling.

2.1 Heat pipes operation principles

When a heat load is applied at any zone of the pipe by an external heat source, it vaporizes the working fluid at that section, which will operate as an evaporator. This additional vapor generates a difference in pressure at the core of the pipe driving vapor from evaporator to the condenser zone where the vapor condenses and releases the latent heat of vaporization to a heat sink. When liquid is depleted by evaporation at evaporator zone, a capillary pressure is developed there. This capillary pressure pumps the condensed liquid back from the condenser to the evaporator. This dynamics can be seen in Figure 2.1, and it continues while the heating and cooling conditions are kept or as long as the flow passage of the fluid is not blocked and a sufficient capillary pressure is developed. (CHI, 1976).

Figure 2.1 – Schematics of Heat Pipe.

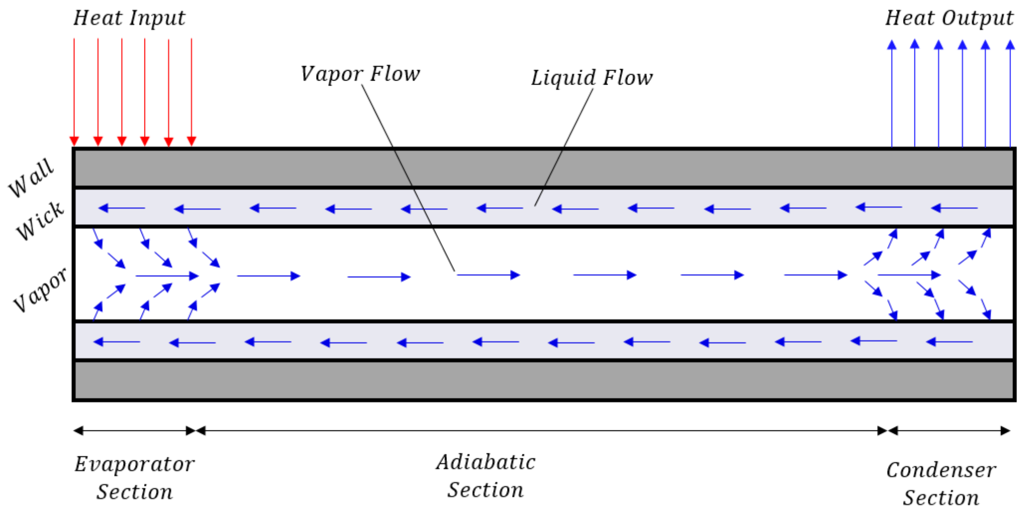

Components and principle of operation of a conventional heat pipe.
Source: Adapted from Chi (1976).

2.2 Startup and shutdown of heat pipes

2.2.1 Startup

For a heat pipe, the startup is characterized as the transient between a state where the pipe is in equilibrium in temperature with ambient to a state where it reaches a constant flux of heat, which is the steady-state operation. The steady-state is only reached if external conditions applied to the heat pipe do not change.

When a heat load is applied to the pipe, in first instant a difference in temperature appears, so there is an increase in evaporator temperature, than evaporation occurs at this section. The new mass of vapor added to the vapor core creates a pressure difference, which drives vapor from the evaporator to the condenser section that is at lower temperature compared with the evaporator thus causing condensation of vapor.

That difference in the temperature along the length of the heat pipe can be caused by heating of a region of the heat pipe, by cooling of a region of the heat pipe, or by a combination of these events.

In some circumstances, the startup may not be successful, for example due to very high initial heat flux density on the evaporator or due to very low initial temperature over the tube.

2.2.2 Shutdown

Under steady-state conditions, there is a constant temperature difference between evaporator and condenser sections. At shutdown, this temperature difference gradually decreases until the entire heat pipe reaches same temperature.

The process of shutdown can occur when the heat source is turned off. After this event, the heat pipe works with lower temperature differences until it reaches ambient temperature. However, this process can also occur when the temperature of condenser is increased until it reaches the same temperature as evaporator. With both ends at same temperature, there is no pressure difference along the axis and consequently, there is no heat flux through the pipe.

2.3 Heat pipe operational limits

With high effective thermal conductivity, a heat pipe is a very efficient heat transfer device, even though it is subject to some heat transfer limitations. Under particular conditions, these limitations can determine the maximum heat transfer rate that a particular heat pipe can achieve. The operational limits are usually evaluated as how much heat rate a heat pipe can transport for a given working temperature. A qualitative graph of the usual operational limits of a heat pipe is shown in Figure 2.2.

Figure 2.2 – Operational Limits of a Conventional Heat Pipe.

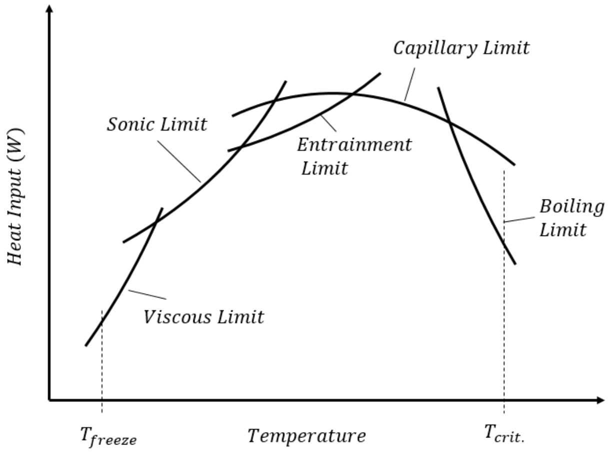

Operational limits of a conventional heat pipe.
Source: Adapted from Faghri (1995).

2.3.1 Viscous limit

Viscous limit is achieved when viscous forces dominate the vapor flow, which occurs usually when working conditions become closer to the freezing temperature of working fluid. The expression for maximum axial heat rate $Q_{v,max}$ through the vapor core is shown by (FAGHRI, 1995):

$$Q_{v,max} = \frac{A_{vap} D_v^2 \lambda \rho_v p_v}{64 \mu_v L_{eff}}, \tag{2.1}$$

where A_{vap} is the area of vapor space, D_v is the diameter of vapor space, λ is the latent heat of evaporation, ρ_v is the vapor density, p_v is the vapor pressure, μ_v is the vapor dynamic viscosity and L_{eff} is the effective length of heat pipe defined as:

$$L_{eff} = 0.5\, L_e + L_a + 0.5\, L_c, \tag{2.2}$$

in which L_e is the length of evaporator, L_a is the length of adiabatic zone (if existent) and L_c is the length of condenser.

2.3.2 Sonic limit

Sonic limitation is generally achieved when a heat pipe operates at low vapor densities and/or high vapor velocities. It is a problem especially in heat pipes with liquid metal as working fluid, in which vapor can reach sonic velocity due to typical high heat loads, wich is velocities above the speed of sound for the given temperatures. Chi (1976), shows an expression to the maximum heat transfer rate on sonic limit $Q_{s,max}$:

$$Q_{s,max} = A_{vap}\rho_v\lambda\left(\frac{\gamma_v R_v T_v}{2(\gamma_v + 1)}\right)^{1/2}, \tag{2.3}$$

where A_{vap} is the area of vapor space, ρ_v is the vapor density, λ is the latent heat of evaporation, γ_v is the ratio of specific heats of vapor, R_v is gas constant of vapor, and T_v is the vapor temperature.

2.3.3 Entrainment limit

The entrainment limit can occur when vapor flow reaches a sufficient high velocity. Inside a heat pipe, liquid and vapor flows have opposite directions, so when vapor velocity is sufficiently high, the shear force can pull out small drops of liquid to the vapor flow. This phenomenon prevents liquid to return from condenser to evaporator, leading to a limitation on the transport capability of heat pipe. The maximum heat transfer rate on entrainment limit $Q_{e,max}$ is given by Chi (1976):

$$Q_{e,max} = A_{vap}\lambda\left(\frac{\sigma\rho_v}{2r_{h,wick}}\right)^{1/2}, \tag{2.4}$$

where A_{vap} is the area of vapor space, λ is the latent heat of evaporation, σ is the surface tension of fluid, ρ_v is the vapor density, and $r_{h,wick}$ is the hydraulic radius of wick structure at its interface surface.

2.3.4 Capillary limit

There is a maximum value of pumping ability of the capillary structure for any pair of liquid-wick combination, so if the evaporation rates are higher than the capability of the given wick replenishment capability, a dry-out of wick may happened due to a lack of liquid phase supplement. Moreover, for a heat pipe operating under a gravitational field, maximum transport of fluid can be smaller for a pipe inclined under unfavorable conditions (condenser lower than evaporator) or higher for a pipe inclined under favorable conditions (evaporator lower than condenser). An expression for capillary limitation on the heat transport factor $(QL_{eff})_{c,max}$ is showed by Faghri (1995):

$$(QL_{eff})_{c,max} \leq \frac{2\sigma/r_{eff} - \rho_l g L_{HP} sin\phi}{F_l + F_v}, \tag{2.5}$$

in which F_l and F_v are friction coefficients for liquid and vapor respectively defined as:

$$F_l = \frac{\mu_l}{\rho_l A_{wick} K \lambda}, \tag{2.6}$$

$$F_v = \frac{f Re \mu_v}{2 R_v^2 A_{vap} \rho_v \lambda}, \tag{2.7}$$

and σ is the surface tension of fluid, r_{eff} is the effective pore radius of wick structure, ρ_l is the liquid density, g is the acceleration of gravity, L_{HP} is the total length of heat pipe, ϕ is the inclination angle of pipe with respect to gravity field, μ_l is the dynamic viscosity of liquid, A_{wick} is the cross-sectional area of wick structure, K is the permeability of wick structure, λ is the latent heat of evaporation, f is a drag coefficient for vapor flow, Re is the Reynolds number of vapor, μ_v is the dynamic viscosity of vapor, A_{vap} is the area of vapor space, ρ_v is the vapor density.

2.3.5 Boiling limit

While the other limits cited are limitations of the axial heat flux through the pipe, the boiling limit is a limitation of the radial heat flux. Excess of radial heat flux in evaporator can lead to the formation of boiling bubbles inside the wick structure which can cause hot spots and even block the circulation of fluid through the wick. The maximum heat transfer rate on boiling limit $Q_{b,max}$ (CHI, 1976):

$$Q_{b,max} = \frac{2\pi L_e k_{eff} T_v}{\lambda\, p_v\, ln\left({}^{r_i}/{}_{r_v}\right)} \left[\frac{2\sigma}{r_n} - p_c\right], \tag{2.8}$$

where L_e is the length of evaporator, k_{eff} is the effective thermal conductivity of wick structure, $T_v$is the vapor temperature, σ is the surface tension of fluid, λ is the latent heat of evaporation, p_v is vapor pressure, p_c is capillary pressure, r_i is inner radius of pipe, r_v is vapor core radius, and r_n is the boiling nucleation radius.

Figure 2.3 shows all operational limits mentioned above as a function of temperature, evaluated for an aluminum-ammonia axially grooved heat pipe. The minimum power input evaluated is $89.79\ W$ for boiling limit at $80\ ℃$. Viscous and sonic limits are never reached within the temperature range from $-50\ ℃$ to $80\ ℃$. Such levels of operational limits are not a concern in usual satellite applications.

Figure 2.3 – Operational Limits of an Aluminum Ammonia Heat Pipe.

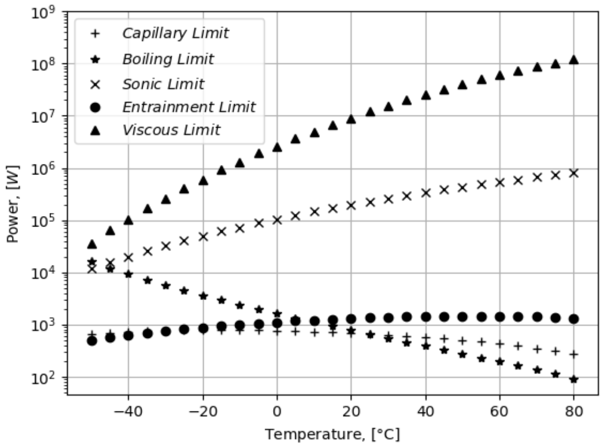

Operational limits of the aluminum ammonia conventional heat pipe used in experiments.
Source: The author.

2.4 Noncondensable gas formation and effect on heat pipes

Chemical reactions between the fluid and container or decomposition of the working fluid may result in noncondensable gas production (MARCUS, 1972). It has already been observed for stainless steel pipes working with methanol (ANDERSON et al., 1974), with nickel pipes working with water (ANDERSON, 1973), aluminum heat pipes with acetone (LOBANOV et al, 1991; REAY; JOHNSON, 1976), and even stainless steel pipes filled with ammonia (ENINGER; FLEISHMAN; LUEDKE, 1976). Noncondensable gas can also be generated in orbital conditions because of radiolysis of working fluid.

For aqueous systems, recent methods to evaluate compatibility between container material and working fluid make use of E–pH, or Pourbaix diagrams to determine beforehand the expected reaction products of some particular system (STUBBLEBINE et al, 2016).

The noncondensable gas formed is carried with the flow and accumulates at the end of the condenser, as presented in Figure 2.4. At sufficient quantities, this gas partially blocks the heat rejection area of the condenser, forcing the pipe to operate at higher temperatures, which can be harmful to the system being thermally controlled (TOWER; KAUFMAN, 1977).

The length of the zone occupied with noncondensable gas is proportional to the mass of gas and to the mean temperature of the zone, and inversely proportional to the pressure of vapor in the refluxing section of the heat pipe. (COTTER, 1965)

Figure 2.4 – Noncondensable Gas Location.

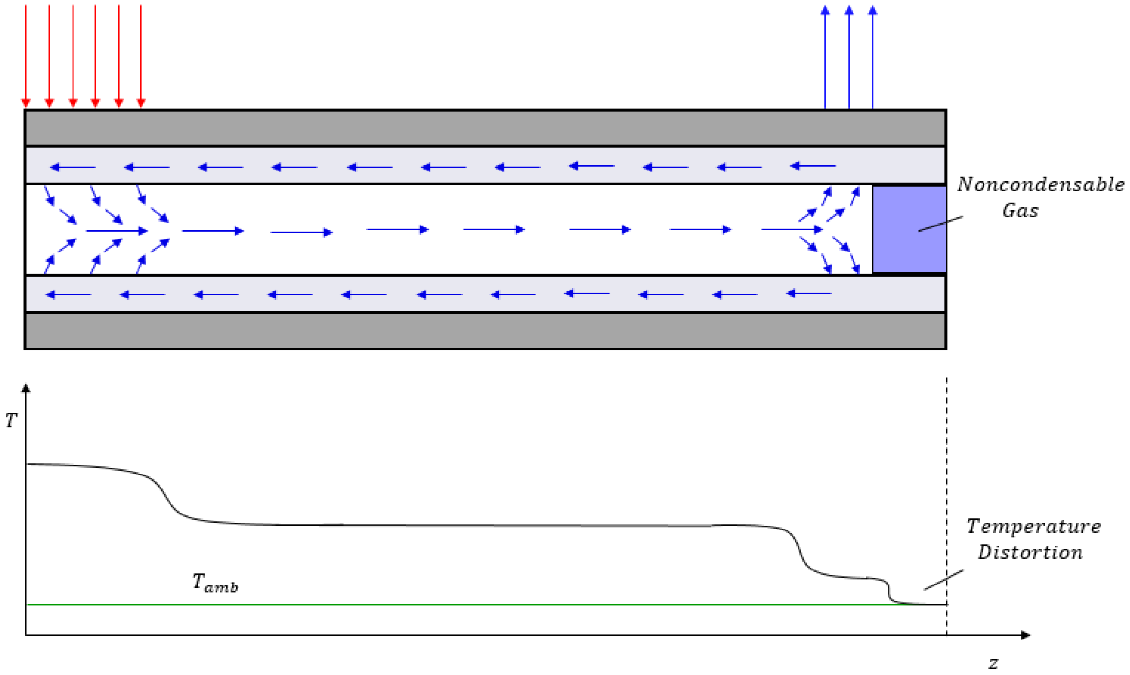

Heat pipe representation with partial blockage of condenser by noncondensable gas, and its temperature profile with distortion at the end of condenser.
Source: The author.

The temperature profile along the heat pipe gets a distortion at the end of condenser. Noncondensable gas, accumulated at the end of heat pipe, reduces the effective length of the condenser section in steady-state operation.

The amount of noncondensable gas, for the first stages of corrosion, can be expressed by the Arrhenius equation (TOWER; KAUFMAN, 1977; ANDERSON et al., 1974):

$$n = B_1 A_{contact} t_{hours}^{1/2} e^{-\left(\frac{E_1}{k_b T}\right)}, \tag{2.9}$$

where n is the number of moles of gas, t_{hours} is heat pipe lifetime in hours, $A_{contact}$ is the total internal area of the material in contact with working fluid, B_1 is a constant characteristic of the corrosion process, E_1 is the activation energy of the process, k_b is the Boltzmann's constant and T is the temperature.

At later stages, after the previous substances produced act as a catalyst for new reactions, these catalytic reactions are considered to predominate (ANDERSON et al., 1974) and would be expected to obey a linear time dependence (TOWER; KAUFMAN, 1977; ANDERSON et al., 1974):

$$n = B_2 A_{contact} t_{hours} e^{-\left(\frac{E_2}{k_b T}\right)}, \tag{2.10}$$

where n is the number of moles of gas, t_{hours} is time in hours, $A_{contact}$ is the total internal area of the material in contact with working fluid, B_2 is a constant that represent a barrier between molecules on the catalytic surface, E_2 is the activation energy of the process, k_b is the Boltzmann's constant and T is the temperature.

The presence of noncondensable gas was investigated in high temperature naphthalene thermosyphons by Mantelli et al. (2010). Authors concluded that the effect of noncondensable gas become more evident at low temperatures because at high temperatures the naphthalene is capable to compress the noncondensable gas in small regions.

The effect of noncondensable gas in loop thermosyphons was studied by He et al. (2013), where the startup of the device was studied. They came to conclusion that the presence of noncondensable gas in the system leads to an increase in startup time, liquid superheat and temperature overshoot. In addition, the temperature overshoot is a function of the quantity of noncondensable gas. The more gas, the higher the overshoot. Same common effects occurred on startup with noncondensable gas presence in the loop thermosyphon occurred again at startup of a loop heat pipe studied by He et al. (2017).

2.5 Noncondensable gas detection methods

For heat pipe applications it is very important to have a precise and practical method for noncondensable gas detection without heat pipe destroying.

Considering only non-destructive methods, there are basically two different ways to detect the presence of noncondensable gas inside the pipe. One way is with heat pipe operating in steady-state condition and another way is with heat pipe operating in transient mode.

2.5.1 Steady-state method

The steady-state method is broadly used in life tests, in which the temperature profile along the pipe is measured after heat pipe operating for long periods. Distortions in temperature measurement at the end of the condenser can lead to the conclusion of presence of noncondensable gas at that region, and even the location of the diffuse frontier between noncondensable gas and vapor (MARCUS, 1972).

Among the difficulties of the steady-state method are following:

– the high conductivity of the pipe shell leading to very small temperature differences along the condenser length and imprecise determination of the location of diffuse frontier;

– a temperature drop can appear at the end of condenser even without noncondensable gas due to the extra cooling from the end cap with ambient. If the condenser is on the same side of the filling tube this effect is increased. This is known as “end effect” of heat pipes;

– at zero gravity or at horizontal orientation, the formation of a liquid meniscus may occur at the end of the pipe leading to a partial block of the condenser even without noncondensable gas.

2.5.2 Transient method

The transient method is a recent method that considers the rates of temperature change instead of the absolute value of temperature along the axis (SMIRNOV; KOCHETKOV; TRETJAKOV, 2009; BERTOLDO JUNIOR, 2017).

Before the startup, the noncondensable gas is distributed homogeneously in the vapor core. During startup or shutdown, there is a process of redistribution of vapor and noncondensable gas. Bertoldo Junior (2017) showed that the temperature change rates are slower for a heat pipe with presence of noncondensable gas in comparison with a heat pipe without noncondensable gas due this redistribution dynamics. This difference in rates is higher in the shutdown case and the sensibility achieved by this method showed better results than the steady-state method.

2.6 Previous mathematical models of heat pipes

Bowman (1987) presented a 2D model of steady compressible vapor dynamics of a heat pipe, though almost all data was presented in terms of pressure and not temperature, and due to the nature of the research the heat pipe utilized in his experiments worked with pressure source and sink not with heat source and sink (Figure 2.5).

Figure 2.5 – Bowman's Porous Pipe.

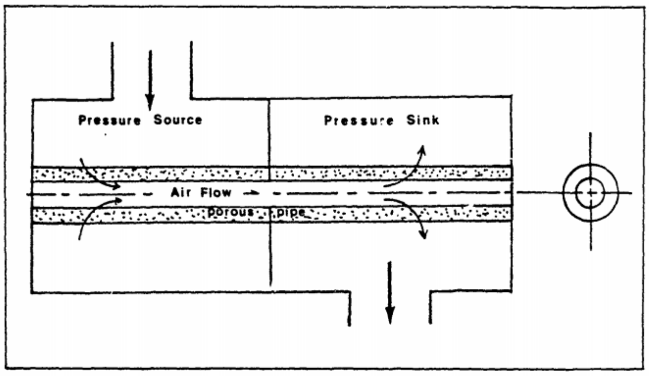

Figure 2.1 Porous Pipe Concept

Representation of the heat pipe with a pressure source and sink.
Source: Bowman (1987).

Issacci et al. (1989) presented a 2D transient model of vapor dynamics inside a heat pipe. This model simulates a rectangular cross section heat pipe, but no equation for wall and wick is used and heat input and output is directly applied to the vapor equations as source terms (Figure 2.6). No comparison with experimental data is presented.

Figure 2.6 – Vapor Flow Patterns of Issacci's Model.

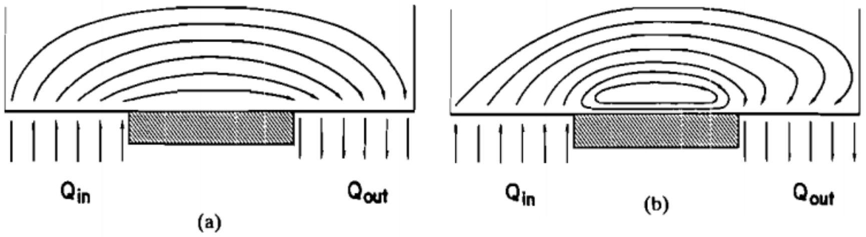

Vapor flow patterns: (a) low input heat flux, (b) high input heat flux.

Vapor flow patterns for low and high heat inputs directly applied to the vapor.
Source: Issacci et al. (1989).

Faghri (1991) and his colleagues, in a series of reports (JANG et al., 1989a, JANG et al., 1989b) presented a transient model for simulation of high temperature heat pipes, in which a 1D approach is used to take into account the vapor dynamics and those equations were coupled with a 2D mesh for wall and wick structure. This model, presented in Figure 2.7 also allows a startup with frozen working fluids.

Figure 2.7 – Mesh Representation of Faghri's Model.

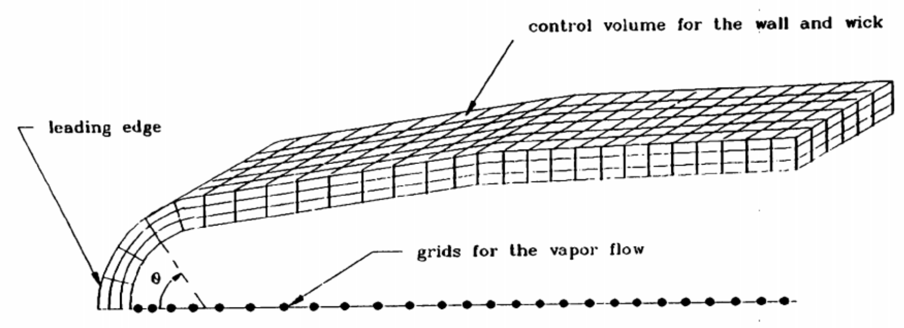

Representation of 2D mesh for wall and wick and 1D mesh for vapor.
Source: Faghri (1991).

Hall and Doster (1990) presented the code THROHPUT (Thermal Hydraulic Response of Heat Pipes Under Transients). This code is capable of simulate a transient 2D model of high temperature heat pipes from frozen state. It also takes into account the momentum of liquid in wick structure and the presence of noncondensable gas within vapor using a dusty gas model. The model can predict meniscus formation at the evaporator zone and pools at the condenser zone, shown in Figure 2.8.

Figure 2.8 – Meniscus and Pool Formation on THROHPUT Code.

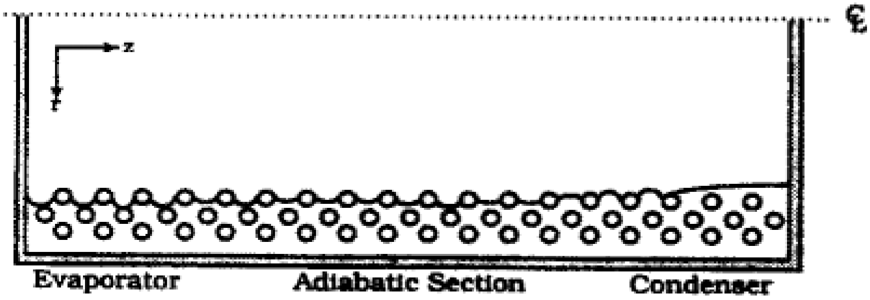

Meniscus formation at the evaporator and pool formation at the condenser zone.
Source: Hall and Doster (1990).

Tournier and El-Genk (1996) presented the heat pipe numerical model and code HPTAM (Heat Pipe Transient Analysis Model). This code also simulates a transient 2D model of heat pipes from frozen state. This code is capable to take into account sublimation and resolidification of working fluid, melting and freezing of the working fluid inside the wick structure, and the liquid flow inside the wick. All those features allow the model to predict capillary limit, dry-out of the wick, and the formation of liquid pool in gravity assisted heat pipes (Figure 2.9).

Figure 2.9 – Liquid Pool Formation on HPTAM Code.

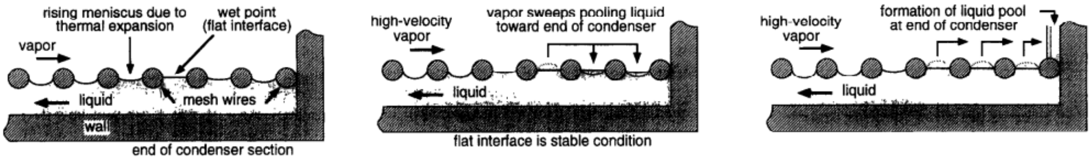
rising meniscus due to thermal expansion
wet point (flat interface)
vapor
liquid
mesh wires
wall
end of condenser section
high-velocity vapor
vapor sweeps pooling liquid toward end of condenser
liquid
flat interface is stable condition
high-velocity vapor
formation of liquid pool at end of condenser
liquid

Illustration of liquid pooling at end of condenser.

Liquid pool formation at the end of condenser.
Source: Tournier and El-Genk (1996).

2.7 Previous mathematical models of heat pipes with noncondensable gas

One of the first numerical models of a heat pipe with noncondensable gas was presented by Edwards and Marcus (1972). The authors presented an analysis based on a numeric steady-state one dimensional model of the heat and mass transfer characteristics of a gas-loaded heat pipe. The model took into account for radiation and convection from an external finned condenser, axial heat conduction in the walls and wicks, and mass diffusion between vapor and noncondensable gas.

Figure 2.10 – Gas Loaded Heat Pipe and Temperature Distribution.

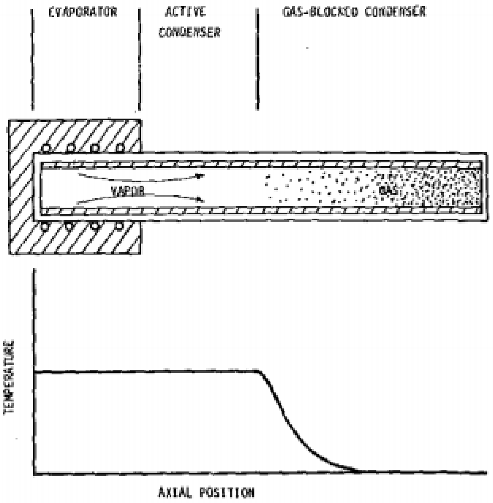
EVAPORATOR
ACTIVE CONDENSER
GAS-BLOCKED CONDENSER
VAPOR
GAS
TEMPERATURE
AXIAL POSITION

Schematic diagram and temperature distribution of a gas-loaded heat pipe
Source: Edwards and Marcus (1972).

In 1973, Rohani and Tien (1973) presented a two dimensional steady-state model of a gas-loaded heat pipe, which included heat and mass transfer in a cylindrical heat pipe with evaporator, condenser and noncondensable gas sections with negligible axial conduction through the wall and the wick.

Figure 2.11 – Axial Mass Distribution of Rohani and Tien’s Model.

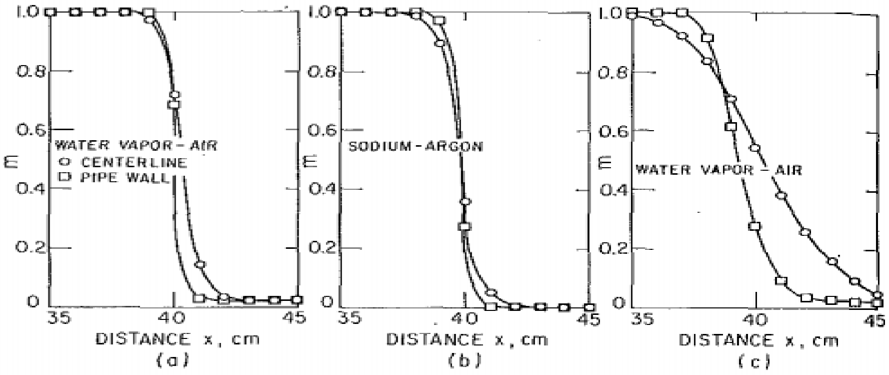

Axial mass distribution along the axis for three different vapor-gas combinations.
Source: Rohani and Tien (1973).

Harley and Faghri (1994) presented a two dimensional transient model of a high temperature gas-loaded heat pipe. This model accounts for diffusion and treats the noncondensable gas separately from the vapor. The model also couples the heat transfer equation of wall with energy equation of vapor-gas using a conjugate solution technique. The authors concluded from the model that the quantity of noncondensable gas heavily affects the steady-state operation of the heat pipe. Another conclusion obtained was the demonstration that the time period to heat pipe reach steady-state operation is increased with gas amount increasing.

Figure 2.12 – Vapor-Gas Dynamics for a High Temperature Heat Pipe.

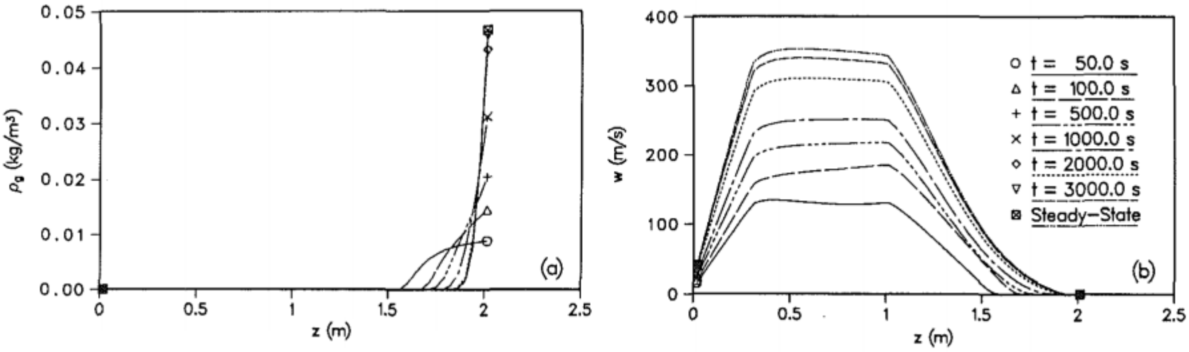

Vapor-gas dynamics for the gas-loaded heat pipe, with transient centerline gas density profiles and centerline axial velocity profiles.
Source: Harley and Faghri (1994).

3 MATHEMATICAL AND NUMERICAL MODEL

This chapter presents the complete set of equations that govern the phenomena that occurs in a heat pipe in the presence of noncondensable gas. The numerical algorithm uses staggered meshes and the procedure to couple velocity and pressure was done using SIMPLE algorithm. At last, the Tridiagonal Matrix Algorithm (TDMA) is presented.

3.1 Transient 1D mathematical model of heat pipe

The model presented here is transient and one-dimensional, with conservative equations for wall, wick, and mixture of vapor and noncondensable gas. A representation of the model nodes is given in Figure 3.1.

Figure 3.1 – Wall, Wick and Mixture Nodes Representation.

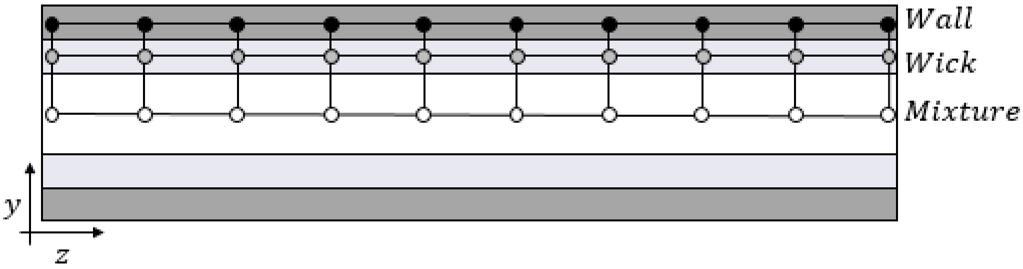

Graphic representation of wall, wick and mixture nodes.
Source: The author.

3.1.1 Mixture flow model

The compressible continuity equation of vapor-gas mixture, adapted from the continuity equation presented by Jang et al. (1989a), is the following:

$$\frac{\partial\bar{\rho}}{\partial t}+\frac{\partial(\bar{\rho}u)}{\partial z}=\frac{4j_v}{D_v}, \tag{3.1}$$

where $\bar{\rho}$ is the mixture density, u is the mixture velocity, j_v is the radial vapor mass flux caused by evaporation-condensation process, D_v is the diameter of vapor channel, t is time and z is the coordinate along the axis.

The mixture density is defined as the sum of vapor and noncondensable gas densities:

$$\bar{\rho}=\rho_v+\rho_{NCG}, \tag{3.2}$$

as well as the mixture pressure is defined as the sum of vapor and noncondensable gas partial pressures:

$$\bar{p} = p_v + p_{NCG}, \tag{3.3}$$

The evaporation/condensation mass rate (or radial vapor mass flux) is linked to local internal wick-vapor mixture heat transfer instant balance:

$$j_v = \rho_v v = \frac{q}{\lambda} = \frac{h_{evap/cond}}{\lambda}(T_{wick} - T_{mix}), \tag{3.4}$$

where j_v is the evaporation/condensation mass rate of vapor or vapor mass flux, ρ_v is the vapor density, v is the vapor velocity in radial direction, $h_{evap/cond}$ is the effective heat transfer coefficient between the wick structure and the mixture, T_{wick} is the temperature of wick structure, T_{mix} is the temperature of the mixture, q is the heat flux from the wick structure to vapor core and λ is the latent heat of evaporation of fluid.

Equation (3.4) assumes that once an eventual positive temperature difference appears between wick and vapor, it will cause evaporation and if a negative difference appears it will cause condensation. It also considers that fluid is in a saturation state, which causes that all heat flux activated by any eventual temperature difference will be responsible for phase change. Such an approach is very common in heat pipe modeling to represent the internal heat transfer with vapor core applying effective heat transfer coefficients. The values of $h_{evap/cond}$ are generally obtained from experimental data, and usually have relatively high magnitudes.

The momentum equation, presented by Jang et al. (1989a), adapted to the mixture:

$$\frac{\partial(\bar{\rho}u)}{\partial t} + \frac{\partial(\bar{\rho}uu)}{\partial z} = -\frac{\partial\bar{p}}{\partial z} + \frac{4}{3}\bar{\mu}\frac{\partial^2 u}{\partial z^2} - \frac{\bar{\rho}u^2 f}{D_v}, \tag{3.5}$$

where $\bar{\rho}$ is the mixture density, u is the mixture velocity, $\bar{p}$ is the mixture pressure, $\bar{\mu}$ is the dynamic viscosity of the mixture, t is time, z is the coordinate along the axis and f is a friction factor depending on the flow characteristics.

Considering a circular heat pipe with vapor flow always laminar, the friction factor is:

$$f = \frac{16}{Re}, \tag{3.6}$$

and for turbulent flow:

$$f = \frac{0.079}{Re^{0.25}}, \tag{3.7}$$

where Re is the Reynolds number.

The Reynolds number for the mixture, in a circular pipe, is given by:

$$Re = \frac{\bar{\rho} u D_v}{\bar{\mu}}. \tag{3.8}$$

The dynamic viscosity of the mixture is defined as the mass fraction weighted viscosity:

$$\bar{\mu} = X\mu_{NCG} + (1 - X)\mu_v, \tag{3.9}$$

where μ_{NCG} is the viscosity of noncondensable gas, μ_v is the viscosity of vapor, and X is the concentration of noncondensable gas in the mixture, defined as:

$$X = \frac{\rho_{NCG}}{\rho_{NCG} + \rho_v}. \tag{3.10}$$

Under the assumption that the mixture flow is compressible and laminar, the momentum equation gets the form as follows,

$$\bar{\rho}\frac{\partial u}{\partial t} + u\frac{\partial(\bar{\rho}u)}{\partial z} + \bar{\rho}u\frac{\partial(u)}{\partial z} = -\frac{\partial \bar{p}}{\partial z} + \frac{4}{3}\bar{\mu}\frac{\partial^2 u}{\partial z^2} - \frac{32\bar{\mu}u}{D_v^2}. \tag{3.11}$$

To account for the presence of noncondensable gas, an additional continuity equation for the noncondensable gas is used. It considers the convection contribution of mixture velocity and a source term from diffusion between vapor and gas (BIRD et al. 2001):

$$\frac{\partial \rho_{NCG}}{\partial t} + \frac{\partial \rho_{NCG} u}{\partial z} = D_{vg}\frac{\partial^2 \rho_{NCG}}{\partial z^2}. \tag{3.12}$$

The energy equation of mixture adapted from the energy equation of vapor from Jang et al. (1989b), here solved directly for temperature:

$$\bar{C}_p\frac{\partial \bar{\rho} T_{mix}}{\partial t} + \bar{C}_p\frac{\partial \bar{\rho} u T_{mix}}{\partial z} = \bar{k}\frac{\partial^2 T_{mix}}{\partial z^2} + u\frac{\partial \bar{p}}{\partial z} + \frac{4}{3}\bar{\mu}\frac{\partial^2 u}{\partial z^2}u + \frac{4}{3}\bar{\mu}\left(\frac{\partial u}{\partial z}\right)^2 + \frac{4 j_v \bar{C}_p T_{mix}}{D_v} - \frac{2\bar{\rho}u^3 f}{D_v}. \tag{3.13}$$

Considering laminar flow, it becomes:

$$\bar{C}_p \frac{\partial \bar{\rho} T_{mix}}{\partial t} + \bar{C}_p \frac{\partial \bar{\rho} u T_{mix}}{\partial z} = \bar{k} \frac{\partial^2 T_{mix}}{\partial z^2} + u \frac{\partial \bar{p}}{\partial z} + \frac{4}{3} \bar{\mu} \frac{\partial^2 u}{\partial z^2} u + \frac{4}{3} \bar{\mu} \left(\frac{\partial u}{\partial z} \right)^2 + \frac{4 j_v \bar{C}_p T_{mix}}{D_v} - \frac{32 \bar{\mu} u^2}{D_v^2}, \tag{3.14}$$

where $\bar{C}_p$ is the specific heat at constant pressure of mixture, $\bar{\rho}$ is the mixture density, T_{mix} is the mixture temperature, t is time, z is the coordinate along the axis, $\bar{k}$ is the mixture thermal conductivity, $\bar{p}$ is the mixture pressure, $\bar{\mu}$ is the mixture dynamic viscosity, u is the mixture axial velocity, j_v is the radial vapor mass flux and D_v is the vapor channel diameter.

The mass fraction weighted specific heat at constant pressure, and thermal conductivity of mixture are defined as follows:

$$\bar{C}_p = X \bar{C}_{p,NCG} + (1 - X) \bar{C}_{p,v}, \tag{3.15}$$

$$\bar{k} = X k_{NCG} + (1 - X) k_v. \tag{3.16}$$

The Clausius-Clapeyron equation relates the temperature and pressure of a saturated fluid:

$$ln \left(\frac{p_v}{p_{stag}} \right) = \frac{\lambda}{R_v} \left(\frac{1}{T_{stag}} - \frac{1}{T_{mix}} \right), \tag{3.17}$$

which when solved for pressure becomes:

$$p_v = p_{stag} e^{\frac{\lambda}{R_v} \left(\frac{1}{T_{stag}} - \frac{1}{T_{mix}} \right)}, \tag{3.18}$$

where p_v is the current pressure of vapor, p_{stag} is the stagnation or other reference vapor pressure, T_{mix} is the current temperature of the mixture, T_{stag} is the stagnation or other reference vapor temperature, λ is the latent heat of evaporation of fluid and R_v is the gas constant of vapor.

The equation of state for noncondensable gas is:

$$p_{NCG} = \rho_{NCG} R_{NCG} T_{mix}, \tag{3.19}$$

where p_{NCG} is the pressure of noncondensable gas, ρ_{NCG} is the density of noncondensable gas, R_{NCG} is the gas constant of fluid and T_{mix} is the temperature of the mixture.

3.1.2 Wall and wick model

3.1.2.1 Wall

The heat equation at the wall, with source term, adapted from Jang et al., (1989b):

$$\rho_w C_{p,w} \delta_w \frac{\partial T_w}{\partial t} = k_w \delta_w \frac{\partial^2 T_w}{\partial z^2} + q_{w,in}, \tag{3.20}$$

where ρ_w is the wall density, $C_{p,w}$ is the specific heat at constant pressure of wall, T_w is the temperature at wall, k_w is the thermal conductivity of wall, t is time, z is the coordinate along the axis, δ_w is the wall thickness, $q_{w,in}$ is the heat flux at the wall.

The source term, $q_{w,in}$ in Equation (3.20), consider heat being exchanged between wall and wick, wall and skin heater, and wall and ambient:

$$q_{w,in} = h_{wick,w}(T_{wick} - T_w) + h_{h,w}(T_h - T_w) + h_{amb}(T_{amb} - T_w), \tag{3.21}$$

where $h_{wick,w}$ is the heat transfer coefficient between wick and wall regions, T_{wick} is the temperature of wick region, T_w is the temperature at wall, $h_{h,w}$ is the heat transfer coefficient between heater and wall, T_h is the heater temperature, h_{amb} is the convection coefficient between wall and ambient, T_{amb} is the ambient temperature. The convection coefficients were estimated from Newton's law of cooling in steady-state operation from experimental data.

3.1.2.2 Wick

The heat equation of the wick structure was adapted from Faghri (1991) and Das et al. (2017), neglecting the velocity:

$$\left(\rho C_p\right)_{wick} \delta_{wick} \frac{\partial T_{wick}}{\partial t} = k_{eff} \delta_{wick} \frac{\partial^2 T_{wick}}{\partial z^2} + q_{wick,in}, \tag{3.22}$$

in which the volumetric specific heat of wick $\left(\rho C_p\right)_{wick}$ is defined by:

$$\left(\rho C_p\right)_{wick} = \left(\varepsilon\left(\rho C_p\right)_l + (1-\varepsilon)\left(\rho C_p\right)_s\right), \tag{3.23}$$

and the equivalent thermal conductivity k_{eff} for porous structures is:

$$k_{eff} = \varepsilon k_l + (1-\varepsilon) k_s. \tag{3.24}$$

The effective thermal conductivity for grooved structures is given by Chi (1976):

$$k_{eff} = \frac{(w_s w_d k_l k_s) + w_l k_l (0.185 w_s k_s + w_d k_l)}{(w_l + w_s)(0.185 w_s k_s + w_d k_l)} \tag{3.25}$$

In the above equations, $(\rho C_p)_{wick}$ is the volumetric specific heat, $T_{wick}$is the temperature of wick structure, k_{eff} is the effective thermal conduction of the wick structure, δ_{wick} is the thickness of the wick, ε is the porosity of the wick structure, t is time, z is the coordinate along the axis, $q_{wick,in}$ is the heat flux at wick, w_s is the width of the fin, w_d is the depth of the fin, w_l is the width of the groove, k_l is the themal conductivity of liquid phase and k_s is the thermal conductivity of the solid phase.

For the wick structure, the source term $q_{wick,in}$ in Equation (3.22), considers heating being exchanged between wick and wall, and wick and mixture:

$$q_{wick,in} = h_{wick,w}(T_w - T_{wick}) + h_{evap,cond}(T_{mix} - T_{wick}), \tag{3.26}$$

here $h_{wick,w}$ is the heat transfer coefficient between the wick and wall structure, T_w is the wall temperature, T_{wick} is the wick structure temperature, $h_{evap,cond}$ is the effective heat transfer coefficient between wick structure and mixture, T_{mix} is the mixture temperature.

3.1.3 Heating block and heater model

At evaporator, it was considered the presence of a polymeric block with two skin heaters attached to it. The heaters were used to input power to the heat pipe.

Figure 3.2 – Heating Block and Heater Nodes Representation.

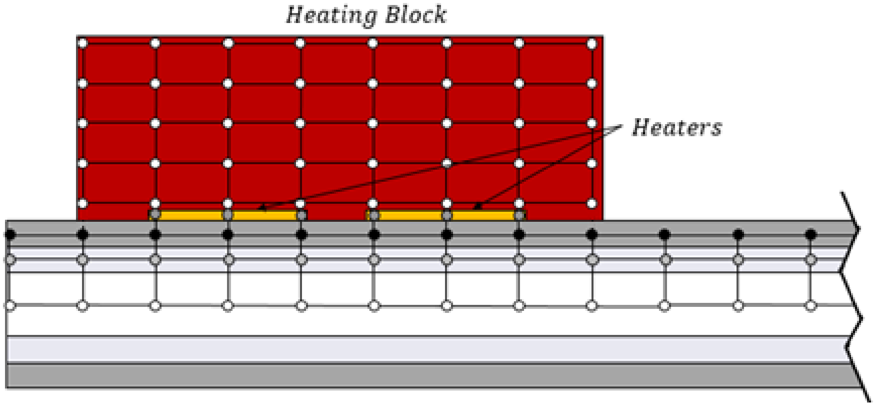

Graphic representation of heating block and heaters with heat pipe nodes.
Source: The author.

3.1.3.1 Heating block

Heat equation of polymer block considers heat coming from skin heater, and rejected heat to ambient through natural convection from its external surfaces. Due to low thermal conductivity of the polymer block, it was verified that a two dimensional heat equation describes better the behavior of the component:

$$\rho_b C_{p,b} \delta_b \frac{\partial T_b}{\partial t} = k_b \delta_b \left(\frac{\partial^2 T_b}{\partial z^2} + \frac{\partial^2 T_b}{\partial y^2} \right) + q_{b,in}, \tag{3.27}$$

where, ρ_b is the density of block, $C_{p,b}$ is the heat capacity at constant pressure of block material, δ_b is the thickness of the polymer block, T_b is the block's temperature, k_b is the thermal conductivity of the block, t is time, z is the coordinate along the axis, y is the coordinate along the axis, $q_{b,in}$ is the heat flux at block.

The source term $q_{b,in}$, neglects the heat exchange between heating block and wall, and considers heating being exchanged between heating block and heater, and heating block and ambient:

$$q_{b,in} = h_{h,b}(T_h - T_b) + h_{b,amb}(T_{amb} - T_b), \tag{3.28}$$

where, $h_{h,b}$ is the heat transfer coefficient between the polymer block and heater, T_h is the skin heater temperature, T_b is the temperature of polymer block, $h_{b,amb}$ is the heat transfer coefficient between polymer block and ambient, and T_{amb} is ambient temperature. The heat exchange between heating block and heat pipe wall is neglected due to the presence of unavoidable air gap of a thickness equal to the skin heater thickness.

3.1.3.2 Heaters

The heat equation of the skin heater was simplified to a lumped-parameter system due to the small mass and dimensions of the component, so thermal conductivity through the material (Kapton) was neglected. The skin heater dissipates its power mainly to the evaporator zone of heat pipe wall, however, part of the dissipated heat is lost to the polymer insulation block:

$$\rho_h C_{p,h} \delta_h \frac{\partial T_h}{\partial t} = q_{h,in}, \tag{3.29}$$

here, ρ_h is the density of skin heater, $C_{p,h}$ is the heat capacity at constant pressure of heater, δ_h is the thickness of the heater, T_h is the temperature of heater, t is time, $q_{h,in}$ is the heat flux at heater.

The source term $q_{h,in}$, takes into account the heat transfer between heating block and heater, and heater and wall, as well as the direct power input given by power source:

$$q_{h,in} = h_{h,b}(T_h - T_b) + h_{h,w}(T_w - T_h) + q_h, \tag{3.30}$$

here, $h_{h,b}$ is the heat transfer coefficient between heater and polymer block, T_b is the temperature of polymer block, T_h is the skin heater temperature, $h_{h,w}$ is the heat transfer coefficient between heater and wall, T_w is wall temperature and q_h is the heat flux input from power source.

3.2 Starting and boundary conditions

All simulations used the same initial and boundary conditions. Considering the generalized notation, $\phi(t,z)$ for one dimensional parameters and , $\phi(t,z,y)$ for two dimensional parameters, at the starting conditions with $t=0$ all temperatures are in equilibrium with ambient and all velocities and fluxes are zero:

$$T_{wall}(0,z) = T_{amb}, \tag{3.31}$$

$$T_{wick}(0,z) = T_{amb}, \tag{3.32}$$

$$T_{mix}(0,z) = T_{amb}, \tag{3.33}$$

$$T_h(0,z) = T_{amb}, \tag{3.34}$$

$$T_b(0,z,y) = T_{amb}, \tag{3.35}$$

$$u(0,z) = 0, \tag{3.36}$$

$$j_v(0,z) = 0, \tag{3.37}$$

$$p_v(0,z) = p_{stag} e^{\frac{\lambda}{R_v}\left(\frac{1}{T_{stag}} - \frac{1}{T_{amb}}\right)}, \tag{3.38}$$

$$\rho_v(0,z) = \frac{p_v}{R_v T_{amb}}, \tag{3.39}$$

$$p_{NCG}(0,z) = \frac{m_{NCG} R_{NCG} T_{amb}}{A_{vap} L_{HP}}, \tag{3.40}$$

$$\rho_{NCG}(0,z) = \frac{p_{NCG}(0,z)}{R_{NCG} T_{amb}}. \tag{3.41}$$

At boundaries, a Neumann boundary condition was applied to the temperatures and densities, and no-slip condition to the velocity:

$$\frac{\partial T_w(t,0)}{\partial z} = \frac{\partial T_w(t,L)}{\partial z} = 0, \tag{3.42}$$

$$\frac{\partial T_{wick}(t,0)}{\partial z} = \frac{\partial T_{wick}(t,L)}{\partial z} = 0, \tag{3.43}$$

$$\frac{\partial T_{mix}(t,0)}{\partial z} = \frac{\partial T_{mix}(t,L)}{\partial z} = 0, \tag{3.44}$$

$$\frac{\partial T_b(t,0,y)}{\partial z} = \frac{\partial T_b(t,L,y)}{\partial z} = 0, \tag{3.45}$$

$$\frac{\partial T_b(t,z,y)}{\partial y} = \frac{\partial T_b(t,z,H)}{\partial y} = 0, \tag{3.46}$$

$$\frac{\partial \rho_v(t,0)}{\partial z} = \frac{\partial \rho_v(t,L)}{\partial z} = 0, \tag{3.47}$$

$$\frac{\partial \rho_{NCG}(t,0)}{\partial z} = \frac{\partial \rho_{NCH}(t,L)}{\partial z} = 0, \tag{3.48}$$

$$u(t,0) = u(t,L) = 0, \tag{3.49}$$

where L is the total length of the heat pipe, and H is the height of polymer block.

3.3 Heat transfer and diffusion coefficients

3.3.1 External heat transfer coefficients

In the experimental setups, the condenser was cooled in two different ways, with free (or natural) convection or with free convection combined with forced convection. At free convection and forced convection zones, the coefficients were evaluated using correlation formulas presented in literature for a horizontal tube with square cross-section (INCROPERA, 2006).

The heat transfer coefficient at free convection zone was calculated using the harmonic average of Nusselt number of each side of heat pipe:

$$h_{nat} = \left(Nu_{up} + Nu_{down} + 2Nu_{side}\right)k_{air} / \left(B_{up} + B_{down} + 2B_{side}\right), \tag{3.50}$$

where, Nu is the Nusselt number, k_{air} is the thermal conductivity of air, and B is the characteristic length of geometry.

Table 3.1 shows the profile of the heat pipe with the characteristic length and the correlation used to calculate Nusselt number on each case.

Table 3.1 – Correlation Used on Each Side of Pipe.

Side of Pipe ($\boldsymbol{L}$)	Correlation Used
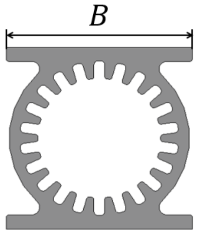	$Nu_{up} = 0.54Ra^{1/4}$
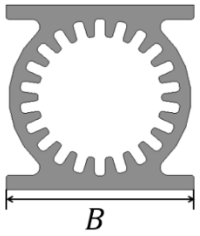	$Nu_{down} = 0.27Ra^{1/4}$
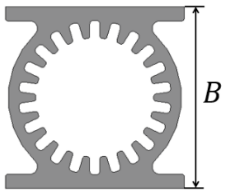	$Nu_{side} = \left\{ 0.825 + \frac{0.387Ra^{1/4}}{\left[1 + \left(\frac{0.492}{Pr}\right)^{9/26}\right]^{8/27}} \right\}^2$

Source: The author.

In Table 3.1, Rayleigh number Ra used to calculate Nusselt number Nu:

$$Ra = \frac{g\beta(T_s - T_{amb})B^3}{\nu\alpha}, \tag{3.51}$$

where, g is the acceleration of gravity, β is a thermal expansion coefficient (equals to$1/((T_s + T_{amb})/2)$), T_s is the temperature of surface, T_{amb} is ambient temperature, B is the characteristic length, ν is the kinematic viscosity, α is the thermal diffusivity and Pr is Prandtl number.

In a similar manner, the external heat transfer coefficient at forced convection zone:

$$h_f = \left(Nu_f k_{air}\right)/B. \tag{3.52}$$

In this case, the Nusselt number is a function of Prandtl and Reynolds number:

$$Nu_f = 0.102\ Re^{0.675}Pr^{1/3}. \tag{3.53}$$

The other two external heat transfer coefficients, heat transfer coefficient between heater and wall $h_{h,w}$, and heat transfer coefficient between heater and polymer block $h_{h,b}$ were adjusted to best fit numerical analysis with experimental data.

3.3.2 Internal heat transfer coefficients

Effective heat transfer coefficient between wick and vapor represents internal processes of intensive heat transfer during eventual evaporation or condensation. Using well-established approach, its values are extracted from experimental data of heat pipe performance steady-state test:

$$h_{evap/cond} = \frac{Q}{A_{wick,v}(T_{wick} - T_{mix})}, \tag{3.54}$$

where, Q is heat transferred between wick and mixture, $A_{wick,v}$ is the area of heat exchange between wick and vapor, T_{wick} is the temperature of wick and T_{mix} is temperature of mixture.

Direct measurements of wick and mixture temperatures are difficult and, very often, experimental data of those temperatures come with high uncertainties. A common approach is to evaluate the heat transfer coefficient between wick and vapor is using the difference in wall temperature at end of evaporator with wall temperature at adiabatic zone. Once the adiabatic zone is usually well insulated, and there are no radial heat transfer, the heat pipe wall temperature at the middle of the adiabatic zone becomes equal to vapor temperature, any wall temperature is very easy to measure.

Heat transfer coefficient between wick and wall:

$$h_{wick,w} = \frac{k_w}{\delta_{wick,w}}, \tag{3.55}$$

where, k_w is the thermal conductivity of wall and $\delta_{wick,w}$ is the thickness of wick and wall centerlines.

3.3.3 Diffusion coefficients

The mass diffusion coefficient D_{vg}, used at noncondensable gas conservation mass equation is a calculated from the Lennard-Jones parameters using the Chapman-Enskog theory (CUSSLER, 2009):

$$D_{vg} = \frac{(1.86x10^{-5})T_{mix}^{3/2}}{\bar{p}\sigma_{vg}^{2}\Omega_{vg}}\left[\frac{M_g + M_v}{M_g M_v}\right]^{1/2}, \tag{3.56}$$

where, T_{mix} is the temperature of vapor and gas mixture, M_v is the molecular weight of vapor, M_g is the molecular weight of gas, $\bar{p}$ is the pressure of mixture, σ_{vg} is the arithmetic average of the collision diameters of the two species, Ω_{vg} is a dimensionless diffusion collision integral obtained from tables from the energy of interaction between vapor and gas.

3.4 Numerical modeling

The flow chart of the numerical algorithm is presented and it is possible to see how all equations interact with each other in the Figure 3.3.

Figure 3.3 – Flow Chart of Algorithm.

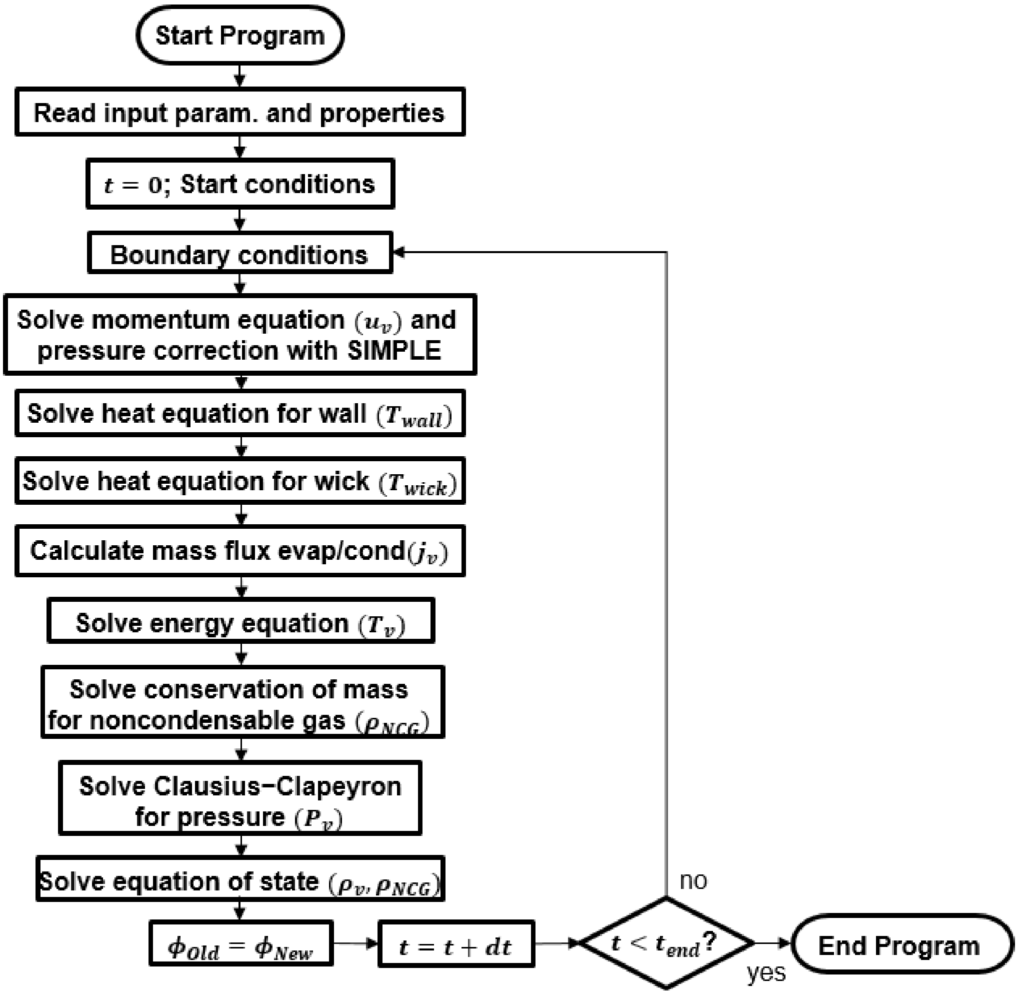
Start Program
Read input param. and properties
$t = 0$; Start conditions
Boundary conditions
Solve momentum equation (u_v) and pressure correction with SIMPLE
Solve heat equation for wall (T_{wall})
Solve heat equation for wick (T_{wick})
Calculate mass flux evap/cond(j_v)
Solve energy equation (T_v)
Solve conservation of mass for noncondensable gas (ρ_{NCG})
Solve Clausius−Clapeyron for pressure (P_v)
Solve equation of state (ρ_v, ρ_{NCG})
$\phi_{Old} = \phi_{New}$
$t = t + dt$
$t < t_{end}$?
no
yes
End Program

Flow chart with relations between equations during the execution of the algorithm.
Source: The author.

3.5 The staggered grid method

When the velocity components are defined at the nodes of a grid, the influence of pressure is not properly represented in the discretized momentum equations (VERSTEEG; MALALASEKERA, 2007). This can result in possible problems with pressure producing no resulting forces, a problem presented specially in one and two-dimensional models (PATANKAR, 1980). The solution is the use of a staggered grid, which can be seen in Figure 3.4, and the idea is to evaluate scalar variables ϕ, such as pressure, density or temperature at nodal points and calculate velocity components on cell faces.

Figure 3.4 – The staggered grid.

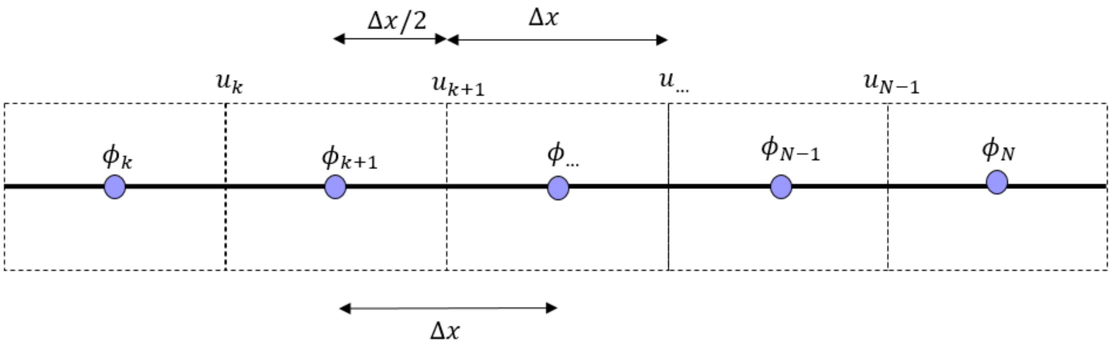

The staggered locations of velocities u and other scalar properties ϕ.
Source: The author.

3.6 The SIMPLE method

There are several methods available to solve pressure-velocity coupling, between them we can cite SIMPLE, SIMPLEC, SIMPLER, PISO and others. All of them follow the general idea to solve the pressure and velocity fields in a first step, with a second step to correct these fields. The SIMPLE algorithm was one of the first methods of its kind and further refinements (SIMPLEC, SIMPLER) have produced more economical and stable iteration methods, (VERSTEEG; MALALASEKERA, 2007).

Due to simplicity to code and debug, the procedure chosen was SIMPLE, which stands for Semi-Implicit Method for Pressure Linked Equations and was developed by Patankar and his advisor Professor Brian Spalding (PATANKAR, 1980).

For this procedure, we assume that the correct values of pressure and velocity are composed by:

$$p = p^* + p', \tag{3.57}$$

$$u = u^* + u', \tag{3.58}$$

where p^* and u^* are guessed values for pressure and velocity, and p' and u' correspond to the corrections in pressure and velocity respectively.

The implicit finite difference form of momentum equation:

$$\rho \frac{\left(u_k^{(2)} - u_k^{(1)}\right)}{dt} + u_k^{(2)} \frac{\left((\rho u)_{k+1}^{(1)} - (\rho u)_{k-1}^{(1)}\right)}{2dz} + (\rho u)_k^{(1)} \frac{\left(u_{k+1}^{(2)} - u_{k-1}^{(2)}\right)}{2dz} = -\frac{\partial p}{\partial z} + \frac{4}{3}\mu \frac{\left(u_{k+1}^{(2)} - 2u_k^{(2)} + u_{k-1}^{(2)}\right)}{dz^2} - \frac{32\mu u_k^{(1)}}{D_v^2}. \tag{3.59}$$

Rearranging the above equation, we have:

$$\left(\frac{\rho}{dt} + \frac{\left((\rho u)_{k+1}^{(1)} - (\rho u)_{k-1}^{(1)}\right)}{2dz} + \frac{8}{3}\frac{\mu}{dz^2}\right) u_k^{(2)} + \left(\frac{(\rho u)_k^{(1)}}{2dz} - \frac{4}{3}\frac{\mu}{dz^2}\right) u_{k+1}^{(2)} - \left(\frac{(\rho u)_k^{(1)}}{2dz} + \frac{4}{3}\frac{\mu}{dz^2}\right) u_{k-1}^{(2)} = \frac{\rho u_k^{(1)}}{dt} - \frac{\partial p}{\partial z} - \frac{32\mu u_k^{(1)}}{D_v^2}. \tag{3.60}$$

This leads to the discretization equation:

$$a_P u_P^{(2)} + a_E u_E^{(2)} + a_W u_W^{(2)} = b, \tag{3.61}$$

where:

$$a_P = \left(\frac{\rho}{dt} + \frac{\left((\rho u)_{k+1}^{(1)} - (\rho u)_{k-1}^{(1)}\right)}{2dz} + \frac{8}{3}\frac{\mu}{dz^2}\right), \tag{3.62}$$

$$a_E = \left(\frac{(\rho u)_k^{(1)}}{2dz} - \frac{4}{3}\frac{\mu}{dz^2}\right), \tag{3.63}$$

$$a_W = -\left(\frac{(\rho u)_k^{(1)}}{2dz} + \frac{4}{3}\frac{\mu}{dz^2}\right), \tag{3.64}$$

$$b = \frac{\rho u_k^{(1)}}{dt} - \frac{\partial p}{\partial z} - \frac{32\mu u_k^{(1)}}{D_v^2}. \tag{3.65}$$

This system result in a tridiagonal matrix, which can be solved by Gauss-Seidel method or with Thomas Algorithm and the values of velocity obtained correspond to the u^* values.

With this, we can also write a momentum equation for the correction values of velocity:

$$a_P u_P' + a_E u_E' + a_W u_W' + b = 0. \tag{3.66}$$

Dropping the neighbors terms and minor sources, in the momentum equation, it becomes:

$$a_P u'_P = -(p'_E - p'_P). \tag{3.67}$$

For convenience, we define

$$d_P^u = \frac{1}{a_P}, \tag{3.68}$$

so,

$$u'_P = -(p'_E - p'_P) d_P^u. \tag{3.69}$$

The pressure correction equation:

$$a_P p'_P = a_W p'_W + a_E p'_E + b, \tag{3.70}$$

where:

$$a_E = d_P^u, \tag{3.71}$$

$$a_W = d_W^u, \tag{3.72}$$

$$a_P = a_E + a_W, \tag{3.73}$$

$$b = u_W^* - u_P^* \tag{3.74}$$

This system results in a tridiagonal matrix, which can be effectively solved by Gauss-Seidel method or with Thomas Algorithm. In this work the Thomas Algorithm was chosen to solve the tridiagonal systems.

The final values for pressure and velocity are usually calculated with:

$$p_P = p_P^* + \alpha_{num} p'_P, \tag{3.75}$$

$$u_P = u_P^* + \alpha_{num} u'_P, \tag{3.76}$$

where α_{num} is an underrelaxation factor, and the values of pressure and velocity are calculated until convergence at each time step or for a fixed number of iterations.

In Figure 3.5 it is possible to see a flow chart showing the inner interactions of equations in the SIMPLE algorithm.

Figure 3.5 – Flow Chart of SIMPLE Algorithm.

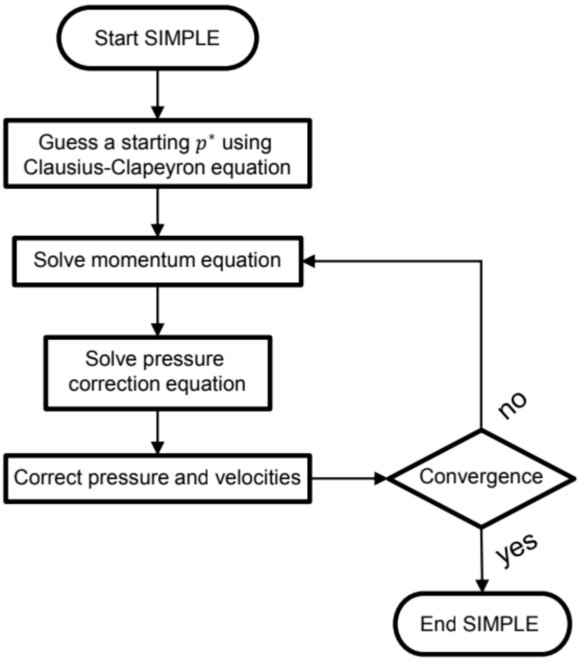
Start SIMPLE
Guess a starting p^* using Clausius-Clapeyron equation
Solve momentum equation
Solve pressure correction equation
Correct pressure and velocities
Convergence
no
yes
End SIMPLE

Flow Chart of commands during the execution of SIMPLE algorithm.
Source: The author.

3.7 Tridiagonal matrix algorithm

The Tridiagonal Matrix Algorithm, also known as Thomas Algorithm or simply TDMA, is the result of applying Gaussian elimination to the tridiagonal system of equations, (ANDERSON, 1995).

A tridiagonal matrix is a square matrix that the nonzero elements lie at main diagonal and the first diagonal above and below the main diagonal. A tridiagonal system is a system of equations whose associated matrix is tridiagonal, as follows:

$$\begin{bmatrix} a_1 & c_1 & & & \\ b_2 & a_2 & c_2 & & \\ & b_3 & a_3 & \ddots & \\ & & \ddots & \ddots & c_{n-1} \\ & & & b_n & a_n \end{bmatrix} \cdot \begin{bmatrix} x_1 \\ x_2 \\ x_3 \\ \vdots \\ x_n \end{bmatrix} = \begin{bmatrix} d_1 \\ d_2 \\ d_3 \\ \vdots \\ d_n \end{bmatrix}. \tag{3.77}$$

The values of b_1 and c_n are $b_1 = 0$ and $c_n = 0$ and were omitted from the matrix above.

To solve the tridiagonal system with Thomas algorithm the following coefficients are computed:

$$c'_i = \begin{cases} \dfrac{c_i}{a_i}, & i = 1 \\ \dfrac{c_i}{a_i - b_i c''_{i-1}}, & i = 2, 3, \ldots, n-1 \end{cases} \tag{3.78}$$

and:

$$d'_i = \begin{cases} \dfrac{d_i}{a_i}, & i = 1 \\ \dfrac{d_i - b_i d'_{i-1}}{a_i - b_i c''_{i-1}}, & i = 2, 3, \ldots, n-1 \end{cases} \tag{3.79}$$

The final solution is obtained with back substitution:

$$\begin{aligned} x_i &= d'_n & i &= 1 \\ x_i &= d'_n - c'_i x_{i+1} & i &= 2, 3, \ldots, n-1 \end{aligned} \tag{3.80}$$

4 MODEL VALIDATION

This chapter presents the results of three different validation tests obtained with the numeric model developed.

Validation 1: the first test was performed to evaluate how the model behaves in the presence of multiple heat sources. Two cases were modeled following the experimental setup and data presented by Faghri and Bushko (1991).

Validation 2: the second test was conducted with the model reconfigured to represent a setup presented by Saad et al. (2012). The heat pipe contains noncondensable gas in the vapor core. The experimental data were compared with generated numerical results.

Validation 3: the third test is a quality validation one. This case tests the capability of model to deal with sources and sinks applied to different locations of the heat pipe, including arbitrary changes of heat load and heat extraction zones. The symmetry tests consists of nine different cases for heat source and sink combinations.

4.1 Validation 1: multiple heat sources

For this setup, two cases were tested with one and two heat loads. The input data for the model corresponds to a heat pipe made of copper and filled with water as working fluid. The heat pipe length is $1.0\,m$ and shell is of $1.7\,mm$ thick, while the wick is $0.7\,mm$ thick. The vapor core is of $20.5\,mm$ diameter. A scheme of the experimental apparatus used by Faghri and Bushko (1991) is shown in Figure 4.1.

Figure 4.1 – Experimental Apparatus.

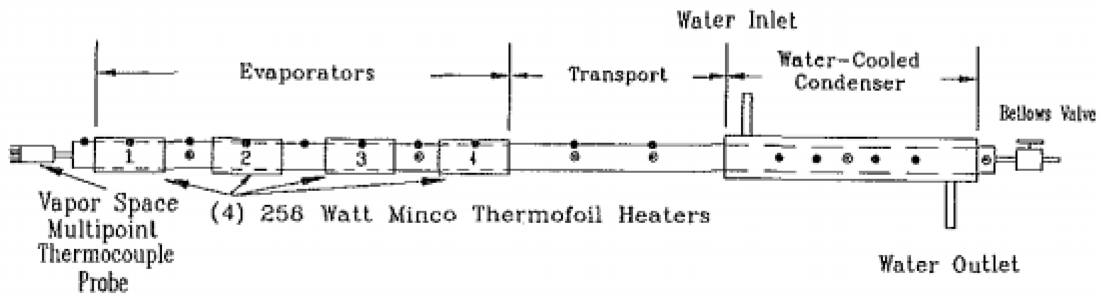

Experimental apparatus scheme, with four separate evaporators and condenser with water inlet/outlet.
Source: Faghri and Bushko (1991).

The heat pipe was modeled with 50 control volumes and fixed time step of $1x10^{-5}\,s$. The simulation was time dependent, so an elapsed time of $2000\,s$ from startup was considered enough to stabilization and allows the comparison of the numerical results with steady-state experiment performed by Faghri and Bushko (1991). The heat transfer coefficients used to adjust the simulations are presented in Table 4.1.

Each simulation of $2000\ s$ took approximately 78 minutes using a computer with an i5 processor with 2.5 GHz and 4 GB of RAM (Random Access Memory) in a 64 bits Operational System and routines written in FORTRAN.

Table 4.1 – Values of heat transfer coefficients used in numerical tests with one and two heat sources.

Parameter $[W/mK]$	Evaporator Zone	Condenser Zone
h_f	$-$	3000
$h_{wick,w}$	16000	16000
$h_{evap/cond}$	2250	4000

Source: The author.

4.1.1 Case with one heat load

In this first case, a total power input of $97\ W$ was applied on nodes 2 to 4, corresponding the evaporator length $6.35\ cm$. Forced convection was applied on the region of nodes 35 to 49, corresponding to the heat pipe condenser length of $30.00\ cm$. Adiabatic conditions were applied in the model for the rest of the pipe. The ambient temperature was considered to be $21.0\ ℃$, the same as in the experimental conditions. The locations of heat loads applied to the heat pipe are presented in Figure 4.2.

Figure 4.2 – Heat Loads Location for Case with One Heat Load.

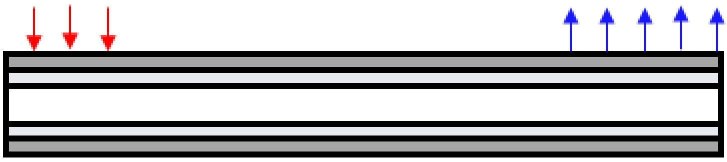

Representative locations of heat loads for Case 1.
Source: The author.

In Figure 4.3 it is presented the outer wall startup temperatures of the heat pipe, at first and last node of numeric model versus time, and it is possible to see that after about $1200\ s$ the system had reached steady-state. The simulation was left running for more time to check for stability of the algorithm after long periods, but no divergence was detected during the period of simulation.

Figure 4.3 – Wall Temperature versus Time for the Case with One Heat Load.

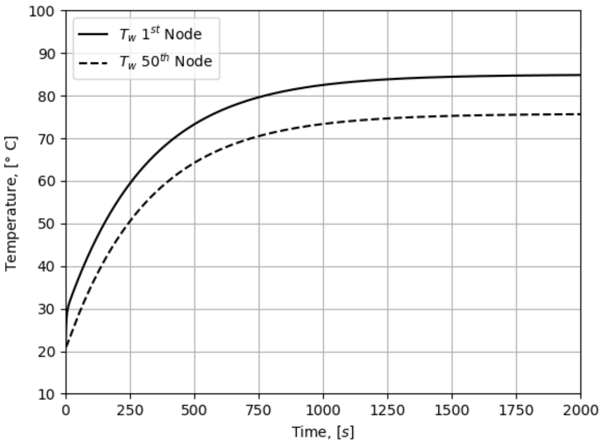

Temperature of the outer wall versus time on the first and last node of model.
Source: The author.

Figure 4.4 presents simulated temperatures of the wall and vapor and the comparison between with temperature profiles of the present study with numeric and experimental data from Faghri and Bushko (1991) in steady-state mode. It should be noted that the numeric model presented by Faghri and Bushko (1991) is a steady-state two-dimensional model. It can be seen a good agreement of both numeric model and experimental results.

It is possible to see a small deviation, within about $2\ ℃$ between present model and experimental data at the end of condenser. It can be explained by a peculiarity of the experimental apparatus (a scheme of the experimental apparatus used by Faghri and Bushko (1991) is shown in Figure 4.1, where a cooler system was used to force water to circulate along the condenser. The water being used to cool the condenser section exchanges heat with the heat pipe and loses efficiency until it reaches the end of condenser.

As expected, a peak in temperature of wall occur at evaporator while the temperature falls at condenser, and the temperatures of vapor remains almost constant along the pipe due to adiabatic conditions at the transport section.

Figure 4.4 – Temperatures Along Heat Pipe Axis for the Case with One Heat Load.

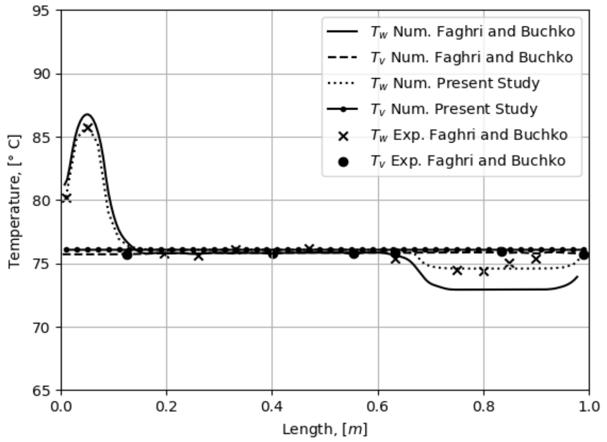

Temperature of the outer wall and temperature of vapor with a comparison between numeric model and experimental data for case with one heat load.
Source: The author.

Figure 4.5 shows the vapor velocity profile along the heat pipe axis, obtained from the developed model. It is possible to see a rise in the vapor velocity when it crosses the evaporator section, starting from zero at the left end cap of the tube. While the vapor passes through the adiabatic zone, almost no energy is exchanged between vapor and wick structure, which causes the velocity remain constant in this section. At condenser, the vapor loses energy and velocity through the section until it reaches zero velocity at the other end cap of the tube.

Figure 4.5 – Vapor Velocity Along Axis for the Case with One Heat Load.

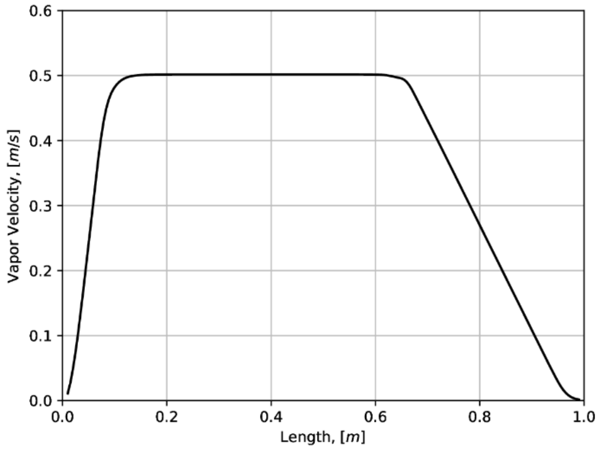

Velocities of the vapor versus axial location for case with one heat load.
Source: The author.

At last, Figure 4.6 shows the profile of radial mass flux of evaporation/condensation of fluid along the axis of the pipe. We can see a profile very similar to the wall temperature, which was already expected. At the evaporator, with higher wall temperatures due to heat load, we observe evaporation intensity profile along the evaporator length. At the condenser, with lower temperatures, it is possible to see condensation occurring. At the adiabatic zone, as expected, almost no net flux of mass is visible.

Figure 4.6 – Mass Flux Along Axis for the Case with One Heat Load.

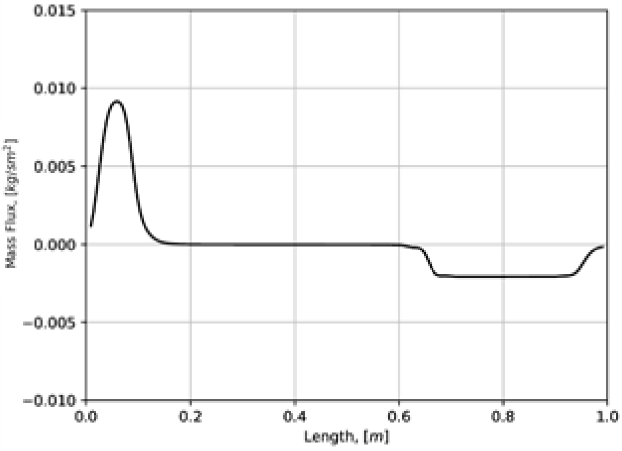

Mass flux of evaporation/condensation versus axial location for case with one heat load.
Source: The author.

The profiles of velocity and radial heat fluxes presented are from the present work while were not available in the source (FAGHRI; BUSHKO, 1991), therefore no comparison is possible. These results are presented for the purpose of the qualitative validation of the model.

4.1.2 Case with two heat loads

In this second case, two heat loads were simulated in accordance to available experimental setup (FAGHRI; BUSHKO, 1991). A total power input of $197\,W$ was distributed in 6 nodes, in which $99\,W$ was applied on nodes 2 to 4, corresponding the length of the first evaporator, and $99\,W$ was applied on nodes 9 to 11, corresponding the length of the second evaporator, each one measured $6.25\,cm$. Two adiabatic sections are presented in this case, a small one between the first and the second evaporator, and another between the second evaporator and the condenser. The locations of heat loads are presented in Figure 4.7.

Figure 4.7 – Heat Loads Location for the Case with Two Heat Loads.

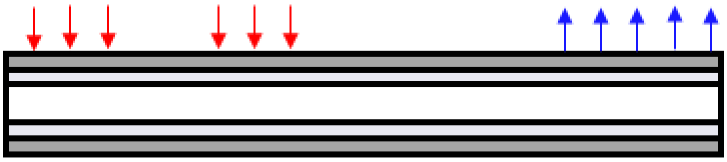

Representative locations of heat loads for case with two heat loads.
Source: The author.

Figure 4.8 shows the time dependent temperatures of the outer wall of the pipe at first and last node of numeric model. In this case, the system reached steady-state after $600\ s$, which is approximately two times faster than the case with one heat source. In this case, again there were no divergence observed during a long steady-state period.

Figure 4.8 – Time Dependent Wall Temperatures for the Case with Two Heat Loads.

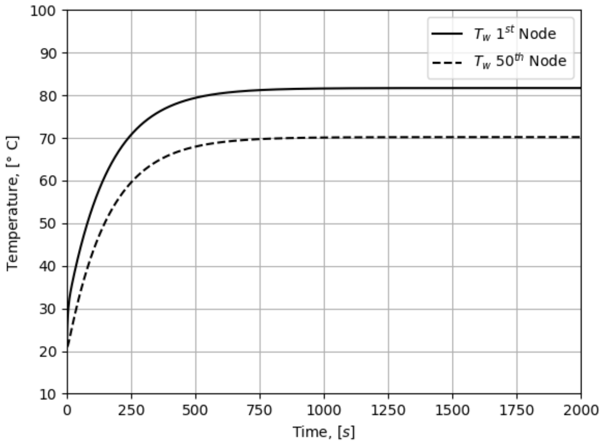

Temperature of the outer wall versus time on the first and last node of model.
Source: The author.

Figure 4.9 shows the temperatures of the wall and vapor of the present study in steady-state condition and the comparison between the temperatures obtained with of the present numeric model and temperatures given by Faghri and Bushko (1991). As expected, here it is possible to see two peaks in temperature of wall at evaporator locations.

Figure 4.9 – Temperatures Along Axis for the Case with Two Heat Loads.

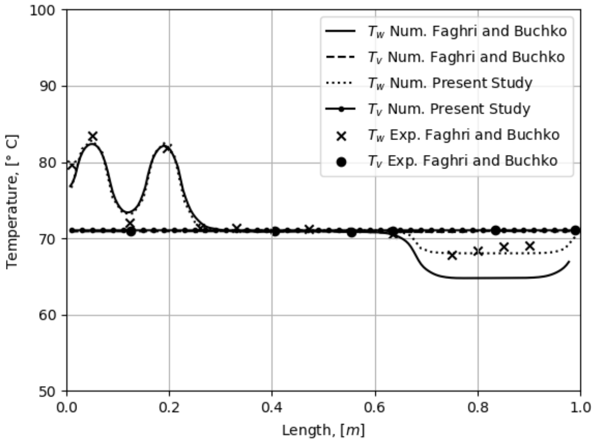

Temperature of the outer wall and temperature of vapor with a comparison between numeric model and experimental data for case with two heat loads.
Source: The author.

For this section of two evaporators, the results obtained with the developed one dimensional model diverge from the results of the referred two dimensional model by not more than 0.3 ℃, and both models match experimental data as close as within about 1.0 ℃. In the condenser section, the present model did not include the cooler heat exchanger, wherefore the deviation from experimental data was about 2.0 ℃, versus about 0.3 ℃ of the referred model.

In Figure 4.10, the velocity profile of vapor along the axis of the pipe is shown. Here we can see a first rise in the vapor velocity when it crosses the first evaporator section and after a little inclination, a second rise in velocity as it crosses the second evaporator section, starting from zero at the end cap of the tube. The subsequent path of vapor is almost identical in shape for case with two heat loads as it was for case with one heat load, but with more than double of the velocity. This behavior was qualitatively expected as the evaporation intensity falls down significantly between two evaporators. Passing through the adiabatic zone, no change in velocity is visible. However, at condenser, again, the vapor loses energy and velocity through the section until it reaches zero velocity at the condenser end cap of the tube.

Figure 4.10 – Vapor Velocity Along Axis for the Case with Two Heat Loads.

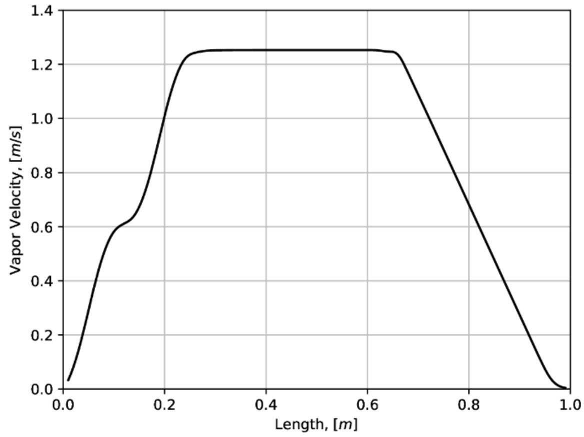

Velocities of the vapor versus axial location for case with two heat loads.
Source: The author.

The maximum vapor velocity takes place in the adiabatic section. The Reynolds number calculated for this condition is $Re = 427$, that confirms the laminar flow in the heat pipe vapor core.

The radial mass flux profile of evaporation/condensation is showed in Figure 4.11. The profile is similar to the wall temperature, as expected. At both evaporator zones, we see two peaks of the evaporation occurring.

Figure 4.11 – Mass Flux Along Axis for the Case with Two Heat Loads.

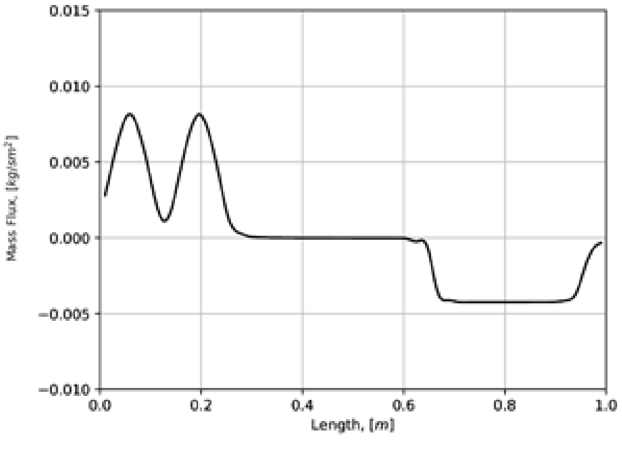

Mass flux of evaporation/condensation versus axial location with two heat loads.
Source: The author.

Due to high thermal conductivity at wall, it is possible to observe the evaporation occurring even with a small intensity between the evaporators, where heaters were not applied.

This and other qualitative details give a confidence on the model ability to correctly represent all physical processes occurred inside the heat pipe during its operation. It is also important to underline, that the numerical algorithm was not changed for the cases of unique or multiple heat sources, just input data of heat load locations have to be changed.

4.2 Validation 2: evaluation of the presence of noncondensable gas

An important phase of the overall model validation process is the model verification in the case of transient startup of the heat pipe with noncondensable gas. An experimental heat pipe presented by Saad et al. (2012) was modeled. The pipe is made of copper and filled with water as working fluid presented. The heat pipe has length of $0.35\,m$, and the shell is $1.65\,mm$ thick, the wick is composed of 4 layers of copper wire screen mesh with wire diameter of $0.109\,mm$, and the vapor core has $14.88\,mm$ diameter. A small amount of $1.45\ x\ 10^{-6}\ kg$ of air was introduced inside the heat pipe to act as a noncondensable gas. The heat pipe was heated thorough an aluminum annular section, with a length of $101.6\,mm$ and outer diameter of $88.9\,mm$ clamped at the evaporator section. A scheme of the experimental apparatus used by Saad et al. (2012). is shown in Figure 4.12.

Figure 4.12 – Cross-section of the Heat Pipe Loaded with Noncondensable Gas.

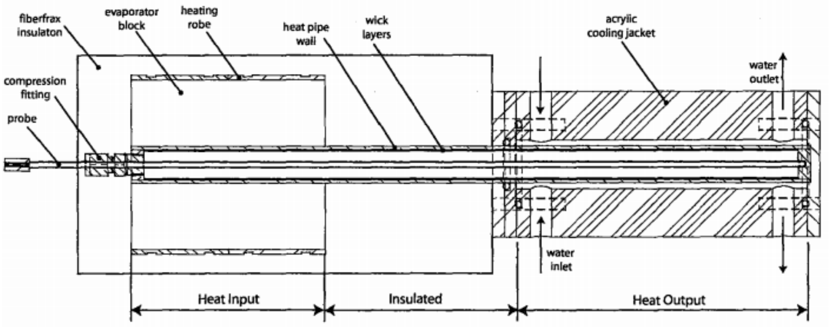

Scheme of the heat pipe section of experiment performed by Saad (2006).
Source: Saad (2006).

The heat pipe mode has 35 control volumes along the length. A power input of $100\,W$ was applied on nodes 1 to 10, corresponding the length of evaporator of $101.6\,mm$. Forced convection was applied on nodes 21 to 35, corresponding to the condenser length of $150.0\,mm$. Adiabatic conditions were applied for the rest of the pipe. The ambient temperature and fluid temperature flowing outside the condenser was considered to be $20°\mathrm{C}$, in accordance to experimental conditions. The aluminum block was modeled with one node in the radial direction and 10 nodes in the axial direction. The parameters used to model the heat transfer process in the heat pipe are presented in Table 4.2.

The entire simulation of $12000\,s$ (with a time step of $5\,x\,10^{-6}\,s$) took approximately 648 minutes using a computer with an i5 processor with 2.5 GHz and 4 GB of RAM.

Table 4.2 – Values of heat transfer coefficients used in numerical tests with noncondensable gas.

Parameter $[W/mK]$	Evaporator Zone	Forced Convection Zone
h_f	$-$	3000
$h_{wick,w}$	3000	3500
$h_{evap/cond}$	3000	3500
$h_{h,b}$	25000	$-$

Source: The author.

Figure 4.13 shows the obtained mean time dependent temperatures at the evaporator and condenser of the outer wall of the pipe during the heat pipe startup and heating period (from 0 to $3000\,s$) and then during shutdown and passive cooling. For the comparison, in this graph is also present the results obtained with a network model and experimental data presented by Saad et al. (2012).

The present study shows a good agreement with experimental data in the heating period and cooling period (3000 to $6000\,s$). The present model gets to have a small deviation of about within $1.0\,℃$ from the experimental data after $6000\,s$ in the evaporator section, which could be due to the aluminum block being modeled with only one node in the radial direction.

Figure 4.13 – Time Depentend Temperature of Wall With Noncondensable Gas.

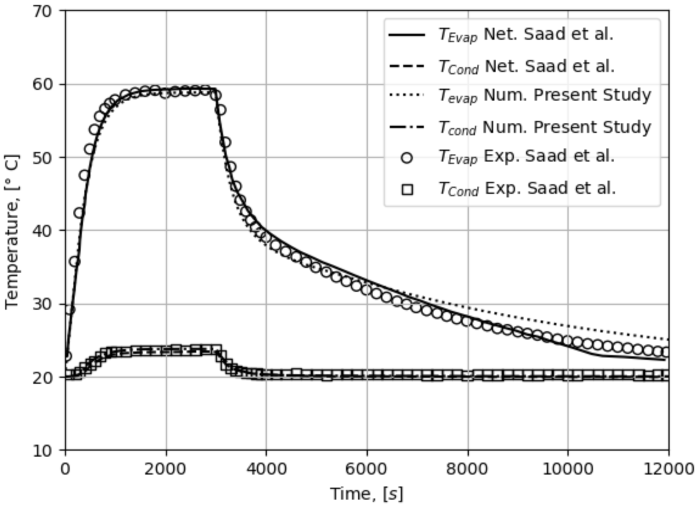

Temperature of the outer wall versus time. Presented temperature is the average of evaporator/condenser temperatures.
Source: The author.

Figure 4.14 presents the temperatures of the outer wall and the comparison between the temperatures of the present study with the network model and experimental data from Saad et al. (2012) in steady-state mode. It is noted a small delay of approximately $3.0\ ℃$ from experimental data in temperature on both, present study and network model, but both models agree with experimental data for longer times. The presence of noncondensable gas migrating to the condenser becomes more evident over time.

Figure 4.14 – Temperature distribution along axis for selected times.

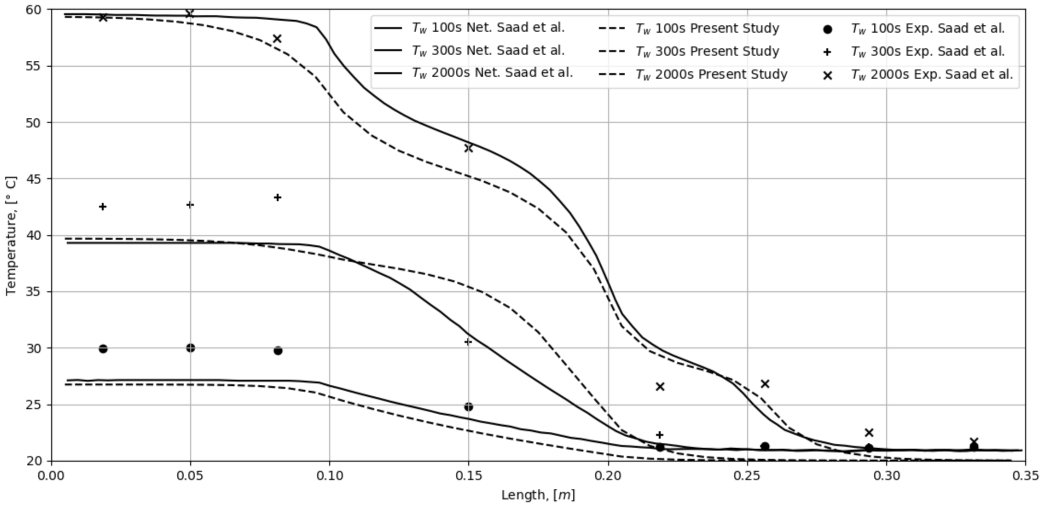

Outer wall temperature distribution along axis for selected times, with comparison between numerical and experimental results.
Source: The author.

The present model was able to represent dynamic of the internal diffusion vapor-gas front developing and then stabilization confirmed by the experimental data. The average deviations from the temperature experimental points were the following: $\Delta T = 1.6\ ℃$ at $t = 100\ s$, $\Delta T = 2.1\ ℃$ at $t = 300\ s$ and $\Delta T = 1.2\ ℃$ at $t = 2000\ s$.

4.3 Validation 3: symmetry test of numerical model

In general, in the research line of heat pipes modeling, the usual approach is to fix the exact position of evaporator and condenser. If one gets a look on many published papers on this matter, most of sources present a predefined numerical domain with exact boundaries between evaporator, adiabatic section, and condenser (a usual layout is the evaporator on the left end, and the condenser on the right end of heat pipe). Such a fixed layout yields various simplifications on numerical algorithm creation. Particularly, numerical scheme for velocities can be set always along flow, without any specific treatment of possible change in velocity direction.

When we think about space applications of heat pipes for thermal stabilization of satellite structural panels, the position of evaporators and condensers can change along time considering that some of equipment, installed on the panel with embedded heat pipes, may be suddenly switched on and off (or come to stand-by mode) during orbit or along entire mission. Therefore, the numerical model shall be able to process arbitrary changes in velocity direction and pressure distribution along heat pipe length.

Moreover, the heat pipe may have several eventual evaporator zones and condenser zones. It is not a trivial feature for any heat pipe model and shall be well tested. Such verification we call here as a symmetry test.

For the symmetry test, nine different heat loads were simulated with and without presence of noncondensable gas inside the pipe, totalizing 18 different combinations. All cases simulate a heat pipe made of copper filled with water with length of $1\,m$ and modeled with 50 nodes. The heat pipe shell is $1.7\,mm$ thick, the wick is $0.7\,mm$ thick and, the vapor core has $20.5\,mm$ diameter. Ambient temperature is $21.0\,℃$, except for cases 5 and 6 where ambient temperature is $0\,℃$. When noncondensable gas is present, it was considered a mass of $1.5\,x10^{-6}\,kg$ of air.

Table 4.3 – Location of Evaporator and Condenser Nodes of Symmetry Test.

Symmetry Case	Evaporator Nodes	Condenser Nodes
1	$1-10$	$41-50$
2	$41-50$	$1-10$
3	$21-30$	$1-5;\ 46-50$
4	$1-5;\ 46-50$	$21-30$
5	$-$	$41-50$
6	$-$	$1-10$
7	$1-10$	$-$
8	$41-50$	$-$
9	$1-10;\ 21-30;\ 41-50$	$11-20;\ 31-40$

Source: The author.

A total power input of $50\,W$ was distributed along the nodes of the evaporator (or evaporators, for multiple heat loads), and different location of condenser zones were attributed as shown in Table 4.3, and a visual representation of the locations were heat loads were applied can be seen in Figure 4.15. Forced convection was applied on condenser nodes and adiabatic conditions were considered for the rest of the pipe.

All results in symmetry test are exhibit for an elapsed time of $2000\,s$ of heat pipe operation, when steady-state condition was already achieved. The exception is for cases 5,6 (case with no heating), and 7,8 (case with no cooling), where only fast transients were simulated.

Each run took approximately 78 minutes to simulate $2000\,s$ of operation (with a time step of $1x10^{-5}\,s$), using the same computer.

Figure 4.15 – Representation of Heat Load Locations for Symmetry Test.

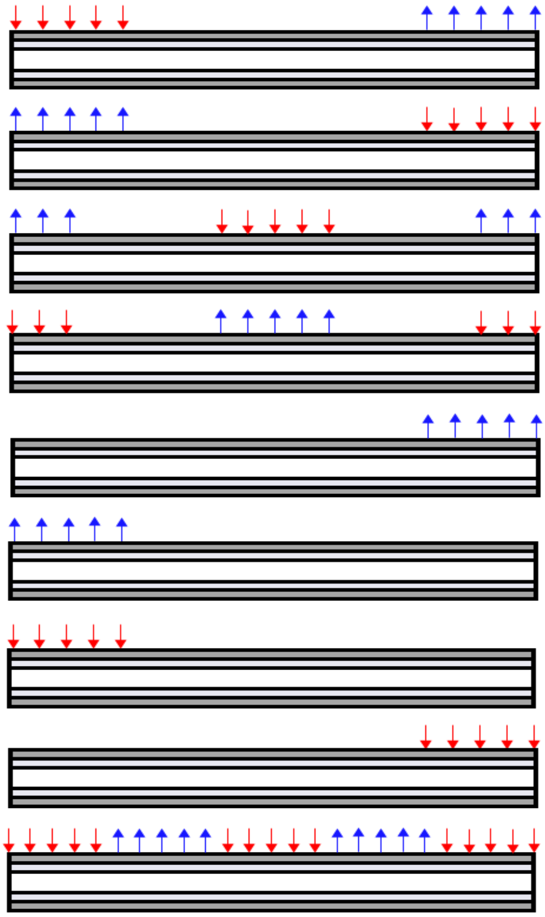

Case 1: canon layout, evaporator at left and condenser at right

Case 2: inverse layout, condenser at left and evaporator at right

Case 3: central evaporator and two condenser at sides

Case 4: central condenser and two evaporators at sides

Case 5: transient on sudden cooling on the right end

Case 6: transient on sudden cooling on the left end

Case 7: transient on the right end heat load switched-on

Case 8: transient on the left end heat load switched-on

Case 9: multiple evaporators and condensers

Representative locations of heat loads for the three cases of Symmetry Test.
Source: The author.

4.3.1 Symmetry test of cases 1 and 2

Case 1 and Case 2 were modeled as a heat pipe considering a heat load application with one evaporator and cooling with one condenser, at both ends of pipe. Figure 4.16 shows the temperature and axial velocity along the axis. The simulations have been obtained in transient mode and were extended until steady-state was achieved. Each graph below show results obtained from both cases, when heat loading occurs at the left and at the right ends of the heat pipe. In the temperature, it is possible to observe a distortion caused by the presence of noncondensable gas, the condenser blocked by the gas gets colder in comparison with the case without gas. In velocity profile, we can see mixture velocity approaches to zero earlier in the condenser zone due to vapor blockage at the cold end of pipe in each case. Figure 4.17 shows vapor and noncondensable gas density distribution along the axis in steady-state for both cases.

Figure 4.16 – Wall Temperature and Axial Velocity Along Axis for Cases 1 and 2.

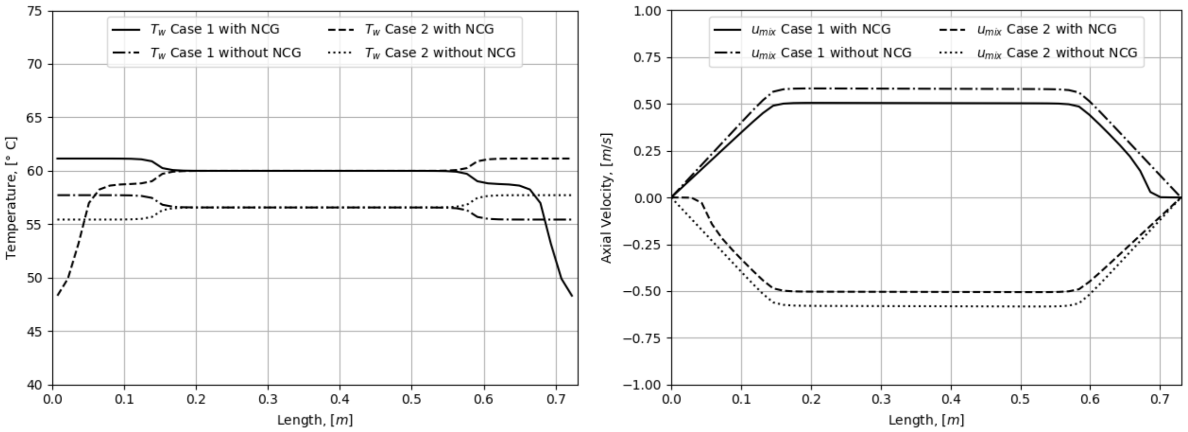

Source: The author.

Figure 4.17 – Vapor and Gas Distribution Along Axis for Cases 1 and 2.

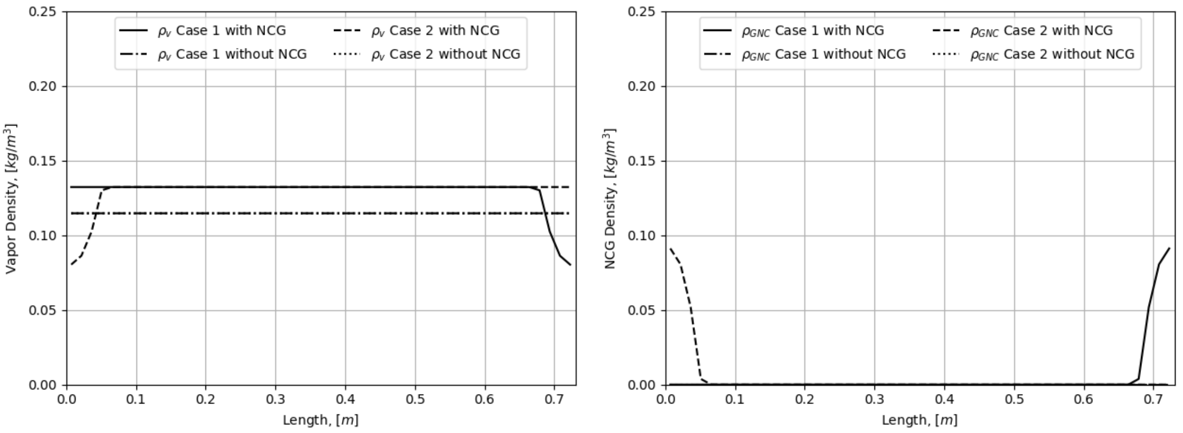

Source: The author.

The obtained results show the absolute symmetry in profiles of all variables for both cases, left-to-right, and right-to-left when velocity gets opposite signal. No correction of algorithm and computer code was needed. It demonstrates the important feature of the developed model: the ability to accommodate the sudden and arbitrary changes in velocity direction at any local of heat pipe.

4.3.2 Symmetry test of case 3

Case 3 was modeled with two condensers at both ends of the pipe and a heat load application in the center. Figure 4.18 shows the temperature and axial velocity along the axis. In temperature, again is possible to see distortions caused by the noncondensable gas at both ends, but the temperature drop is lower compared to cases 1 and 2 because here the same amount of gas is distributed in both sides of the pipe. Velocities approach to zero slightly before end of pipe, as excpected, due to noncondensable gas concentration at the condenser ends of pipe. It is interesting to note a zero velocity in the middle of the pipe, at the central evaporation zone. This case can be seen as two different heat pipes with half the length attached side by side. Figure 4.19 shows vapor and noncondensable gas distribution along the axis in steady-state.

Figure 4.18 – Wall Temperature and Axial Velocity Along Axis for Case 3.

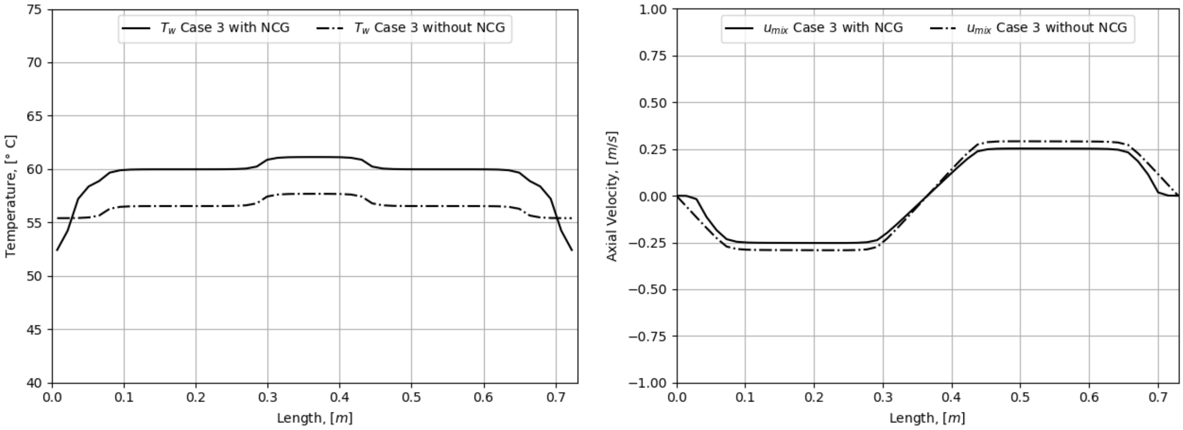

Source: The author.

Figure 4.19 – Vapor and Gas Distribution Along Axis for Case 3.

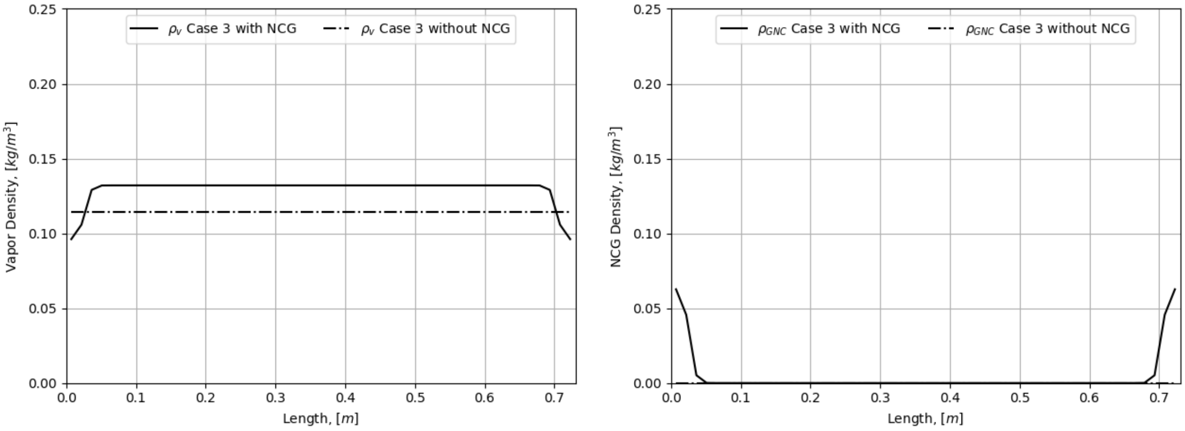

Source: The author.

The simulation demonstrates the ability of the developed model to deal with interchanged velocity directions at unique physical process for both sub-cases, with and without noncondensable gas. This feature is important in heat pipe simulations for space applications. A heat pipe inserted into satellite structural honeycomb panels, usually features this eventual heating/cooling configuration, with some colder conditions at two pipe ends.

4.3.3 Symmetry test of case 4

Case 4 was simulated the configuration with two evaporators at the ends of the pipe and a single condenser in the center. Figure 4.20 shows the temperature and axial velocity profile along the axis at the steady-state. In the temperature profile, we observe an unusual temperature drop because of the noncondensable gas affects the vapor condensation in the center of the pipe. In axial velocity profile, we can see a relatively large zone of velocities approaching to zero due to noncondensable gas concentration in the center of the pipe, however again this blocked zone does not occupy the entire length of condenser, only part of it.

Figure 4.20 – Wall Temperature and Axial Velocity Along Axis for Case 4.

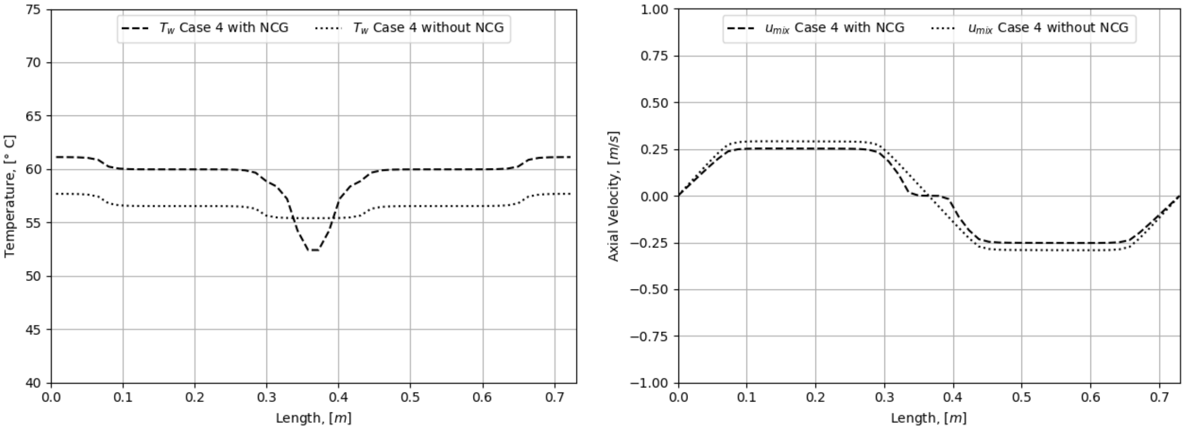

Source: The author.

Figure 4.21 shows vapor and noncondensable gas distribution along the heat pipe axis in steady-state.

Figure 4.21 – Vapor and Gas Distribution Along Axis for Case 4.

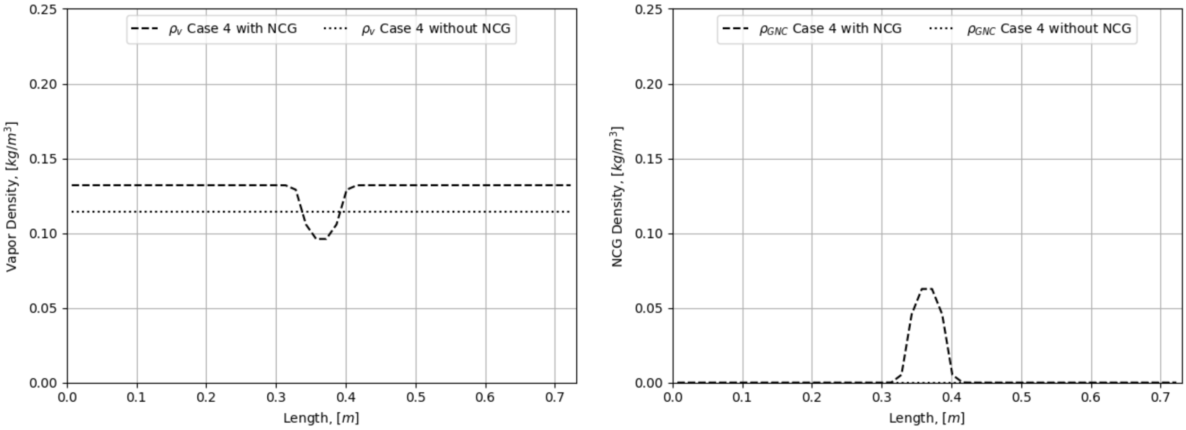

Source: The author.

In Figure 4.21 (left) it is interesting to see how the vapor density in the heat pipe with noncondensable gas drops below the vapor density constant level compared to heat pipe without noncondensable gas.

The conducted test demonstrates the ability of the model to simulate such an unusual configuration as accumulating of noncondensable gas in the center of the heat pipe. It is important to note that such a configuration is quite common in heat pipe applications for thermal stabilization of the satellite panels, however, it is a very atypical one from the point of view of heat pipe modeling. Up to now, there is no publications have found on such a feature in the heat pipe in presence of noncondensable gas modeling, neither in steady-state nor in transient modes.

4.3.4 Symmetry test of cases 5 and 6

Due to some specific space applications, there are cases in which the condenser starts cooling before or without any evident application of a heat load on the heat pipe. Cases 5 and 6 simulate a specific transient mode named as a startup by cooling, where no area for evaporator is dedicated. Figure 4.22 shows the temperature and axial velocity profiles along the axis after $2000\,s$ since the startup through the left or right end of heat pipe being suddenly cooled. Figure 4.22 (left) shows the heat pipe without noncondensable gas reached steady-state ($\Delta T < 0.01$ ℃ between condenser and adiabatic zone) after this period, but the heat pipe with noncondensable gas still not achieve the steady-state due to blockage of cooling section by gas.

Figure 4.22 – Wall Temperature and Axial Velocity Along Axis for Cases 5 and 6.

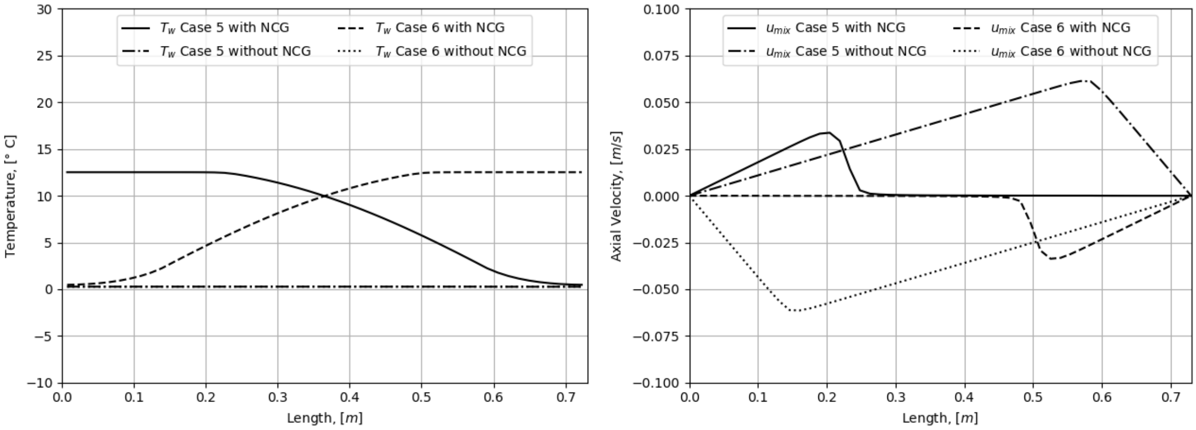

Source: The author.

In this last case, the cooling occurs mainly by conduction through the heat pipe wall, and the process goes very slowly. Figure 4.22 (left) shows that velocity at heat pipe without noncondensable gas did not reached steady-state, even with such small temperature gradients. Future analysis need to be conducted in order to check stability on this particular case.

Figure 4.23 shows vapor and noncondensable gas distribution along the axis after $2000\,s$ of operation. Due to small temperature gradient, the pressure difference across the length of the pipe was also small and was not enough to compress the noncondensable gas to the ends of the pipe. This small pressure difference is also the reason for such small velocities if compared with other cases.

Figure 4.23 – Vapor and Gas Distribution Along Axis for Cases 5 and 6.

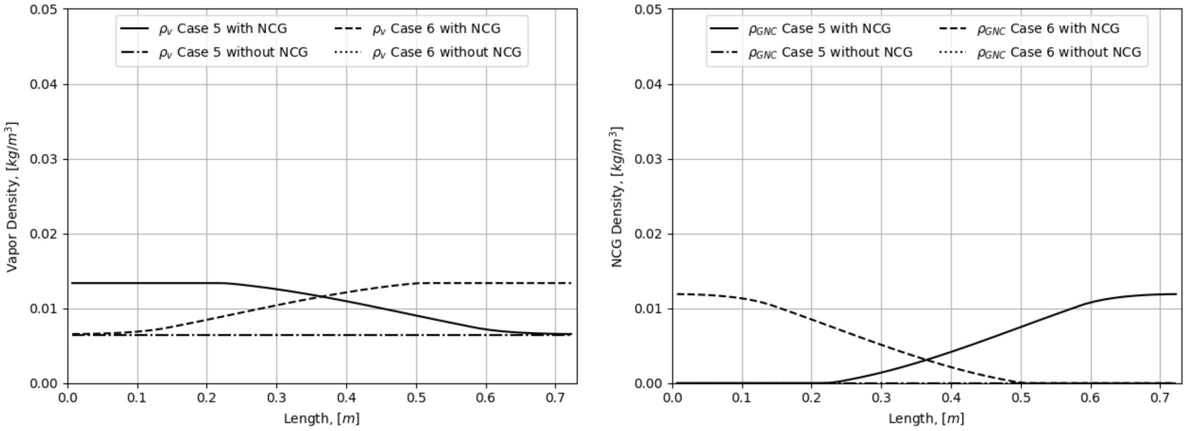

Source: The author.

Once again, a heat pipe startup by cooling may occur in space application, for example, the heat load, attached to one heat pipe end, is in switching-off conditions, and a space radiator, attached to opposite heat pipe end, get sudden cooling when satellite leaves Sun-illuminated phase and enters eclipse period of the orbit. Nevertheless, the performed bibliographic search through available sources shows that such a transient simulation of startup by cooling was never studied.

4.3.5 Symmetry test of cases 7 and 8

Cases 7 and 8, were modeled due to some specific space applications, where the cooling conditions are not provided or temporarily not available and a heat load is applied to the pipe. These cases are purely transient because steady-state can never be reached due to the absence of a condenser. Figure 4.24 shows the temperature and axial velocity profiles along the axis after $2000\,s$ since hot startup. Figure 4.25 shows vapor and noncondensable gas density distribution along the axis in $2000\,s$ of operation.

Figure 4.24 – Wall Temperature and Axial Velocity Along Axis for the Cases 7 and 8.

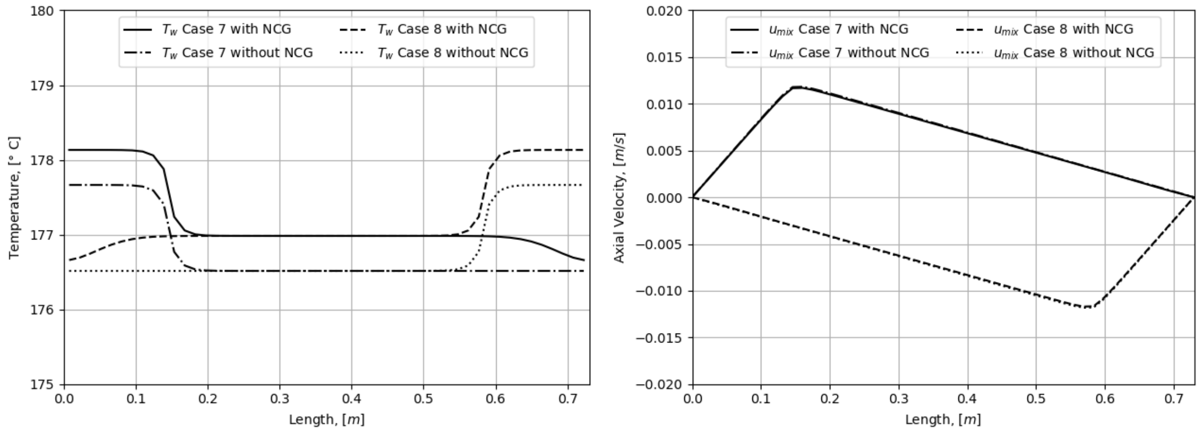

Source: The author.

Figure 4.25 – Vapor and Gas Distribution Along Axis for Cases 7 and 8.

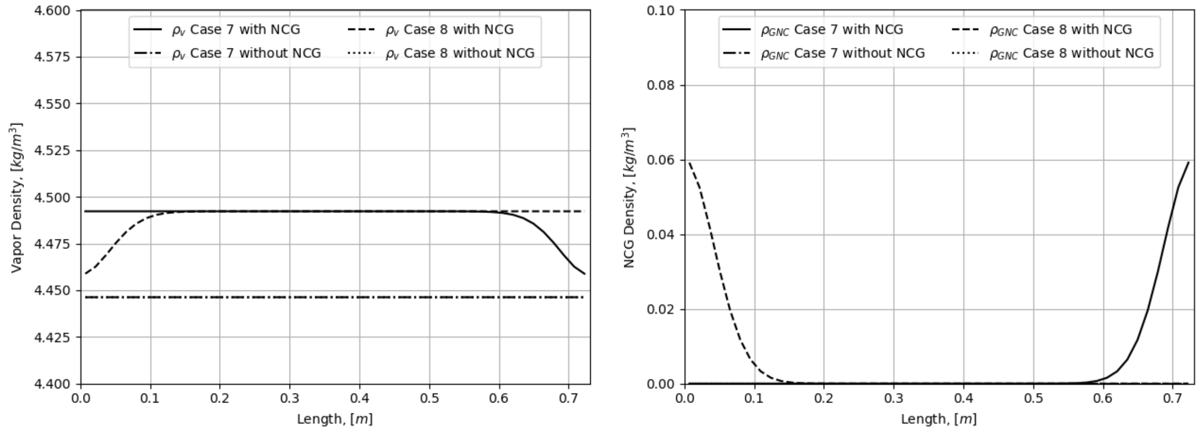

Source: The author.

As soon as the heat pipe was heating without any cooling, one can see very high temperatures were achieved in after $2000\ s$, as expected. In these cases, it would be more interesting to see fast transient results, soon after startup. Figure 4.26 and Figure 4.27 show the same profiles after $100\ s$ since the startup.

Figure 4.26 – Wall Temperature and Axial Velocity Along Axis for the Cases 7 and 8.

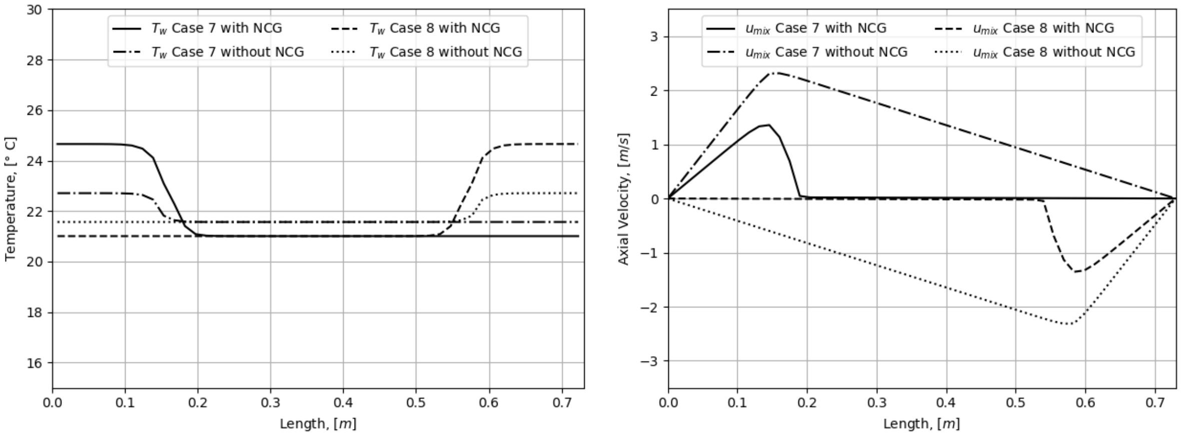

Source: The author.

Figure 4.27 – Vapor and Gas Distribution Along Axis for Cases 7 and 8.

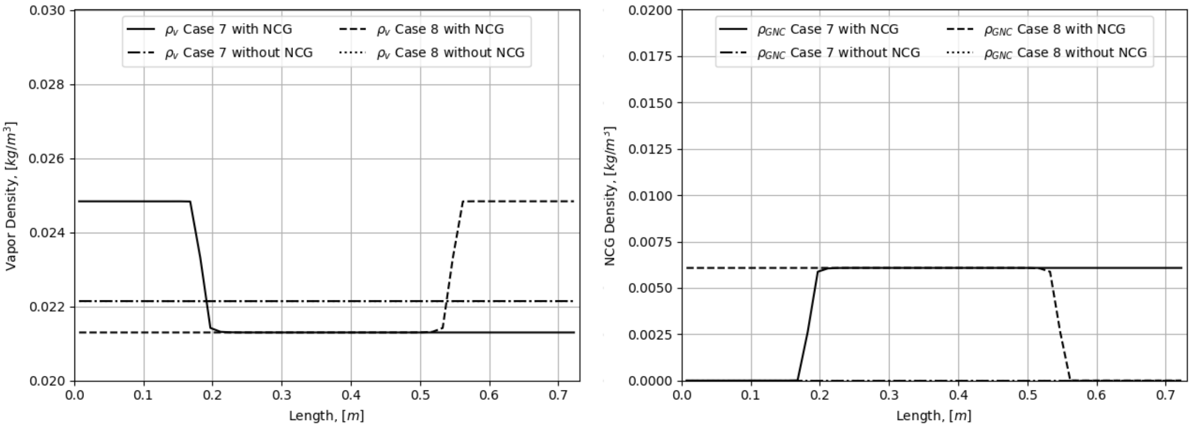

Source: The author.

The results presented in this section demonstrate the ability of the model to simulate fast transient processes into heat pipe on sudden heat load application without any cooling. The heat pipe may contain or not contain noncondensable gas, and heating may occurs either from left or right end of heat pipe.

4.3.6 Symmetry test of case 9

Case 9 was modeled with two condensers and three evaporators to check a most typical heat pipe heating/cooling configuration of application for satellite panel thermal stabilization. It is important also to check if the model is able to deal with a higher number of different boundary conditions and heat loads. Figure 4.28 shows the temperature and axial velocity along the axis. Figure 4.29 shows vapor and noncondensable gas distribution along the axis in steady-state.

Figure 4.28 – Wall Temperature and Axial Velocity Along Axis for Case 9.

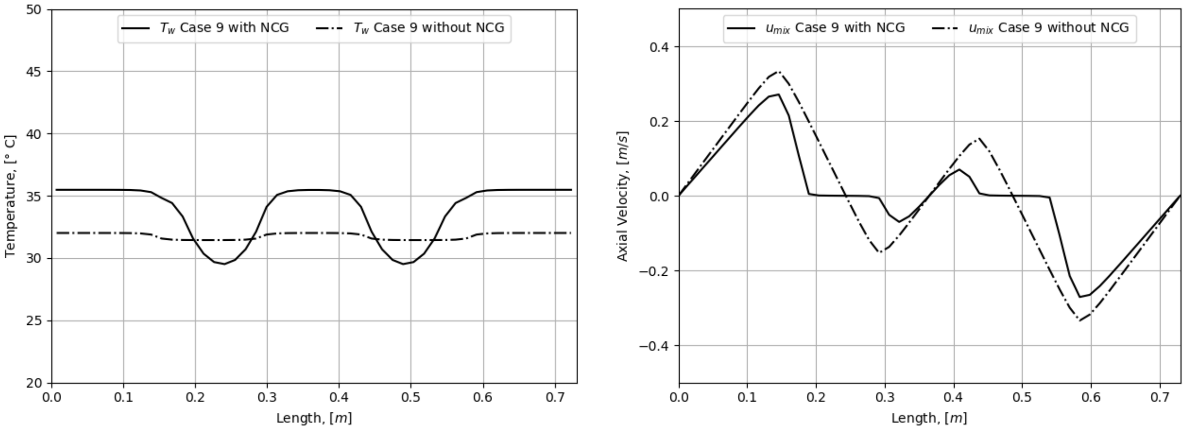

Source: The author.

Figure 4.29 – Vapor and Gas Distribution Along Axis for Case 9.

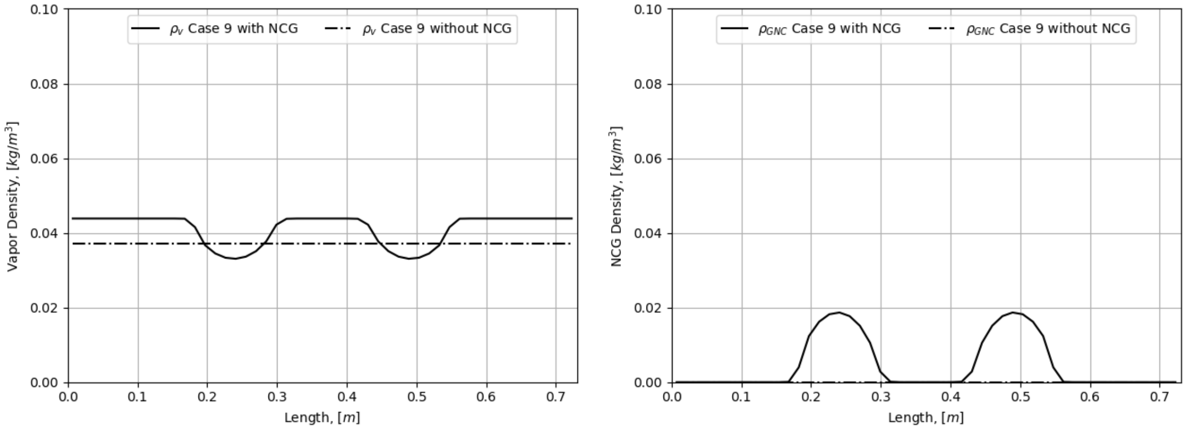

Source: The author.

Finally, it was proved the model is capable to simulate any possible configuration of multiple heating/cooling zones and to predict the adequate and dynamic distributions of all internal variables, including velocity, density, pressure and temperature for transient and steady-state modes, with and without noncondensable gas.

5 EXPERIMENTAL SETUP

This chapter will present the experimental setup used, as well as the characteristics of heat pipes and fluids.

5.1 Heat pipe characteristics

The experiments were performed using two identical heat pipes with axial rectangular grooves heat pipes made of aluminum alloy 6063 T6. Both heat pipes had the same characteristics with $19\,mm$ outer diameter and a length of $730\,mm$ with wall and wick thickness of $1.44\,mm$ and $1.81\,mm$ respectively. The rectangular grooves had width of $1.37\,mm$ and are evenly spaced by $1.37\,mm$. The 22 rectangular grooves had average width of $1.23\,mm$ and are evenly spaced by $1.37\,mm$. The cross-section of the pipe can be seen in Figure 5.1, this figure shows the original draw and an optical scan of the profile.

Figure 5.1 – Heat Pipe Cross-Section Profile.

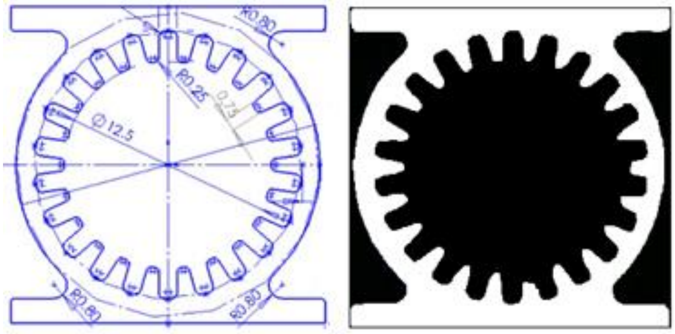

Source: The author.

Both heat pipes were charged with $22.45\,g$ of ammonia and one of the pipes received an additional charge of $0.33\,g$ of argon as noncondensable gas. The argon charge was measured indirectly through pressure and temperature during charging ($1.6\,bar$ at $296\,K$).

5.2 Experimental setup

To measure the temperature in outer wall of the heat pipe 17 T-type thermocouples were positioned along the pipes as shown in Figure 5.2. The thermocouples were fixed on the wall with Kapton tape. Ambient temperature was measured using an additional thermocouple.

Figure 5.2 – Thermocouple Locations.

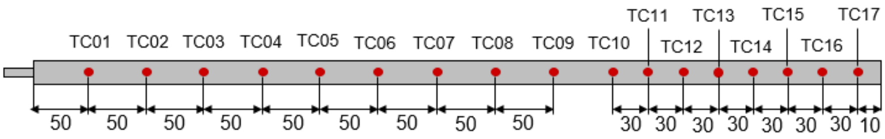
TC01
TC02
TC03
TC04
TC05
TC06
TC07
TC08
TC09
TC10
TC11
TC12
TC13
TC14
TC15
TC16
TC17
50 50 50 50 50 50 50 50 50
30 30 30 30 30 30 30 10

Source: The author.

The heat pipes were heated using two MINCO HK5160R44.0 skin heaters connected in parallel with an equivalent resistance of $22\ \Omega$ (Figure 5.3). The heaters were fixed under the face of a rectangular polymer block which was fixed to the pipe with two aluminum clamps. The heating block with heaters are positioned relative to the heat pipe as shown in Figure 5.4.

Figure 5.3 – Heating Block.

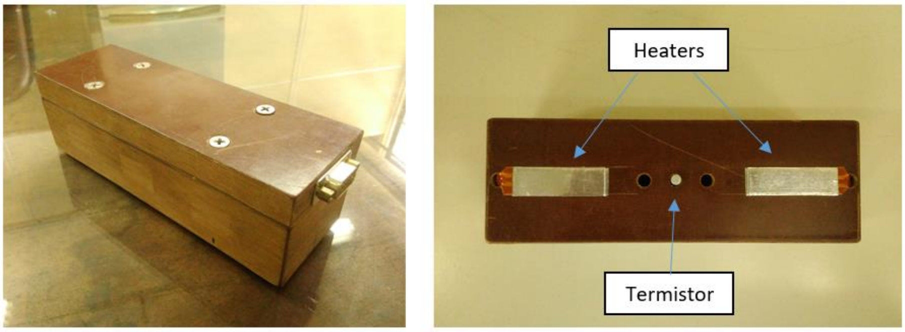
Heaters
Termistor

Source: The author.

Figure 5.4 – Heating Block Location.

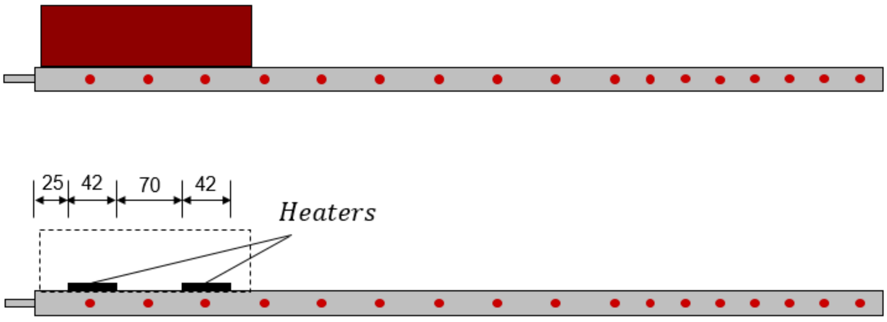
25
42
70
42
Heaters

Source: The author.

Electrical power to the heaters were supplied by a Tectrol TCA-120-20 power source (Figure 5.5). Thermocouple and power data were measured using a desktop computer connected to an Agilent 34970A (Figure 5.6) Data Acquisition Switch Unit sampling at every $2\ s$ throughout the experiment.

Figure 5.5 – Power Source Tectrol TCA 120-20.

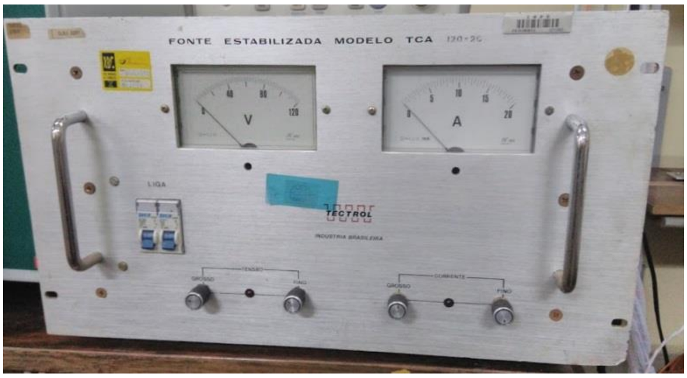

Source: The author.

Figure 5.6 – Data Acquisition System.

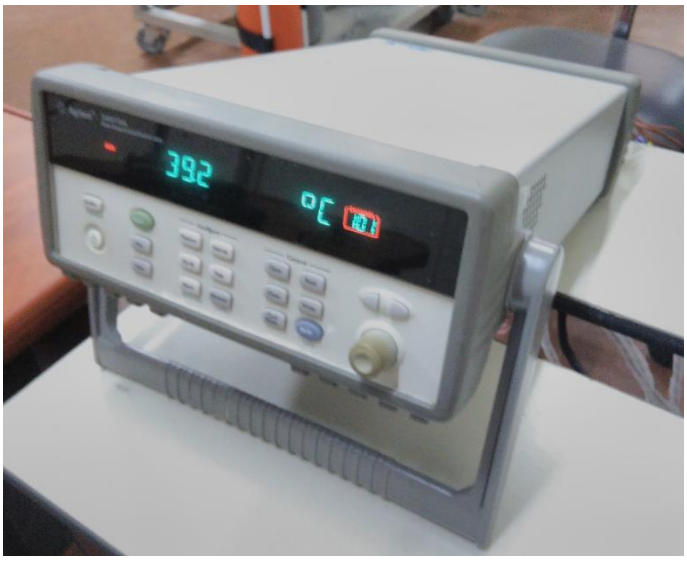

Source: The author.

All experiments were performed with the heat pipes mounted in the horizontal orientation and two different cooling methods were used. In the first method, the heat pipes were cooled through free convection at initial $510\,mm$ of the pipe and by forced convection with a Honeywell DT-73E Fan on subsequent $220\,mm$ of pipe. In the second method, heat pipes were cooled by free convection through the entire length of the condenser. The Honeywell DT-73E Fan provides a steady flow of $220\,CFM$ (ft^3/s), equivalent to a flow of $0.1085\,m^3/s$ or a flow velocity of $6.01\,m/s$

Figure 5.7 shows the general schematics of the experimental setup and Figure 5.8 shows a mounted heat pipe with heating block and thermocouples.

Figure 5.7 – Experimental Diagram.

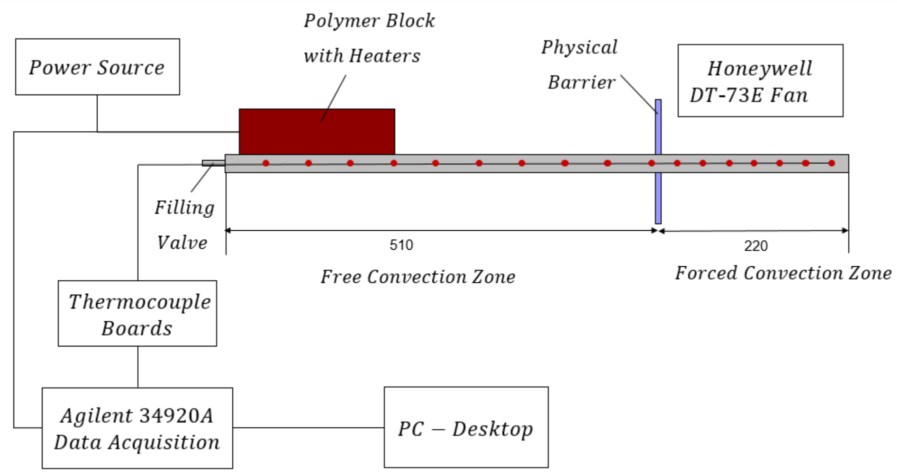
Power Source
Polymer Block with Heaters
Physical Barrier
Honeywell DT-73E Fan
Filling Valve
510
220
Free Convection Zone
Forced Convection Zone
Thermocouple Boards
Agilent 34920A Data Acquisition
PC – Desktop

Source: The author.

Figure 5.8 – View of the Experimental Setup.

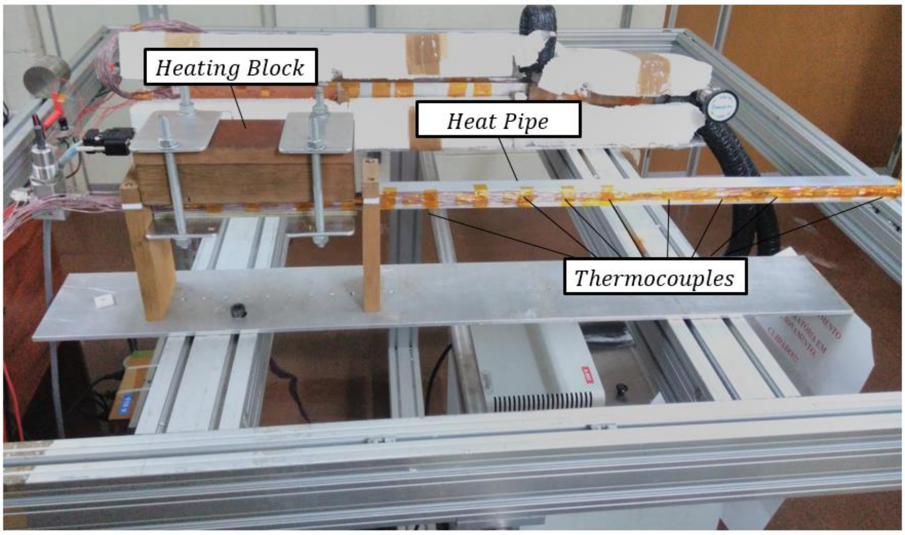
Heating Block
Heat Pipe
Thermocouples

Source: The author.

5.3 Experimental setup error analysis

A method for uncertainty analysis was presented by Kline and McClintock (1953), in which the uncertainty of a parameter R, function of $x_1, x_2 \ldots x_n$ is given by:

$$w_R = \left[\left(\frac{\partial R}{\partial x_1} w_1\right)^2 + \left(\frac{\partial R}{\partial x_2} w_2\right)^2 + \cdots + \left(\frac{\partial R}{\partial x_n} w_n\right)^2\right]^{1/2}, \tag{5.1}$$

where w_R is the uncertainty of R, w_1 is the uncertainty of x_1, w_2 is the uncertainty of x_2, w_n is the uncertainty of x_n.

Thermocouples of T type have nominal uncertainty of $\pm 1.0\ ℃$ for the temperature range in which tests were conducted. Considering the ambient temperature of $25\ ℃$, the relative uncertainty will be 0.17%.

For heat pipe tests, the temperature difference is more important than the absolute temperature, so should be taken into account the measurement variation without the absolute error. Therefore, the uncertainty related to temperature difference will be expressed as:

$$w_{\Delta T} = \sqrt{\left(\frac{\partial \Delta T}{\partial T} w_T\right)} = 1.0\ ℃. \tag{5.2}$$

Random uncertainties, need to be taken into account, which are ruled by a statistic distribution. For a confidence level of 95%, two standard deviations above or below the average (2σ) is used for calculations. From experimental data, the oscillations around the average do not exceed $w_{dT} = 0.1\ ℃$.

Another uncertainty is related to the data acquisition system. From manual, the precision given by the equipment is 0.01% at any channel, temperature included, which results in $w_{DAS} = 0.03\ ℃$.

The temperature measurement precision is also influenced by the uncertainties on the precision of power measurements:

$$w_{\Delta T,P} = \sqrt{\left(\frac{\partial \Delta T}{\partial P} w_P\right)}, \tag{5.3}$$

where the derivative $\partial \Delta T / \partial P$ is obtained from experimental tests. Appling a heat load of $75\ W$ to the pipe will rise the temperature of pipe from $23\ ℃$ to $60\ ℃$, which yields:

$$\frac{\partial \Delta T}{\partial P} \approx \frac{(60 - 23)}{75} = 0.49. \tag{5.4}$$

The uncertainty related to the power dissipation of heaters will be taken into account with the uncertainties in heater voltage and current, according to:

$$w_P = \left[\left(\frac{\partial P}{\partial V} w_V\right)^2 + \left(\frac{\partial P}{\partial I} w_I\right)^2\right]^{1/2}, \tag{5.5}$$

where w_P is the uncertainty in power, w_V is the uncertainty in voltage and w_I is the uncertainty in current.

After some manipulation, it is possible to write Equation (5.5) as follows:

$$w_P = [(I\, w_V)^2 + (V\, w_I)^2]^{1/2}, \tag{5.6}$$

where values of current I and voltage V are obtained from experimental values.

The power source Figure 5.5, used during tests does not present the necessary precision, however, the voltage is read by Agilent 34970A (Figure 5.6). For typical values from experiment, $V = 40.62\ V$ and $I = 1.84\ A$ we have $w_V = 0.004\ V$ and $w_I = 0.000184\ A$. Substituting the values on Equation (5.6):

$$w_P = [1.84^2 \cdot 0.004^2 + 40.62^2 \cdot 0.000184^2]^{1/2} = 0.01048\ W. \tag{5.7}$$

The total uncertainty in experimental data is given by:

$$w_{\Delta T,total} = \left[\left(\frac{\partial \Delta T}{\partial T}(w_{\Delta T} + w_{DAS})\right)^2 + (2w_{dT})^2 + \left(\frac{\partial \Delta T}{\partial P_n} w_P\right)^2\right]^{1/2}, \tag{5.8}$$

which yields, when numerical values are substituted:

$$w_{\Delta T,total} = \sqrt{1 \cdot (1.0 + 0.03)^2 + (2 \cdot 0.01)^2 + (0.49 \cdot 0.01048)^2} = 1.04\ ℃ \tag{5.9}$$

6 RESULTS AND DISCUSSION

In this chapter will be presented the results obtained experimentally and the comparison of experimental data and numerical model results. At the end of this chapter is presented the temperature change rate of for all experimental tests with a comparison with a temperature change rate obtained by linear regression of the experimental data.

6.1 Experimental and numerical results comparison

Experimental results were obtained with three different heat loads applied to the heat pipe throuth the heating block. The first case was run with heating power of $75\,W$ applied to the heaters ($37.5\,W$ each heater), with cooling provided by a combination of forced and natural convection. A second case took place with the same cooling configuration but with $25\,W$ applied to the heaters ($12.5\,W$ each heater). A third case was run with $25\,W$ applied to the heaters, and being cooled with natural convection only. Figure 6.1 shows a representation of the three different heat loads for these three cases in each pipe.

Figure 6.1 – Representation of Heat Load Locations for Experimental Setup.

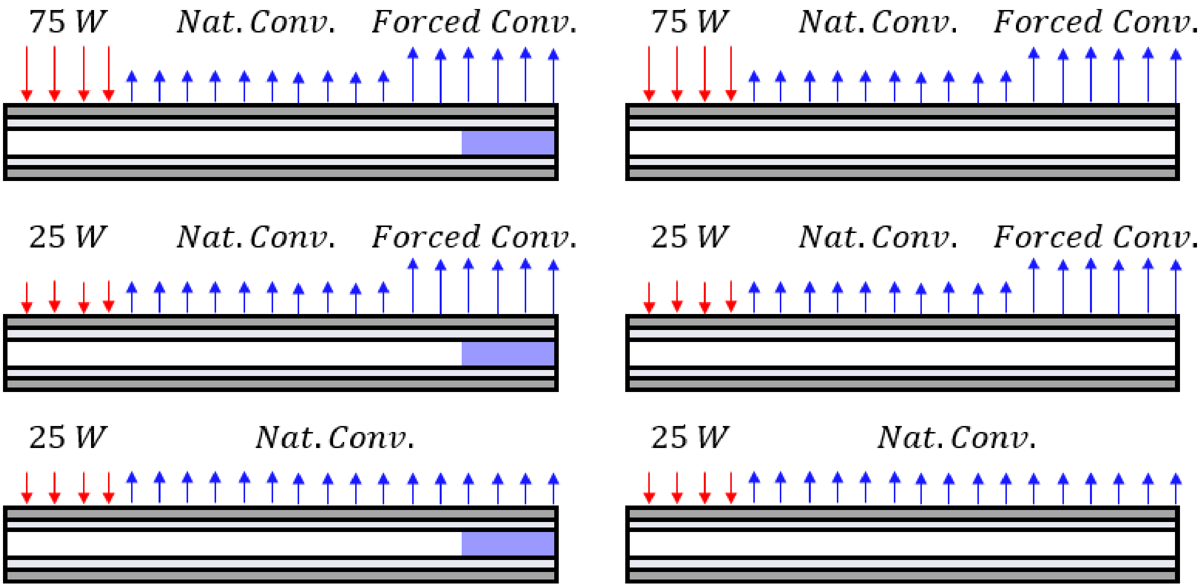

Source: The author.

For each heat pipe, tests were conducted during two different running periods, a long period test with heaters turned on for 2 hours and more 2 hours with heaters off, and a short period test with heaters turned on for 10 minutes with more 50 minutes of measurements with heaters turned off.

Each test was performed for both heat pipes, with and without noncondensable gas, totalizing 12 different experiments. All combinations of experiments can be seen in Table 6.1.

Table 6.1 – Performed Combinations of Experimental Test Setups.

Power Input (W)	NCG Present	Cooling Method	Running Period
75	No	$NC + FC$	$Long$
75	No	$NC + FC$	$Short$
75	Yes	$NC + FC$	$Long$
75	Yes	$NC + FC$	$Short$
25	No	$NC + FC$	$Long$
25	No	$NC + FC$	$Short$
25	Yes	$NC + FC$	$Long$
25	Yes	$NC + FC$	$Short$
25	No	NC	$Long$
25	No	NC	$Short$
25	Yes	NC	$Long$
25	Yes	NC	$Short$

Source: The author.

6.1.1 Long run test without NCG, cooled by natural and forced convection, with 75 W applied to the heater.

The test presented is a long run test, with a heat pipe without noncondensable gas, cooled by natural and forced convection combined and heat load of $75\ W$ applied to the heaters. A graphical representation of this test is shown in Figure 6.2.

Figure 6.2 – Representation of Experimental Setup With Heat Load of 75 W Cooled by Natural and Forced Convection Without Noncondensable Gas.

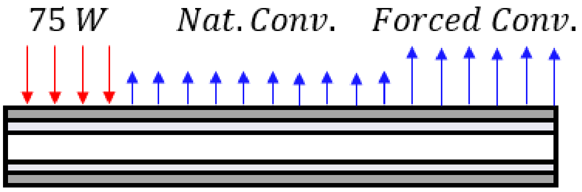

Source: The author.

Figure 6.3 (left) shows de time dependent temperatures of selected thermocouples and a comparison with the numerical results. Figure 6.3 (right) shows the temperature distribution along axis for selected times, until $2000\ s$, when the steady-state was practically achieved. The deviation from numerical results to experimental data do not exceeds 1.5 ℃.

Figure 6.3 – Experimental and Numerical Time Depentent Wall Temperatures and Temperature Distribution Along Axis for Selected Times.

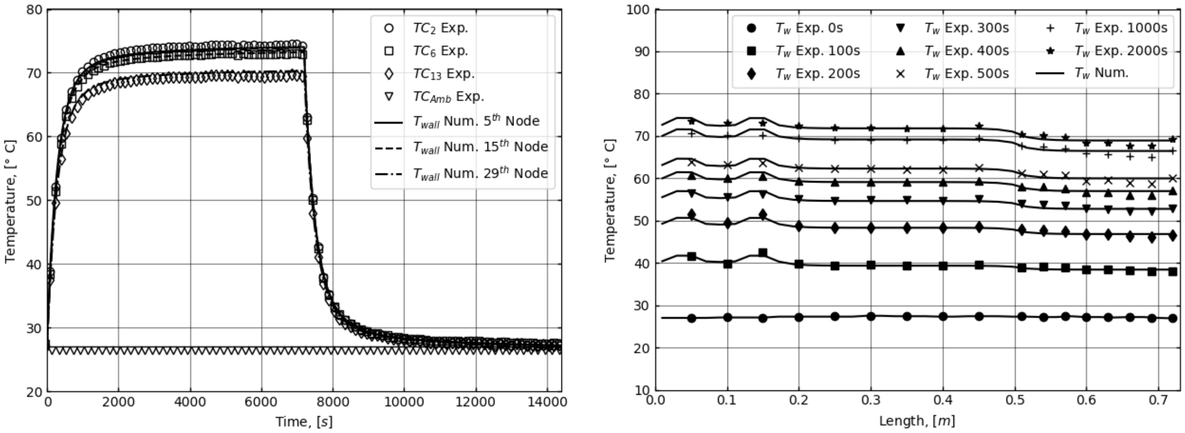

Source: The author.

Figure 6.4 shows the numerical results of density distribution of vapor along the axis for selected times. There are almost no gradient in density due to constant vapor temperature along the pipe’s length due to low velocity and low pressure drop along the vapor flow path.

Figure 6.4 – Vapor Distribution Along Axis for Selected Times.

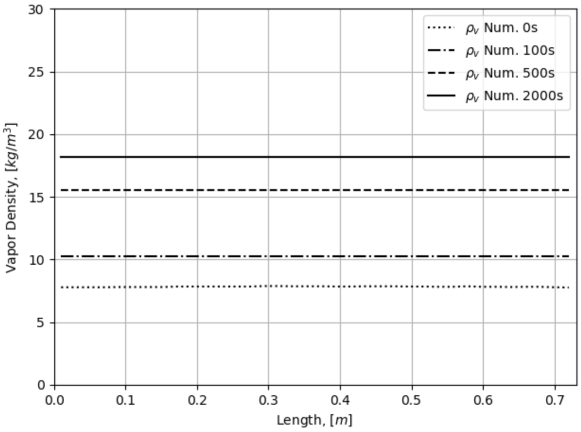

Source: The author.

Figure 6.5 shows the numerical results of axial velocity distribution and the evaporation/condensation mass flux distribution along the pipe for selected times. It is possible to see the rise in velocity at evaporator’s positions, and the fall in velocity along the condenser, with a higher decrease in velocity at the point with forced convection. In the case of evaporation/condensation mass flux, two evaporators position become very prominent as well as the forced convection region, which is easily identifiable with higher condensation rates.

Figure 6.5 – Axial Velocity and Evaporation/Condensation Mass Rate Along Axis for Selected Times.

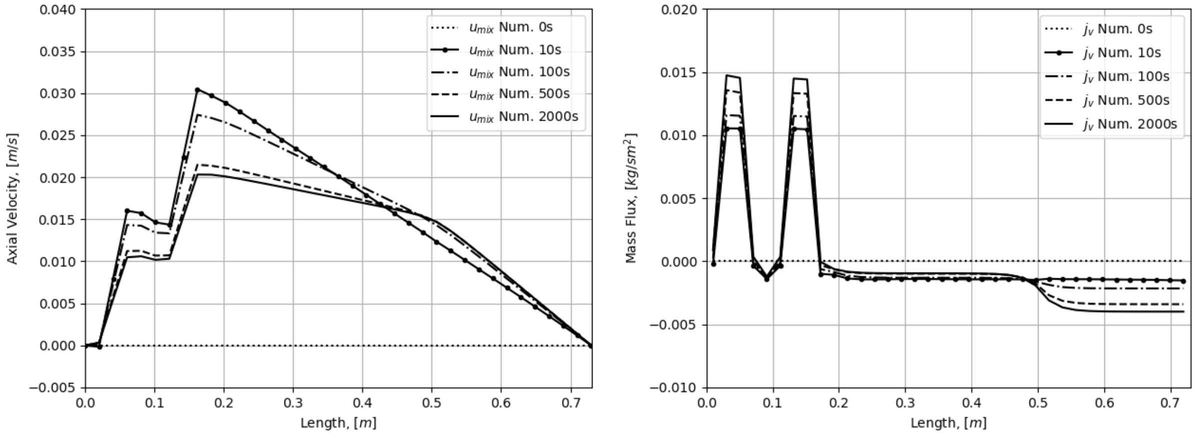

Source: The author.

Table 6.2 shows the values of heat transfer coefficients and relative locations where the coefficients were applied in numerical model for all simulations with heat load of $75\ W$ and cooled by natural and forced convection combined.

Table 6.2 – Values of heat transfer coefficients used in numerical models with 75W cooled by natural and forced convection.

Parameter $[W/mK]$	Evaporator Zone	Natural Convection Zone	Forced Convection Zone
h_f	$-$	$-$	50
$h_{wick,w}$	110000	110000	110000
$h_{evap/cond}$	12350	1425	1225
$h_{h,b}$	500	$-$	$-$
$h_{h,w}$	1000	$-$	$-$

Source: The author.

6.1.2 Short run test without NCG, cooled by natural and forced convection, with 75 W applied to the heater.

The following results presented is from a short run test, with a pipe without noncondensable gas, cooled by natural convection and forced convection combined and a heat load of $75\ W$ applied to the heaters.

Figure 6.6 (left) shows the short run time dependent temperatures of selected thermocouples and a comparison with the numerical results. Figure 6.6 (right) shows the temperature distribution along axis for selected times. The deviation the numerical results from experimental data does not exceed 1.5 ℃.

Figure 6.6 – Experimental and Numerical Time Depentent Wall Temperatures and Temperature Distribution Along Axis for Selected Times.

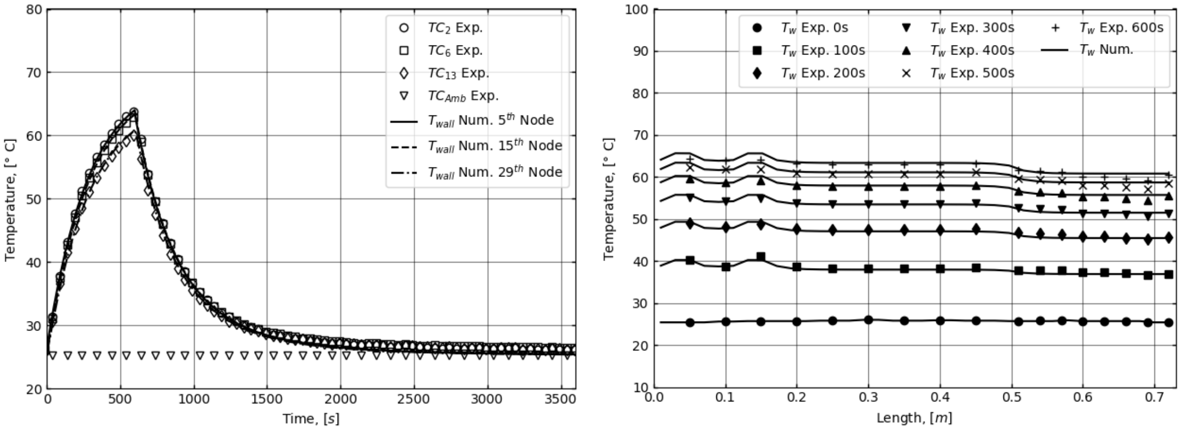

Source: The author.

Figure 6.7 – Experimental and Numerical Outer Wall Distribution Along Axis for Selected Times.

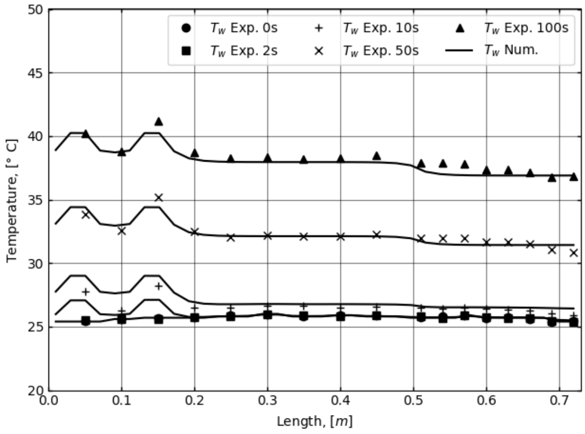

Source: The author.

Figure 6.7 shows the numerical results of temperature distribution along the axis for startup on the interval of 0 to $100\ s$. It is possible to see a rapid rise in temperatre in the first few minutes of heat pipe operation.

Figure 6.8 shows the numerical results of axial velocity distribution and the evaporation/condensation mass flux distribution along the pipe for the first $100\ s$ of simulation. It is possible to see the overshoot of temperature in velocity with values at $100\ s$ lower than the values of velocity at $10\ s$ of operation.

Figure 6.8 – Axial Velocity and Evaporation/Condensation Mass Rate Along Axis for Selected Times.

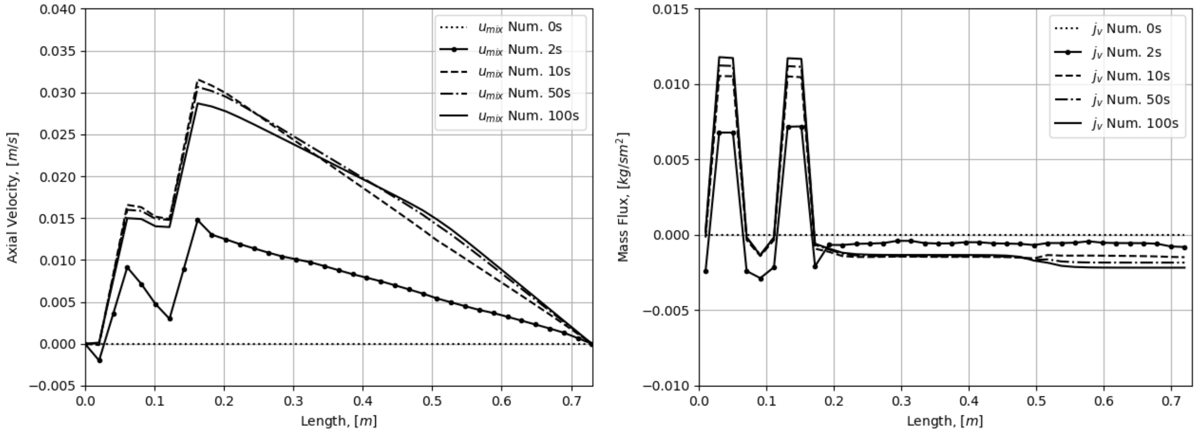

Source: The author.

6.1.3 Long Run Test with NCG, cooled by Natural and Forced Convection, with 75 W Applied to the Heater.

The test presented is a long run test, until the steady-state was reached, with a pipe charged with noncondensable gas, cooled by a combination of natural and forced convection with a heat load of $75\ W$ applied to the heaters. A representation of this setup with noncondensable gas is shown in Figure 6.9.

Figure 6.9 – Representation of Experimental Setup With Heat Load of 75 W Cooled by Natural and Forced Convection With Noncondensable Gas.

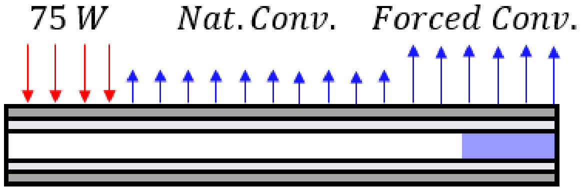

Source: The author.

The long period time dependent temperatures of selected thermocouples are shown in Figure 6.10, as well as the numerical results. Figure 6.10 (left) shows the transient temperatures of selected thermocouples, while Figure 6.10 (right) shows the temperature distribution along axis for selected times. As expected, the heat pipe with noncondensable gas presents a higher temperature gradient between evaporation and condensation zones in comparison with pipe without noncondensable gas, and this pattern repeats for all tests. The maximum deviation from numerical results to experimental data was about $2.5\ ^{\circ}\mathrm{C}$ at $100\ s$ from startup.

It was detected some temperature oscillations in the condenser of the heat pipe containing noncondensable gas when temperatures reached steady-state (visible on experimental results of thermocouple 13), which is in accordance to previous results given by Edom and Vlassov (2001).

Figure 6.10 – Experimental and Numerical Time Dependent Wall Temperatures and Temperature Distribution Along Axis for Selected Times.

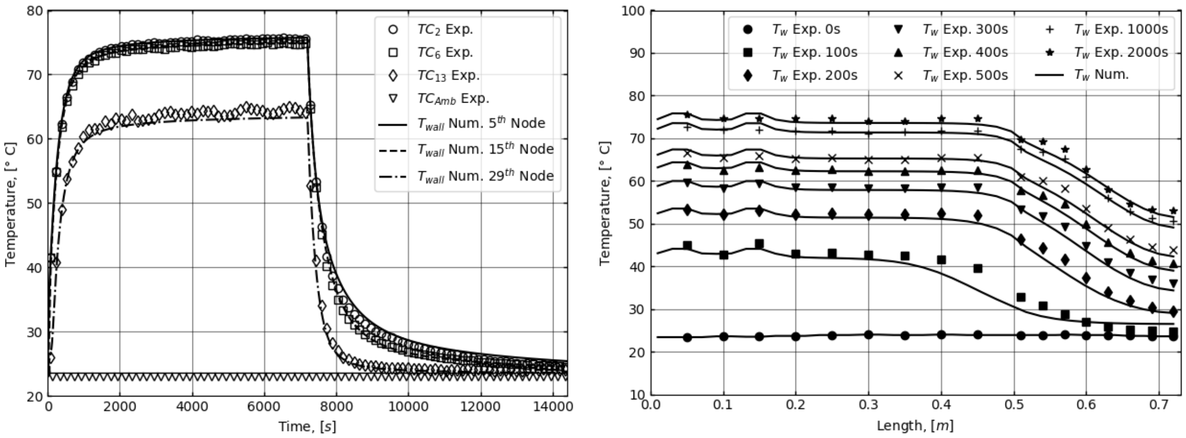

Source: The author.

Figure 6.11 shows the numerical results of density distribution of vapor and noncondensable gas along the axis for selected times, within 0 to $2000\,s$ time interval. In this case, a gradient in vapor density appear due to distortions caused by the presence of noncondensable gas.

Figure 6.11 – Vapor and Noncondensable Gas Distribution Along Axis for Selected Times.

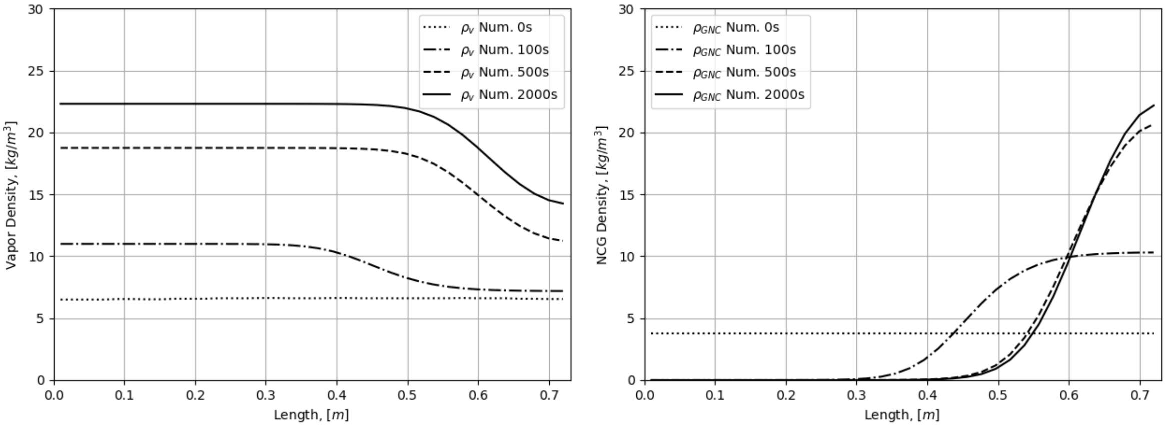

Source: The author.

Figure 6.12 (left) shows the numerical results of axial velocity and the evaporation/condensation mass flux distribution along the heat pipe with noncondensable gas. Here is also possible to see the rise in velocity at two evaporators positions, and the fall in velocity along the condenser, with a higher rate in velocity at the forced convection zone. In this case, the presence of noncondensable gas modifies the profile of velocity at the end of condenser. There is not enough quantity of noncondensable gas to block completely the condenser, so velocity decrease at higher rates when compared with the pipe without gas, but does not reach zero before the condenser end.

Figure 6.12 – Axial Velocity and Evaporation/Condensation Mass Rate Along Axis for Selected Times.

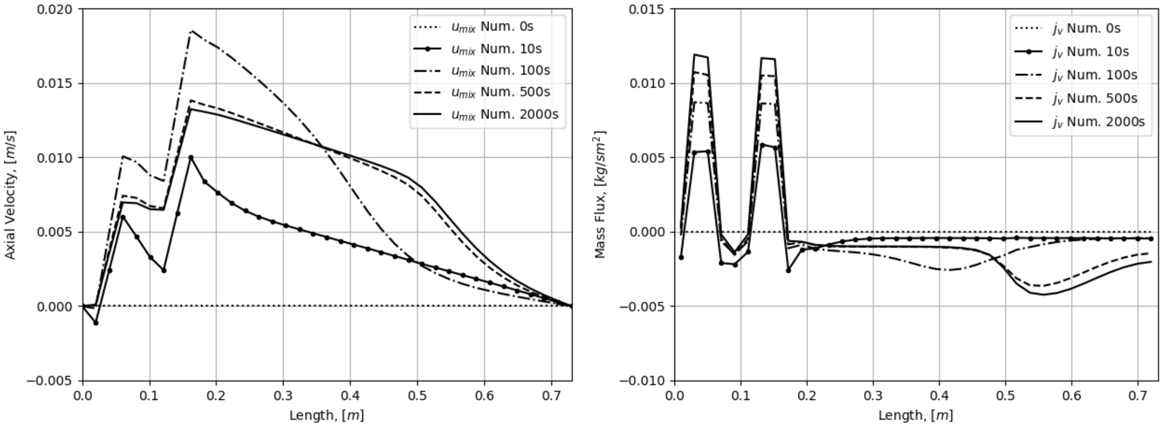

Source: The author.

In Figure 6.12 (right), it is important to observe that there is no points in condenser where temperature is in equilibrium with ambient, so the condensation process decreases with the presence of noncondensable gas but does not ceases entirely.

The model was able to simulate such an interesting phenomenon as a vapor velocity overshoot, not detectable by the experimental results with temperature measurement. One can observe from the graph, that the vapor velocity experiences a noteworthy pick at $100\,s$ on percussion of 10 to 100 to $500\,s$. This pick naturally occurs due to initial noncondensable gas redistribution. On the first moments after startup, vapor goes to the condensation zone and condenses over entire area of the condenser so the vapor velocity is high. Soon after, noncondensable gas starts to progressively block the condenser end vapor channel, effective condensation area decreases and the vapor velocity begin also to decrease.

6.1.4 Short run test with NCG, cooled by natural and forced convection, with 75 W applied to the heater.

The next results are from a short run startup test, with a pipe with the presence of noncondensable gas, cooled by natural and forced convection combined and a heat load of $75\,W$ applied to the heaters.

Figure 6.13(left) shows de time dependent temperatures of selected thermocouples and a comparison with the numerical results. Figure 6.6 (right) shows the temperature distribution along axis for selected times within the period from 0 to $600\ s$ from startup. In this short period test, temperature oscillations in the condenser of the heat pipe containing noncondensable gas are almost undetectable.

Figure 6.13 – Experimental and Numerical Time Depentent Wall Temperatures and Temperature Distribution Along Axis for Selected Times.

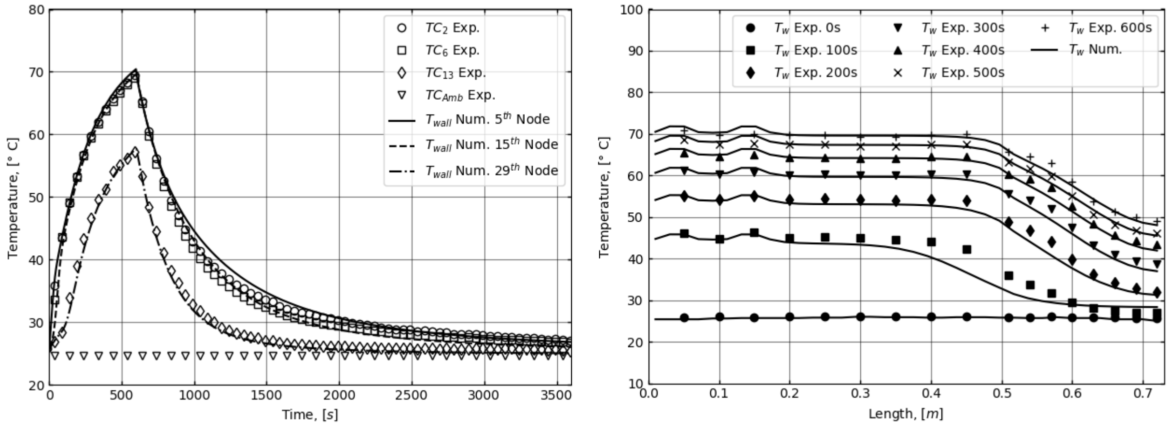

Source: The author.

Figure 6.14 shows the numerical results of density distribution of vapor along the axis for selected times. It shows that at around $200\ s$, the diffuse front is almost totally formed and front position remains without much change from this point on.

Figure 6.14 – Vapor and Noncondensable Gas Distribution Along Axis for Selected Times.

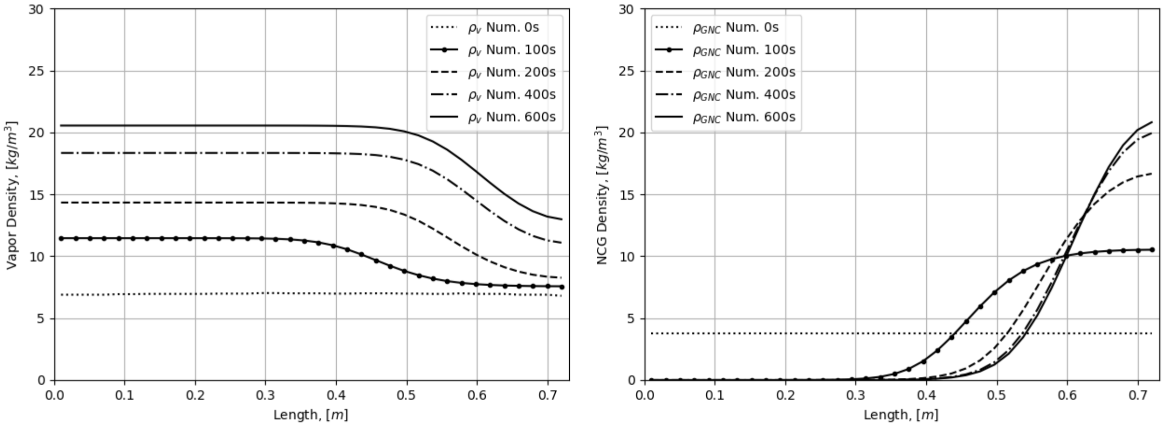

Source: The author.

Figure 6.15 shows the numerical results of axial velocity distribution and the evaporation/condensation mass flux distribution along the pipe for selected times.

Figure 6.15 (left) one can conclude that the velocity overshoot phenomenon, detected and described for the long period simulation, lasted about $400\ s$.

Figure 6.15 – Axial Velocity and Evaporation/Condensation Mass Rate Along Axis for Selected Times.

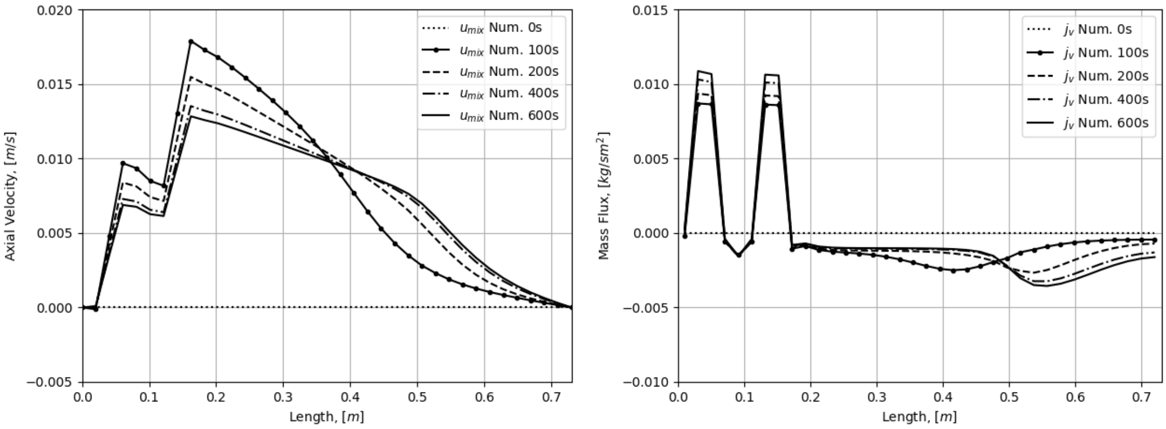

Source: The author.

6.1.5 Long run test without NCG, cooled by natural and forced convection, with 25 W applied to the heater.

The next test presented is a long run transient test, with a heat pipe without noncondensable gas, cooled by a combination of natural and forced convection and, a heat load of $25\ W$. A representation of this text with $25\ W$ is shown in Figure 6.16.

Figure 6.16 – Representation of Experimental Setup With Heat Load of 25 W Cooled by Natural and Forced Convection Without Noncondensable Gas.

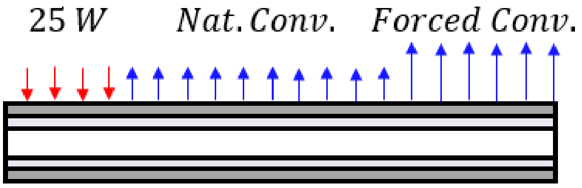

Source: The author.

Figure 6.17 shows the experimental transient temperatures and a comparison with the numerical results. Figure 6.17 (right) shows the temperature distribution along axis for selected times. With less power applied to the heaters, the temperatures are lower when compared to the case of $75\ W$, and maximum deviation from the experimental results gets improvement from 1.5 °C to 0.8 °C.

Figure 6.17 – Experimental and Numerical Time Depentent Wall Temperatures and Temperature Distribution Along Axis for Selected Times.

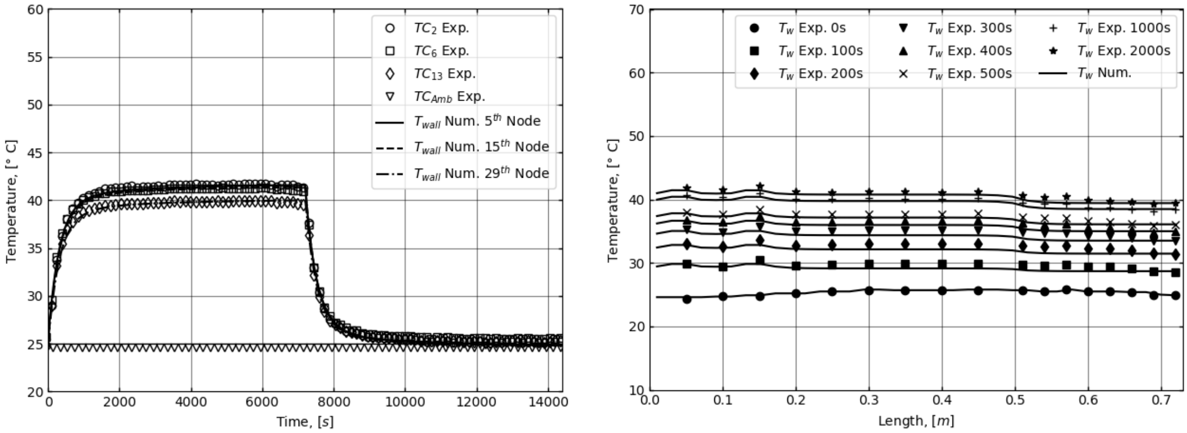

Source: The author.

Numerical results confirm the vapor density distribution along the axis is linear and does not reveal any signal of visible gradients, similarly to the case of $75\,W$ load. Figure 6.18 shows the numerical results of axial velocity distribution and the evaporation/condensation mass flux distribution along the pipe for selected times.

Figure 6.18 – Axial Velocity and Evaporation/Condensation Mass Rate Along Axis for Selected Times.

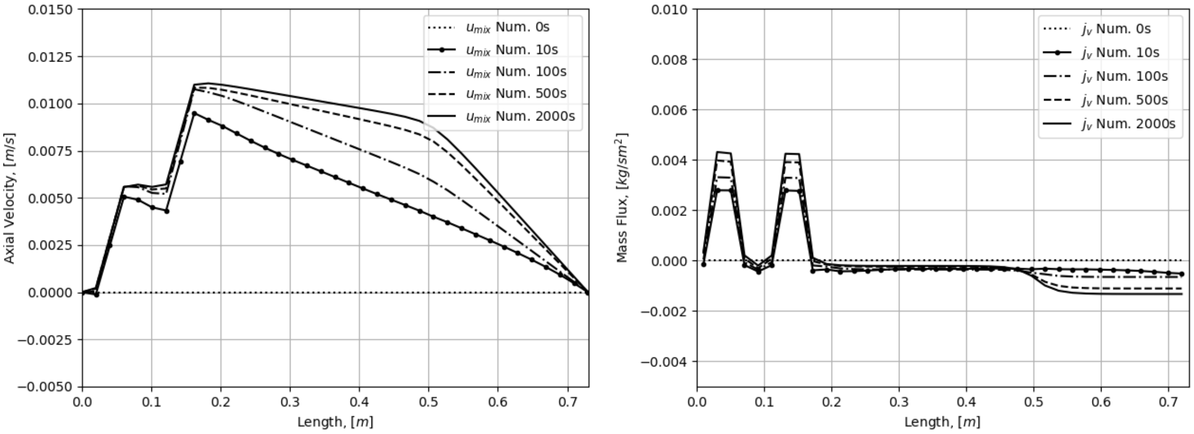

Source: The author.

Table 6.3 shows the values of heat transfer coefficients and relative locations where the coefficients were applied in numerical model for all simulations with heat load of $25\,W$ and cooled by natural and forced convection combined.

Table 6.3 – Values of heat transfer coefficients used in numerical models with 25W cooled by natural and forced convection.

Parameter $[W/mK]$	Evaporator Zone	Natural Convection Zone	Forced Convection Zone
h_f	–	–	50
$h_{wick,w}$	110000	110000	110000
$h_{evap/cond}$	16400	1600	1200
$h_{h,b}$	500	–	–
$h_{h,w}$	900	–	–

Source: The author.

6.1.6 Short run test without NCG, cooled by natural and forced convection, with 25 W applied to the heater.

The following results presented is from a short run test, with a pipe without noncondensable gas, cooled by natural and forced convection combined and a heat load of $25\ W$ applied to the heaters.

Figure 6.19 (left) shows de time dependent temperatures of selected thermocouples and a comparison with the numerical results. Figure 6.19 (right) also shows the temperature distribution along axis for selected times for a shorter period of $600\ s$.

Figure 6.19 – Experimental and Numerical Time Depentent Wall Temperatures and Temperature Distribution Along Axis for Selected Times.

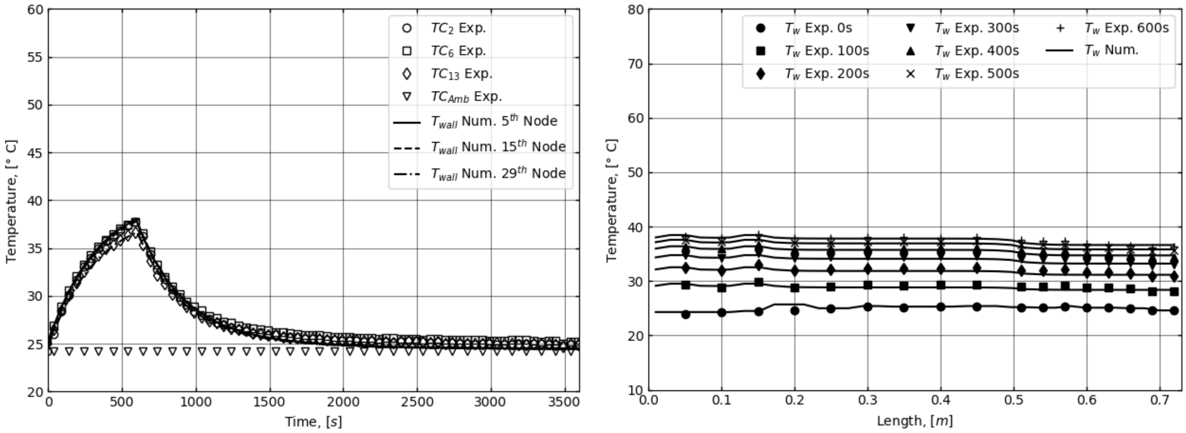

Source: The author.

Figure 6.20 demonstrates the temperature behavior at startup short period of 100 s.

Figure 6.20 – Experimental and Numerical Temperature Distribution Along Axis for Selected Times.

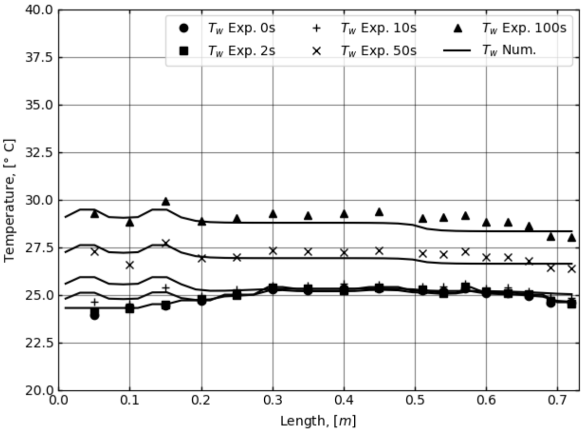

Source: The author.

Figure 6.21 shows the numerical results of axial velocity distribution and the evaporation/condensation mass flux distribution along the pipe for selected times.

Figure 6.21 – Axial Velocity and Evaporation/Condensation Mass Rate Along Axis for Selected Times.

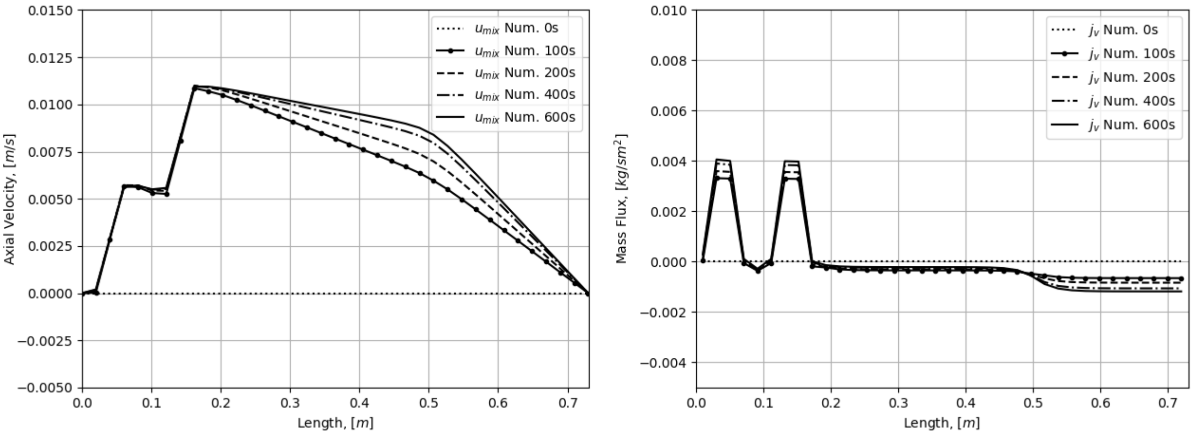

Source: The author.

6.1.7 Long run test with NCG, cooled by natural and forced convection, with 25 W applied to the heater.

The next test presented is a transient long run test, with a heat pipe with noncondensable gas, cooled by forced and natural convection with a heat load of $25\ W$. A graphic representation of this setup is shown in Figure 6.22.

Figure 6.22 – Representation of Experimental Setup With Heat Load of 25 W Cooled by Natural and Forced Convection With Noncondensable Gas.

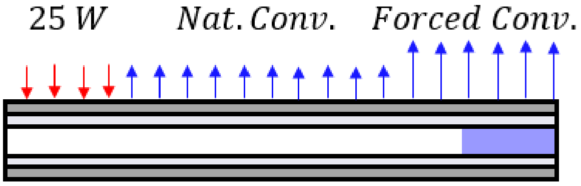

Source: The author.

The long period time dependent temperatures of selected thermocouples are shown in Figure 6.23 (left), with the numerical results. Figure 6.23 (right) shows the transient temperatures of selected thermocouples, and the temperature distribution along axis for selected times.

Figure 6.23 – Experimental and Numerical Time Depentent Wall Temperatures and Temperature Distribution Along Axis for Selected Times.

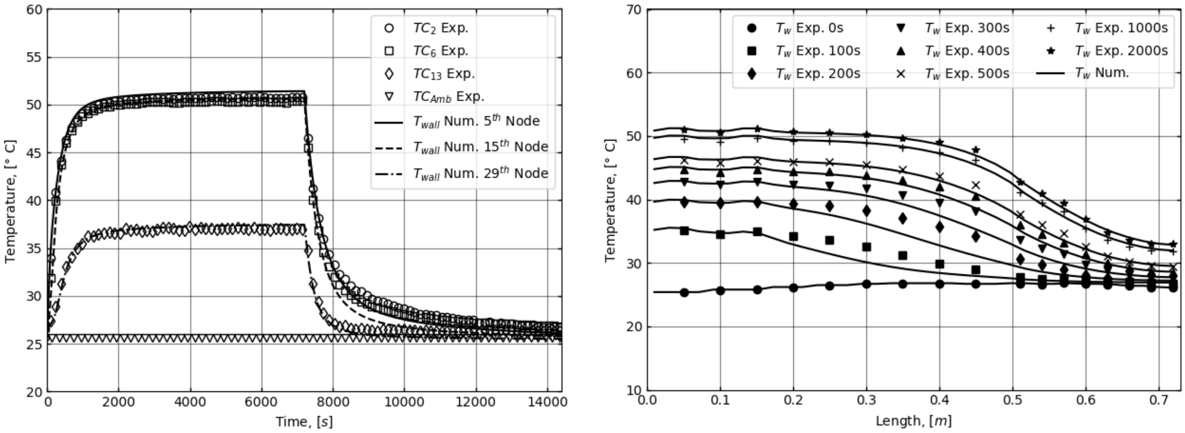

Source: The author.

Figure 6.24 shows the numerical results of density distribution of vapor and noncondensable gas along the heat pipe axis for selected times. It is seen from graphs, a gradient in vapor density appears due to distortions caused by the presence of noncondensable gas.

Figure 6.24 – Vapor and Noncondensable Gas Distribution Along Axis for Selected Times.

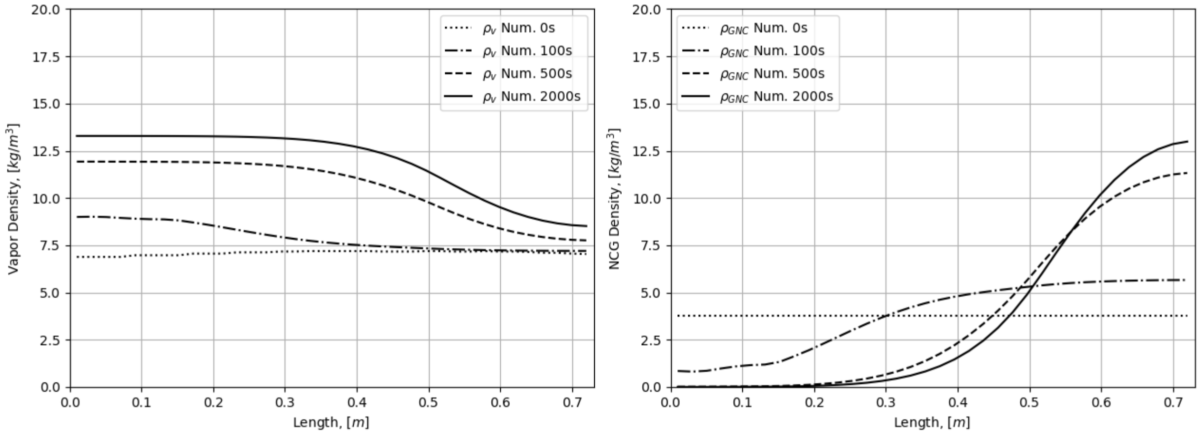

Source: The author.

Figure 6.25 shows the numerical results of axial velocity distribution and the evaporation/condensation mass flux distribution along the pipe with noncondensable gas for selected times.

From these results, we can conclude that the formation of the diffusion front vapor-gas barrier in the heat pipe vapor channel takes as long as about $1000\,s$ from startup.

Figure 6.25 – Axial Velocity and Evaporation/Condensation Mass Rate Along Axis for Selected Times.

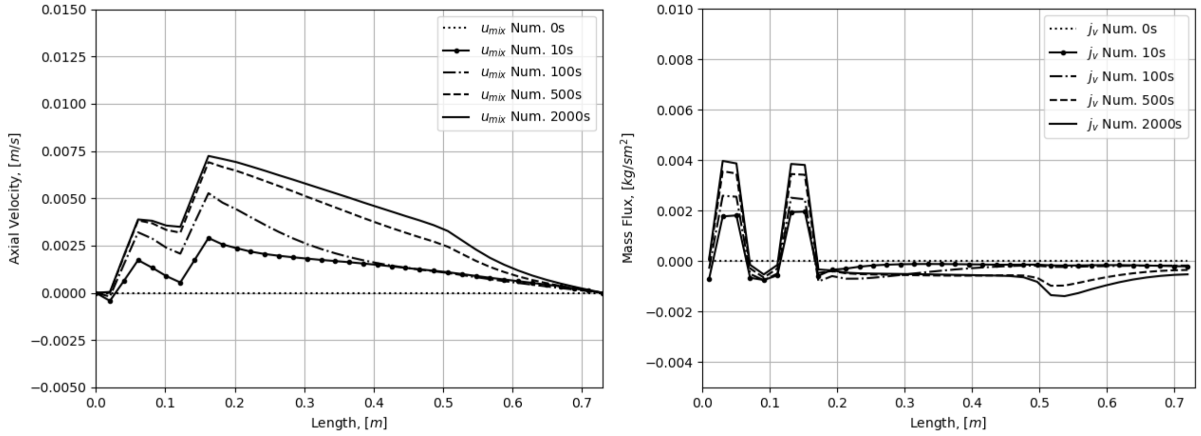

Source: The author.

6.1.8 Short run test with NCG, cooled by natural and forced convection, with 25 W applied to the heater

The following results presented is from a short run test, with a pipe with the presence of noncondensable gas, cooled by natural and forced convection, and a heat load of $25\ W$ applied to the heaters.

Figure 6.26 shows de time dependent temperatures of selected thermocouples and a comparison with the numerical results. Figure 6.26 also shows the temperature distribution along axis for selected times.

Figure 6.26 – Experimental and Numerical Time Depentent Wall Temperatures and Temperature Distribution Along Axis for Selected Times.

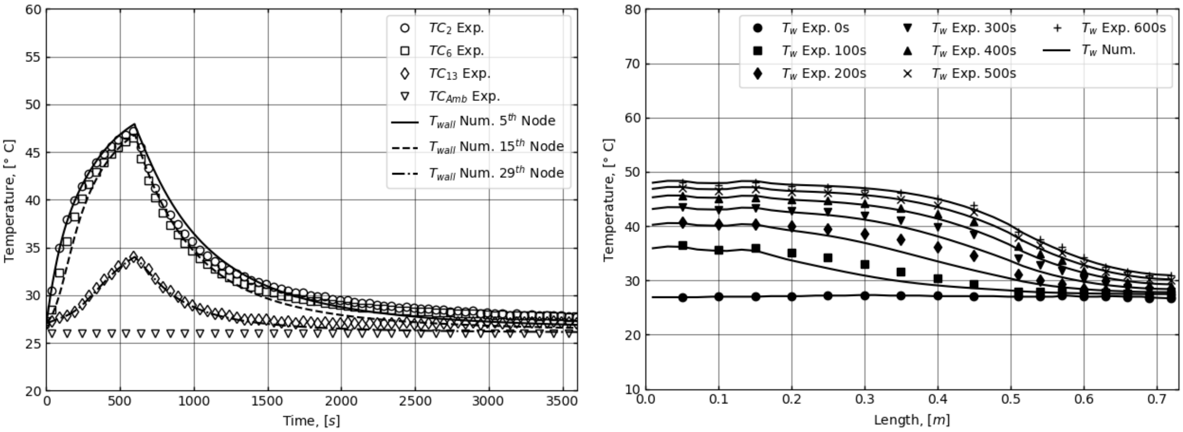

Source: The author.

Figure 6.27 – Vapor and Noncondensable Gas Distribution Along Axis for Selected Times.

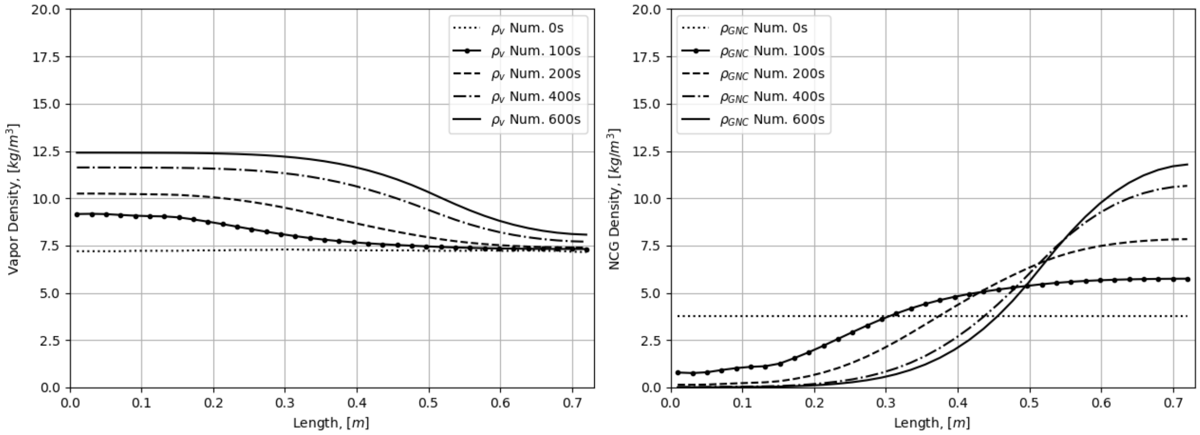

Source: The author.

Figure 6.27 shows the numerical results of density distribution of vapor along the axis for selected times. It is possible to observe that at around $200\ s$, the diffuse front is almost totally formed and front position remains without much change from this point on.

Figure 6.28 shows the numerical results of axial velocity distribution and the evaporation/condensation mass flux distribution along the pipe for selected times.

Figure 6.28 – Axial Velocity and Evaporation/Condensation Mass Rate Along Axis for Selected Times.

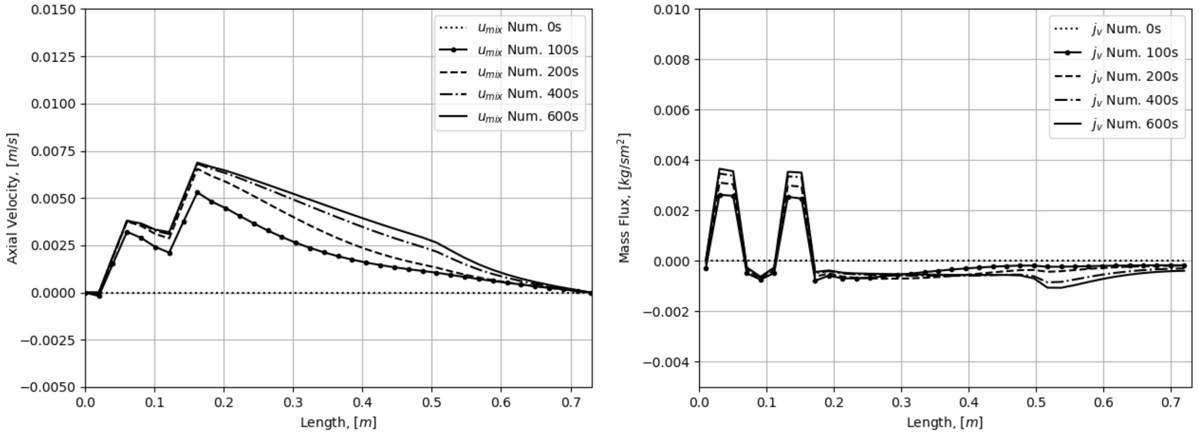

Source: The author.

It very interesting to observe, the velocity overshoot, detected for noncondensable gas charged heat pipe at 100 s with high heat load of $75\ W$, does not appear for the same heat with noncondensable gas but under low heat load of $25\ W$. This is a new finding obtained by the simulation: the velocity overshoot phenomenon occurs only in heat pipe with under heat loads applied on startup.

6.1.9 Long run test without NCG, cooled by natural convection only, with 25 W applied to the heater.

In this section, it is presented is a transient long run test, with a heat pipe without noncondensable gas, cooled by natural convection only with a heat load of $25\ W$ is applied to the heaters. A graphic representation of the experimental setup is shown in Figure 6.29.

Figure 6.29 – Representation of Experimental Setup With Heat Load of 25 W Cooled by Natural Convection Without Noncondensable Gas.

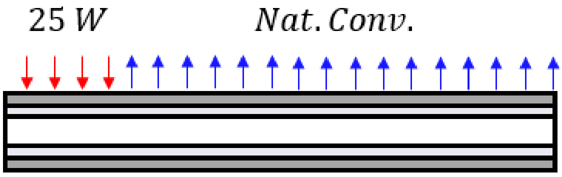

Source: The author.

Figure 6.30 (left) shows de transient temperatures of selected thermocouples and a comparison with the numerical results. Figure 6.30 (right) shows the temperature distribution along axis for selected times. Due to lower capability to remove heat by natural convection, the temperature is almost isothermal through the pipe, with a small temperature elevation at evaporator location. By the same reason, the transient period until steady-state achievement takes more time, about $3000\,s$, in comparison with $2000\,s$ for forced convection cooling.

Figure 6.30 – Experimental and Numerical Time Depentent Wall Temperatures and Temperature Distribution Along Axis for Selected Times.

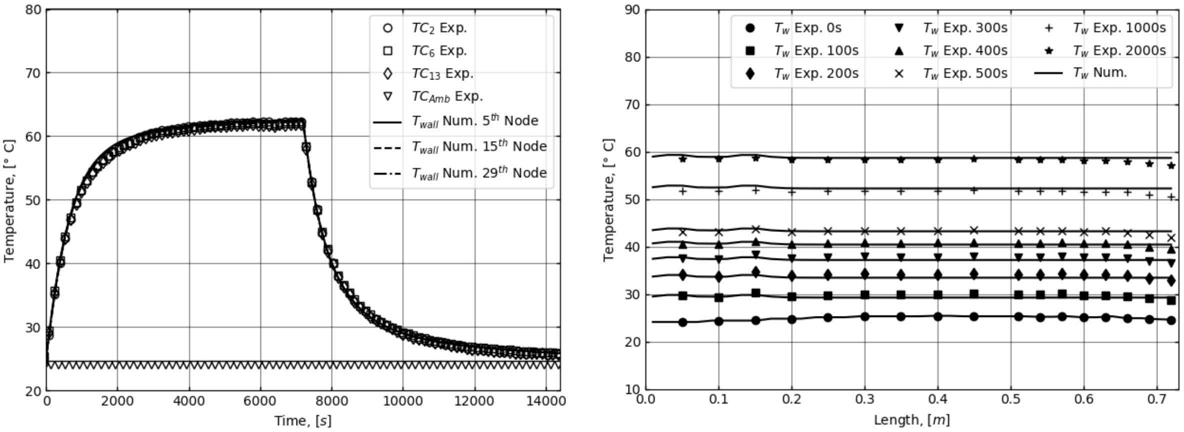

Source: The author.

Figure 6.31 shows the numerical results of density distribution of vapor along the axis for selected times.

Figure 6.31 – Vapor Distribution Along Axis for Selected Times.

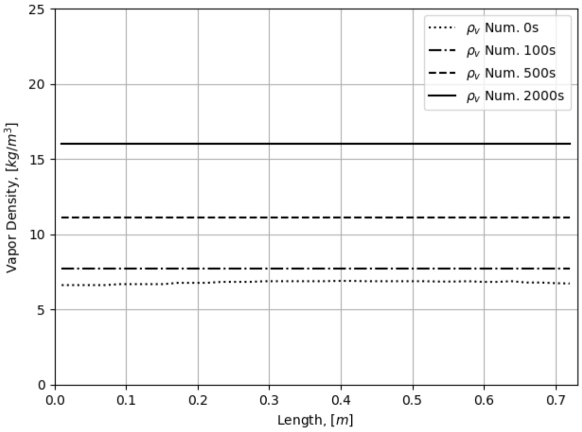

Source: The author.

Figure 6.32 shows the numerical results of axial velocity distribution and the evaporation/condensation mass flux distribution along the pipe for selected times. It is possible to see the rise in velocity at two evaporators positions. The fall in velocity along the condenser is almost constant, indicating a lower cooling rate at condenser, as expected for the natural convection.

Figure 6.32 – Axial Velocity and Evaporation/Condensation Mass Rate Along Axis for Selected Times.

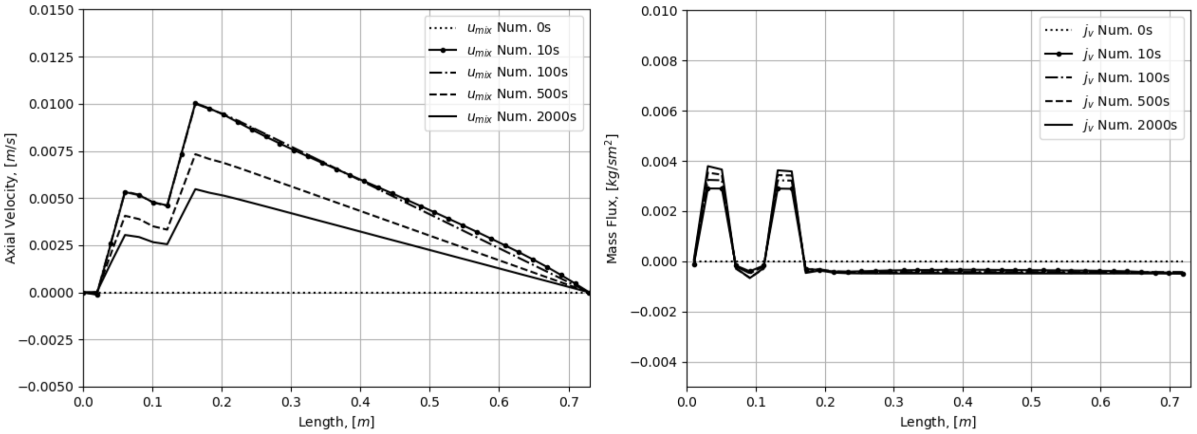

Source: The author.

Table 6.4 shows the values of heat transfer coefficients and relative locations where the coefficients were applied in numerical model for all simulations with heat load of $25\ W$ and cooled by natural convection only.

Table 6.4 – Values of heat transfer coefficients used in numerical models with 25W cooled by natural convection.

Parameter $[W/mK]$	Evaporator Zone	Natural Convection Zone
$h_{wick,w}$	110000	110000
$h_{evap/cond}$	16400	2500
$h_{h,b}$	500	$-$
$h_{h,w}$	900	$-$

Source: The author.

6.1.10 Short run test without NCG, cooled by natural convection, with 25 W applied to the heater

The following results presented is from a short run test, with a pipe without noncondensable gas, cooled by natural convection and heat load of $25\ W$ applied to the heaters.

Figure 6.33 shows de transient temperatures of selected thermocouples and a comparison with the numerical results. It also shows the temperature distribution along axis for selected times.

Figure 6.33 – Experimental and Numerical Time Depentent Wall Temperatures and Temperature Distribution Along Axis for Selected Times.

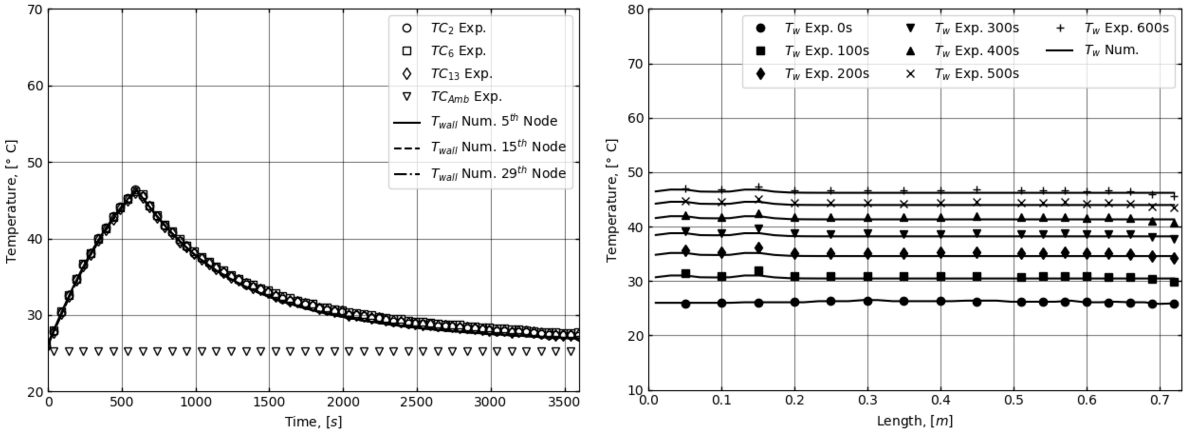

Source: The author.

Figure 6.34 shows the numerical results of density distribution of vapor along the axis for selected times.

Figure 6.34 – Vapor Distribution Along Axis for Selected Times.

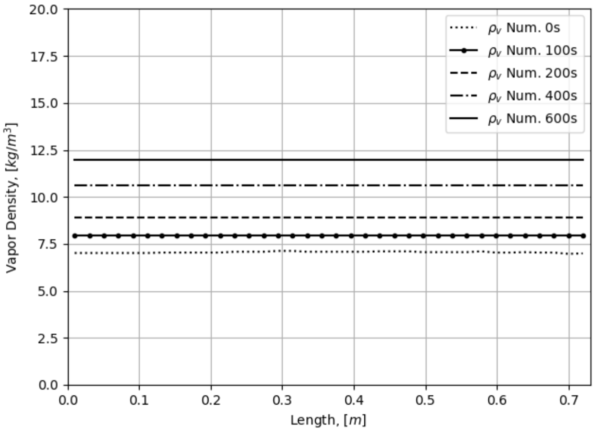

Source: The author.

Figure 6.35 shows the numerical results of axial velocity distribution and the evaporation/condensation mass flux distribution along the pipe for selected times.

Figure 6.35 – Axial Velocity and Evaporation/Condensation Mass Rate Along Axis for Selected Times.

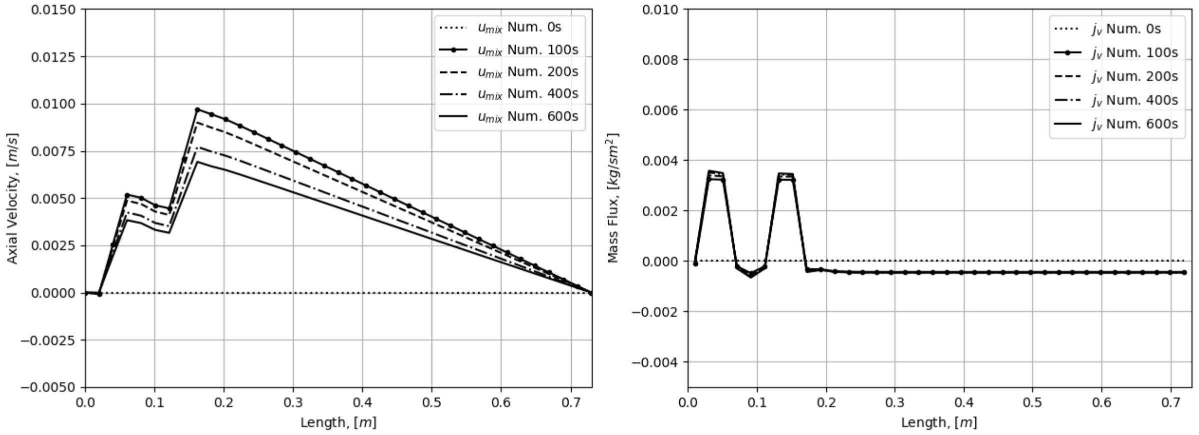

Source: The author.

6.1.11 Long run test with NCG, cooled by natural convection, with 25 W applied to the heater

This section presents is a long run transient test, with a heat pipe charged with noncondensable gas, cooled by natural convection only and a heat load of $25\,W$. A graphic representation of the setup is shown in Figure 6.36.

Figure 6.36 – Representation of Experimental Setup With Heat Load of 25 W Cooled by Natural Convection With Noncondensable Gas.

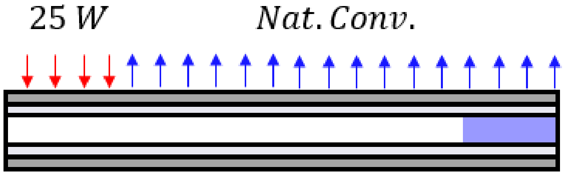

Source: The author.

The long period transient temperatures of selected thermocouples are shown in Figure 6.37 , as well as the numerical results. Figure 6.37 (left) shows the transient temperatures of selected thermocouples, while Figure 6.37 (right) shows the temperature distribution profile along heat pipe axis for selected times. As expected and contrary to the heat pipe without noncondensable gas, the heat pipe with noncondensable gas presented a higher temperature gradient between evaporation and condensation zones.

Figure 6.37 – Experimental Numerical Time Depentent Wall Temperatures and Temperature Distribution Along Axis for Selected Times.

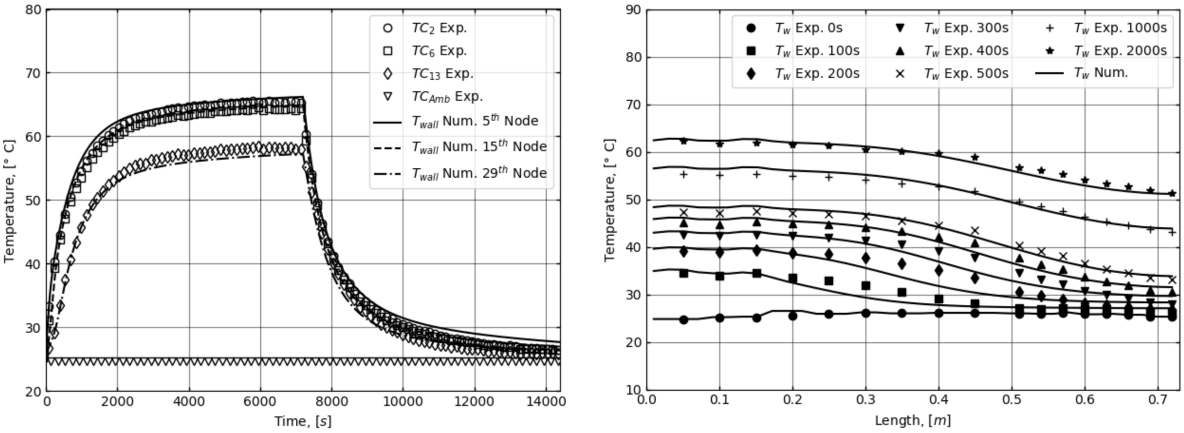

Source: The author.

Figure 6.38 shows the numerical results of density distribution of vapor and noncondensable gas along the axis for selected times. This figure presents the dynamic of the diffusion vapor-gas front developing on heat pipe startup

Figure 6.38 – Vapor and Noncondensable Gas Distribution Along Axis for Selected Times.

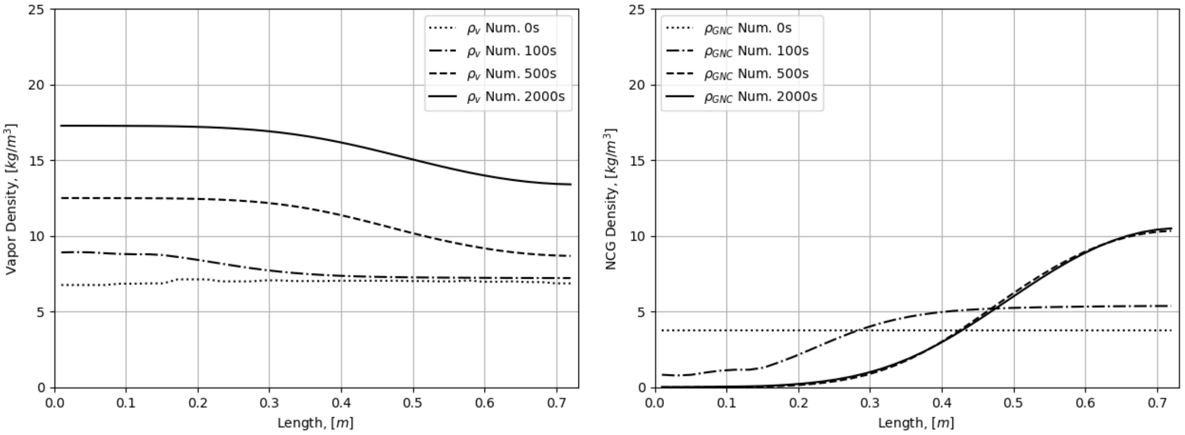

Source: The author.

Figure 6.39 shows the numerical results of axial velocity distribution and the evaporation/condensation mass flux distribution along the pipe with noncondensable gas for selected times.

Figure 6.39 – Axial Velocity and Evaporation/Condensation Mass Rate Along Axis for Selected Times.

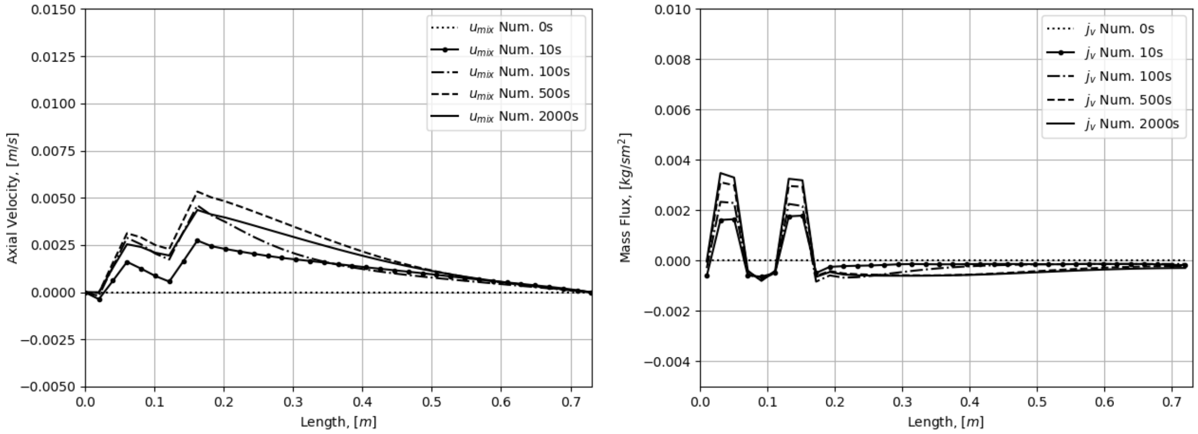

Source: The author.

Once again, it very interesting to observe, the velocity overshoot, detected for noncondensable gas charged heat pipe at $100\ s$ with high heat load of $75\ W$, and not detected under low heat load of $25\ W$, appears again (however very small) at this low heat load, but with weak cooling intensity provided by natural convection only. This is one more new finding obtained by the simulation, the velocity overshoot phenomenon may occur also in heat pipes under low heat loads however under natural convection weak cooling.

6.1.12 Short run test with NCG, cooled by natural convection, with 25 W applied to the heater

The last results presented is from a short run test, with a pipe with the presence of noncondensable gas, cooled by natural convection and a heat load of $25\ W$ applied to the heaters.

Figure 6.40 (left) shows de transient temperatures of selected thermocouples and a comparison with the numerical results. Figure 6.40 (right) also shows the temperature distribution along axis for selected times.

Figure 6.40 – Experimental and Numerical Time Depentent Wall Temperatures and Temperature Distribution Along Axis for Selected Times.

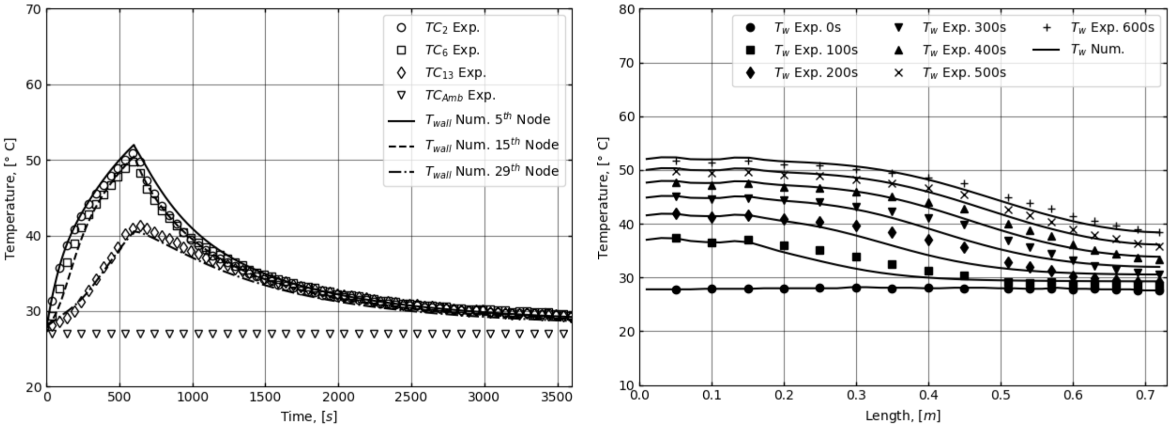

Source: The author.

Figure 6.41 shows the numerical results of density distribution of vapor along the axis for selected times.

Figure 6.41 – Vapor and Noncondensable Gas Distribution Along Axis for Selected Times.

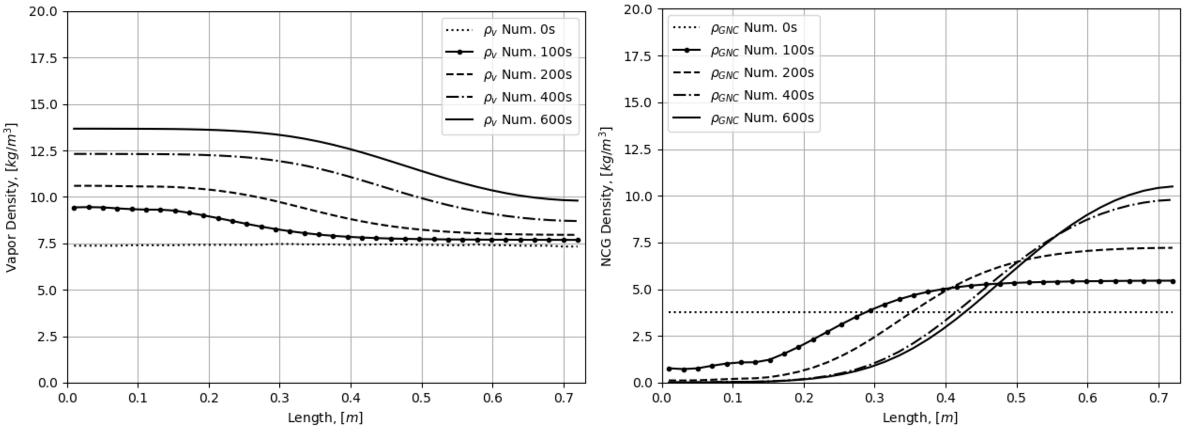

Source: The author.

Figure 6.42 shows the numerical results of axial velocity distribution and the evaporation/condensation mass flux distribution along the pipe for selected times.

Figure 6.42 – Axial Velocity and Evaporation/Condensation Mass Rate Along Axis for Selected Times.

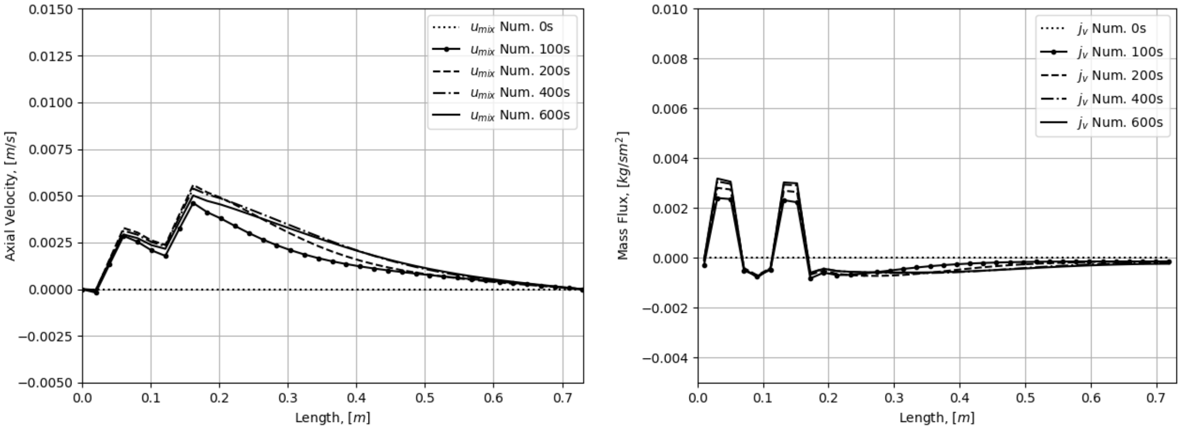

Source: The author.

As a partial conclusion of this chapter, we can reveal the main results obtained with the developed model:

– the prediction of dynamic of velocity distribution under any fast and slow transient processes, including startup and shutdown;

– the distribution of evaporator-condensation mass flux transient;

– modeling of vapor-gas diffusion front developing through time, evaluation of time of the front establishment;

– the velocity overshoot on startup of heat pipe in some cases is a new phenomenon detected;

– modeling of temperature delays on condenser temperatures on startup of heat pipe with noncondensable gas;

– precise simulation of transient temperature profiles along heat pipe length confirmed by experimental data.

7 CONCLUSIONS

A mathematical model capable to simulate different transient modes of a heat pipe with and without the presence of noncondensable gas was developed. An extensive program of model validation has proved that the one dimensional compressible mixture heat pipe model is capable to simulate many transient modes and unusual heat load applications to the heat pipes.

Experimental tests were conducted with two identical aluminum ammonia heat pipes, with and without noncondensable gas. This approach allowed to improve the model precision by separate adjusting of parameters which are common for both heat pipes. Different external conditions were tested and simulated including fast transients, like startup and shutdown, as well as long transient processes until steady-state condition were achieved.

A good agreement between numerical and experimental data was achieved for over entire transient period in various combination of heat loads and cooling methods. The model was capable to predict the noncondensable gas diffusion front formation dynamic in fast transient processes and position of vapor-gas barrier for steady-state.

Fast transient tests proved to be an efficient way to detect the presence of noncondensable gas inside pipe through the analysis of the temperature change rate instead of the temperature itself. The developed mathematical model and computer code can be used to define the limit of sensitivity of noncondensable gas amount detection of such fast transient verification tests on the heat pipes already embedded into honeycomb structural satellite panels with equipment mounted on.

7.1 Future work

Based on the present study, some work still can be done in order to improve the model developed, bring useful data to INPE and increase the understanding about the functioning of heat pipes. Future development involves:

- use the present one dimensional model to simulate and predict the behavior of the TUCA experiment - a heat pipe experiment to be launched with Amazonia 1 satellite in 2020;

- use the model to simulate different quantities of noncondensable gas inside the pipe to estimate minimum gas quantity necessary to be detectable through temperature measurements;
- input the model developed as a module inside the software SINDA/FLUINT Thermal Desktop, which will allow the software to simulate a heat pipe embedded in structural panels within the overall thermal mathematical model (TMM) of satellite;
- upgrade the model from one dimensional to two dimensional, which will allow the model to simulate a wider range of heat load applications;
- upgrade the model with a model of the liquid inside the wick, this can allow the model to simulate other failure modes present in heat pipes like the dry-out phenomena.

REFERENCES

ANDERSON, J. D. **Computational fluid dynamics:** the basics with applications. Singapore: McGraw-Hill, 1995. 574 p.

ANDERSON, W. T. Hydrogen evolution in nickel-water heat pipes. In: AIAA THERMOPHYSICS CONFERENCE, 8., 1973. **Proceedings…** 1973.

ANDERSON, W. T.; EDWARDS, D. K.; ENINGER, J. E.; MARCUS, B. D. **Variable conductance heat pipe technology**. California: [s.n.], 1974. 87 p. Final Research Report Contract Number NAS 2-5503.

BERTOLDO JUNIOR, J.; VLASSOV, V.; GENARO G.; SANTOS, N.; CANDIDO, P. A. A noninvasive technique of verification of embedded heat pipes in integrated satellites. In: INTERNATIONAL CONFERENCE OF HEAT PIPES FOR SPACE APPLICATIONS, 2., 2014, Moscow, Russia. **Proceedings…** Moscow, 2014.

BERTOLDO JUNIOR, J. **Estudo do desempenho de tubos de calor de alumínio ranhurados na presença de gás não condensável durante testes ambientais**. 2017. 234p. Thesis (Doctorate in Space and Technological Engineering) – National Institute of Space Research, São José dos Campos, Brasil, 2017.

BIRD, R. B.; STEWART, W. E.; LIGHTFOOT, E. D. **Transport phenomena**. 2.ed. USA: John Wiley & Sons, 2002. 897 p.

BOWMAN, W. J. **Simulated heat-pipe vapor dynamics**. 1987. Thesis (PhD) Air Force Institute of Technology, Ohio, USA, 1987.

CHI, S. W. **Heat pipe theory and practice:** a sourcebook. Washington: Hemisphere, 1976. 242 p.

COTTER, T. P. **Theory of heat pipes.** Los Alamos: [s.n.], 1965. 34 p. Report Number LA-3246-MS.

CUSSLER, E. L. **Diffusion:** mass transfer in fluid systems. 3.ed. Cambridge: Cambridge University Press, 2009. 631 p.

DAS, M. K.; MUKHERJEE, P. P.; MURALIDHAR, M. **Modeling transport phenomena in porous media with applications**. Berlin: Springer, 2017. 250 p.

EDOM, A. VLASSOV, V. V. Experimental study on periodical fluctuations of the diffuse vapor/gas front during operation of a gas-loaded heat pipe. In: INTERNATIONAL CONFERENCE ON ENVIRONMENTAL SYSTEMS, 31., 2001, Orlando, FL, USA,. **Proceedings…** 2001. p. 1-9.

EDWARDS, D. K.; MARCUS, B. D. Heat and mass transfer in the vicinity of the vapor-gas front in a gas-loaded heat pipe. **Journal of Heat Transfer**. v. 94, p. 155-162, 1972.

ENINGER, J. E.; FLEISCHMAN, G. L.; LUEDKE, E. E. **Heat pipe materials compatibility**. Ohio: [s.n.], 1976. 46 p. Report Number TRW 26148-6004-RU-00.

FAGHRI, A. Heat pipe science and technology. USA: Taylor & Francis, 1995. 874 p.

FAGHRI, A. **Analysis of frozen startup of high-temperature heat pipes and three-dimensional modeling of block heated heat pipes**. Ohio: [s.n.], 1991. 138 p. Report Number WL-TR-91-2086.

FAGHRI, A.; BUCHKO, M. Experimental and numerical analysis of low-temperature heat pipes with multiple heat sources. **Journal of Heat Transfer**, v. 113, p. 728-734, 1991.

GAUGLER, R. **Heat transfer devices.** US Patent number 2350348, 1944.

GROVER, G. M.; COTTER, T. P.; ERIKSON, F. G. Structures of very high thermal conductivity. **Journal of Applied Physics**, v. 35, p. 1990-1991, 1964.

HALL, M. L.; DOSTER J. M. A sensitivity study of the effects of evaporation/condensation accommodation coefficients on transient heat pipe modeling. **International Journal of Heat and Mass Transfer**, v. 33, p. 465-481, 1990.

HARLEY, C.; FAGHRI, A. Transient two-dimensional gas-loaded heat pipe analysis. **Transactions of the ASME**, v. 116, p. 716-723, 1994.

HE, J.; LIN, G.; BAI, L; MIAO, J.; ZHANG, H.; WANG, L. Effect of non-condensable gas on startup of a loop thermosyphons. **International Journal of Thermal Sciences**, v. 72, p. 184-194, 2013.

HE, J.; MIAO, J.; BAI, L; LIN, G.; ZHANG, H.; WEN, D. Effect of non-condensable gas on the startup of a loop heat pipe. **Applied Thermal Engineering**, v. 111, p. 1507-1516, 2017.

INCROPERA, F. P.; DEWITT, D. P.; BERGMAN, T. L.; LAVINE, A. S. **Fundamentals of heat and mass transfer**. 6.ed. USA: John Wiley & Sons, 2006. 1000 p.

ISSACCI, F.; CATTON, I.; HEISS, A.; GHONIEM N.M. Analysis of heat pipe vapor dynamics. **Chemical Engineering Communications**,. v. 85, p. 85-94, 1989.

JANG, J. H.; CHANG, W. S.; FAGHRI, A. **Analysis of transient compressible vapor flow in heat pipe**. Ohio: [s.n.], 1989. 10 p. NASA Contract Report 185119.

JANG, J. H.; CHANG, W. S.; MAHEFKEY, E. T.; FAGHRI, A. **Mathematical modeling and analysis of heat pipe startup from frozen state.** Ohio, 1989. 12 p. NASA Contract Report 185132.

KLINE, S. J.; MCCLINTOCK, F. A. Describing uncertainties in single-sample experimens. **Mechanical Engineering**, v. 75, p. 3-8, 1953.

LOBANOV, A. D.; YATSENKO, A. A.; PARFENTIEV, M. D.; BARKOVA, L. V. Life tests of aluminium axial groove heat pipes with acetone as working fluid. In: EUROPEAN SYMPOSIUM ON SPACE ENVIRONMENTAL CONTROL SYSTEMS, 4., 1991, Italy. **Proceedings…** Italy, 1991. p.583-586.

MANTELLI, M. B. H.; YAO, Q.; ANGELO, W. B.; BORGES, T. Performance of naphthalene thermosyphons with non-condensable gases: theoretical study and comparison with dat. **International Journal of Heat and Mass Transfer**, v. 53, p. 3414-3428, 2010.

MARCUS, B. D. **Theory and design of variable conductance heat pipes**. California: NASA, 1972. 252 p. NASA Report Number NASA CR-2O18.

PATANKAR, S. V. **Numerical heat transfer and fluid flow**. England: CRC Press, 1980. 214 p.

ROHANI, A. R.; TIEN, C. L. Steady two-dimensional heat and mass transfer in the vapor-gas region of a gas-loaded heat pipe. **Journal of Heat Transfer**, v. 95, p. 377-382, 1973.

REAY, D. A.; JOHNSON, M. P. The formation of diacetone alcohol during Life tests on acetone heat pipes constructed using aluminium and stainless steel. In: ESA HEAT PIPES, 2., 1991, Italy. **Proceedings…** Italy, 1991. p. 393-399.

SAAD, S. M. I.; CHING, C. Y.; EWING, D. The transient response of wicked heat pipes with non-condensable gas. **Applied Thermal Engineering.** v. 37, p. 403-411, 2012.

SAAD, S. M. I. Improved transient network model for wicked heat pipes. 2006. 134p. Thesis (Master of Applied Science) – McMaster University, Ohio, USA, 2006.

SMIRNOV, H. F.; KOCHETKOV, A.; TRETJAKOV, S. V. Express control method of heat pipe performance. In: HEAT PIPES FOR SPACE APPLICATION, 2009, Moscow, Russia. **Proceedings…** Moscow, 2009.

STUBBLEBINE, M. J.; YAO, Q.; SUPOWIT, J.; CATTON, I. A new method for evaluating heat pipe fluid compatibility. **Applied Thermal Engineering**, v. 101, p. 796-803, 2016.

TOURNIER, J. M.; EL-GENK, M. S. **“HPTAM”, a two-dimensional heat pipe analysis model, including the startup from frozen state**. New Mexico: [s.n.], 1995. 356 p. NASA Report Number NASA-CR-1999553.

TOWER, L. K.; KAUFMAN, W. B. **Accelerated life tests of specimen heat pipe from Communication Technology Satellite (CTS) project**. Ohio: [s.n.], 1977. 27 p. NASA Technical Memorandum NASA TM-73846.

VERSTEEG, H. K.; MALALASEKERA, W. **An introduction to computational fluid dynamics:** the finite volume method. 2 ed. England: Pearson Education, 2007. 517 p.

APPENDIX A: TEMPERATURE CHANGE RATES

In this appendix is presented new additional experimental results, related to heat pipe transient processes characterization by temperature rate ($℃/s$) and not by temperature (℃). Such a characterization by rate may reveal very interesting and useful results, which were not previously published by heat pipe research community, that confirmed through a wide bibliographic revision performed by author. It is expected, that the analysis of temperature change rates may increase the sensibility of detection of small amount of noncondensable gas in heat pipe, which is very important to heat pipe selection after ground storage for application in satellites.

A.1 Temperature changing rate of experimental tests with heat load of 75 W and cooled by natural and forced convection combined

Figure A.1 and Figure A.2 shows the temperature change rate during the first $1000\ s$ of the tests with heat load of $75\ W$ for pipe with and without noncondensable gas. Combination of forced and natural convection provides the cooling on the condensation zone. Both figures show the temperature change rate calculated from the raw experimental data and after analytical linear regression treatment. Thermocouple 6 and 13 have been chosen in order to take results on the middle of the natural convection zone, and on the middle of the forced convection zone.

Figure A.1 correspond to long test experimental case when heaters were keep turned on during time enough to heat pipes reach steady-state condition, and Figure A.2 corresponds to short test experimental case when heaters were switched off after $600\ s$.

First thing to note in Figure A.1 and Figure A.2 is that if we compare, the temperature change rates profiles are the same until heater is turned off at $600\ s$ of short run test. In thermocouple 6 (in the middle of natural convection zone), there is a sharp peak in the heat pipe with noncondensable gas in comparison with the heat pipe without gas. In addition, previous small periodic temperature oscillations in the condenser of heat pipe with noncondensable gas are now much more evident. The oscillations in the thermocouple 13 (forced-convection cooling zone) have a period approximately of $40\ s$. This is a relatively long period and has nothing with smallamplitude high frequency oscillations of measurement channel (thermocouples and Data Acquisition System).

As for the heat pipe without noncondensable gas, the temperature change is very similar in both condensing zones (thermocouple 6 and 13).

Figure A.1 – Temperature Change Rate of the Long Run Test, cooled by Forced Convection, with Heat Load of 75 W.

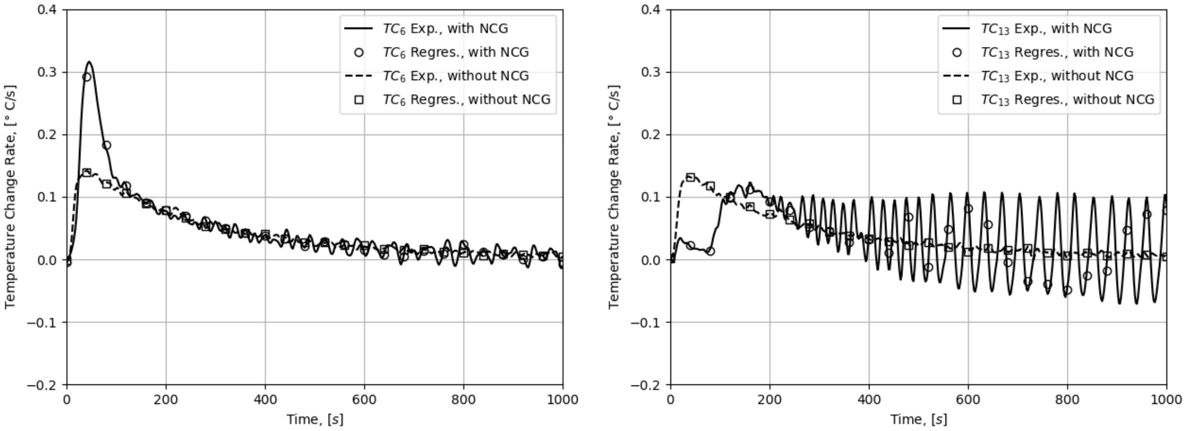

Source: The author.

Figure A.2 – Temperature Change Rate of the Short Run Test, cooled by Forced Convection, with Heat Load of 75 W.

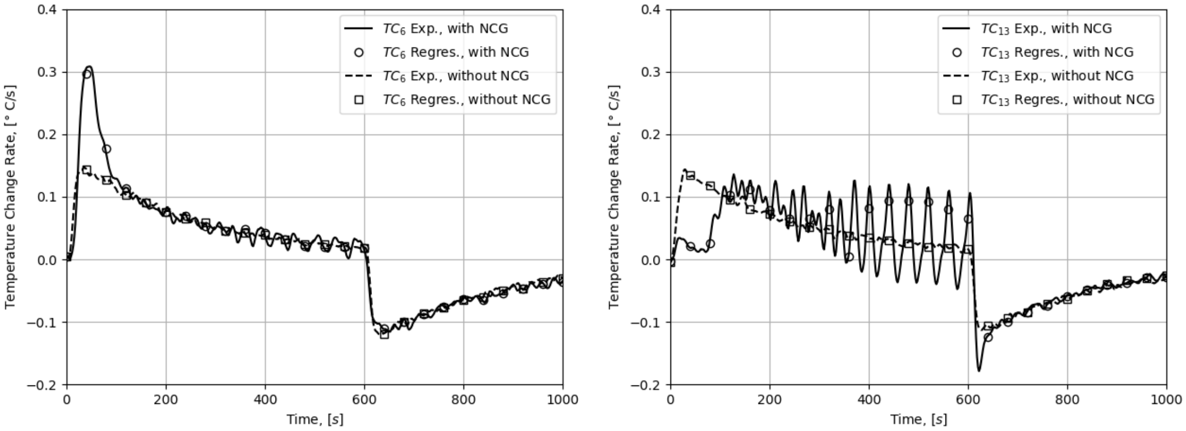

Source: The author.

Such low frequency oscillations of the temperature rates instead of temperature itself of the heat pipe with noncondensable gas was not studied previously following the performed bibliographic revision from available publications on this matter.

A.2 Temperature changing rate of experimental tests with heat load of 25 W and cooled by natural and forced convection combined

Figure A.3 and Figure A.4 shows the temperature change rate during the first $1000\,s$ of the tests with heat load of $25\,W$ for the cases of heat pipe with and without noncondensable gas cooled by a combination of natural and forced convection. Both figures show the temperature change rate calculated from the experimental data and from analytical linear regression obtained from data for two different thermocouples. Thermocouple 6 and 13.

Here again, in Figure A.3 and Figure A.4, if we compare, the temperature change rates profiles are the same until heater is turned off at $600\,s$ of short run test. But in this case, at thermocouple 6, there is no such a sharp peak in the heat pipe with noncondensable gas in comparison with the case of high heat load ($75\,W$). The temperature change rate of the heat pipe without noncondensable gas continued to be similar in thermocouple 6 and 13.

Figure A.3 – Temperature Change Rate of the Long Run Test, cooled by Forced Convection, with Heat Load of 25 W.

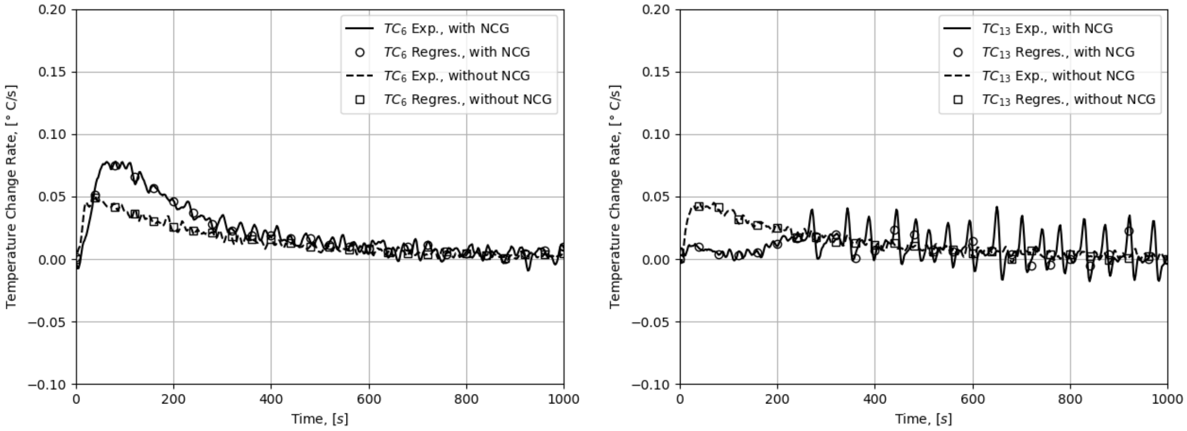

Source: The author.

Figure A.4 – Temperature Change Rate of the Short Run Test, cooled by Forced Convection, with Heat Load of 25 W.

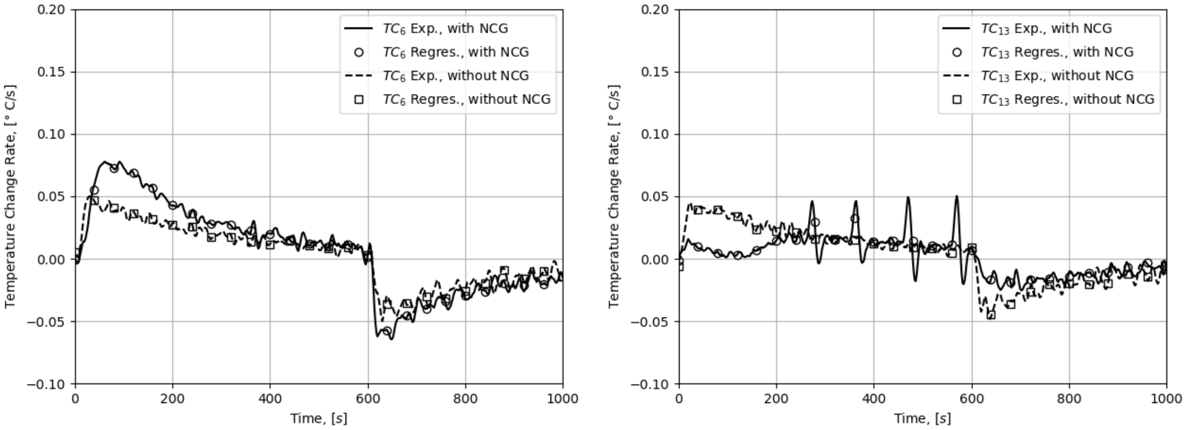

Source: The author.

Compared to the previous case of high heat load, the startup temperature rate overshoot has reduced from $0.3\ ℃/s$ down to $0.075\ ℃/s$ and becomes closer to startup rate pick of heat pipe without noncondensable gas ($0.045\ ℃/s$). The temperature rate oscillation period got an increasing from $40\ s$ (case of $75\ W$) up to $74\ s$ (present case of $25\ W$). Now, these oscillations behave like periodic pulses.

A.3 Temperature changing rate of experimental tests with heat load of 25 W and cooled by natural convection

This section present experimental results for heat pipe with and without noncondensable gas cooled purely by natural convection.

Figure A.5 presents transient data for the first $1000\ s$ of long period tests and Figure A.6 shows the temperature change rate during the first $1000\ s$ of short period tests, where heaters are switched-on for $600\ s$ and then switched-off.

Figure A.5 – Temperature Change Rate of the Long Run Test, cooled by Natural Convection, with Heat Load of 25 W.

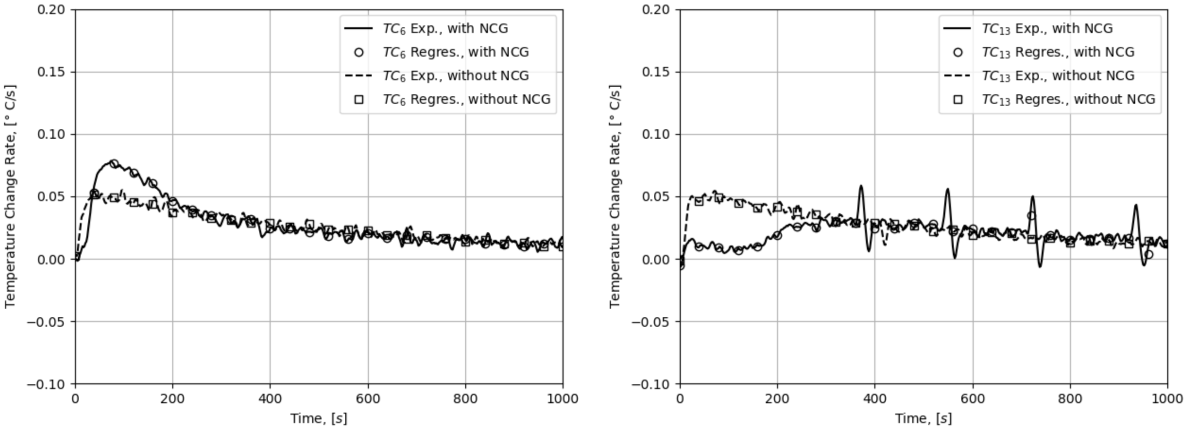

Source: The author.

Figure A.6 – Temperature Change Rate of the Short Run Test, cooled by Natural Convection, with Heat Load of 25 W.

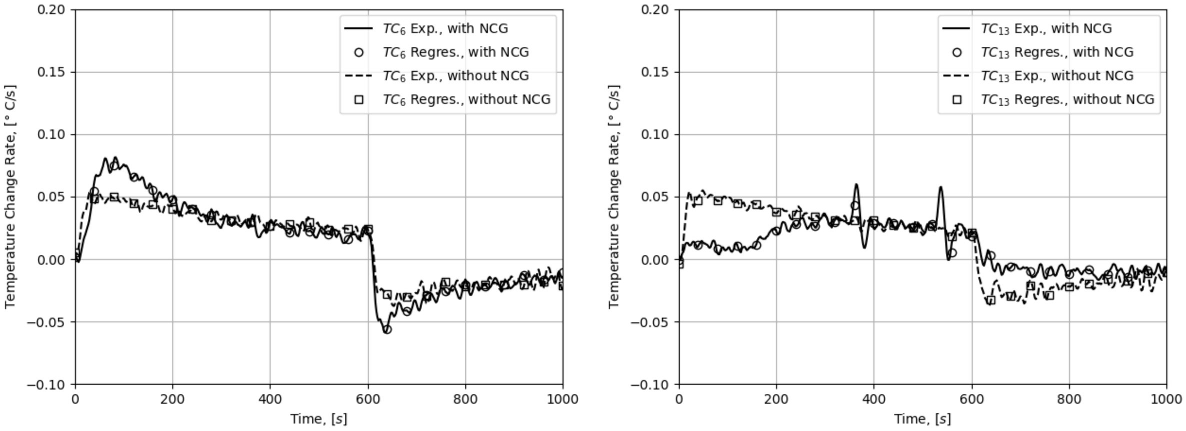

Source: The author.

Both figures show the temperature change rate calculated from the experimental data and from analytical linear regression obtained from experimental data for two different thermocouples.

Compared to the previous case of combined cooling under the same low heat load of $25\ W$, the startup temperature rate overshoot keeps the same level of 0.75 ℃/s. The difference has appeared in the temperature rate oscillation period, which has increased from $74\ s$ up to $180\ s$. These oscillations behave now as separate eventual pulses.

A.4 Time drifts of the maximum temperature change rate

In Table A.1 and Table A.2 is presented the maximum value of temperature change rate for long period ($7000\,s$ heating) and short period ($600\,s$ heating) tests respectively. Both tables shows numerically what is already shown in Figures A.1 to A.6, that there is a drift of the maximum peak when comparing heat pipe with and without noncondensable gas, for each test. It means that the condenser of heat pipe with noncondensable gas takes more time to respond an external heat load. This delay on the response takes place because the noncondensable gas partially blocks the condenser and resists the temperature raise.

Table A.1 – Values of maximum of temperature change for long period tests.

Case	TC 6		TC 13	
	Max. peak (ºC/s)	Time (s)	Max. peak (ºC/s)	Time (s)
$75W, without\ GNC, CF, Long$	0.140	42.013	0.132	44.016
$75W, with\ GNC, CF, Long$	0.313	48.038	0.117	166.035
$25W, without\ GNC, CF, Long$	0.050	44.008	0.044	72.011
$25W, with\ GNC, CF, Long$	0.077	64.027	0.033	272.002
$25W, without\ GNC, CN, Long$	0.052	40.002	0.053	74.03
$25W, with\ GNC, CN, Long$	0.078	74.036	0.051	374.029

Source: The author.

Table A.2 – Values of maximum of temperature change for short period tests.

Case	TC 6		TC 13	
	Max. peak (ºC/s)	Time (s)	Max. peak (ºC/s)	Time (s)
$75W, without\ GNC, CF, Short$	0.145	36.004	0.139	34.002
$75W, with\ GNC, CF, Short$	0.309	48.043	0.123	130.04
$25W, without\ GNC, CF, Short$	0.050	34.040	0.0425	48.017
$25W, with\ GNC, CF, Short$	0.077	68.002	0.039	472.014
$25W, without\ GNC, CN, Short$	0.051	82.041	0.053	48.022
$25W, with\ GNC, CN, Short$	0.079	84.009	0.053	366.038

Source: The author.

These delay effect can also be seen in time dependent graphs of temperature but is amplified analyzing the temperature change rates.

APPENDIX B: CALCULATION OF HEAT TRANSFER COEFFICIENTS

In this appendix is presented an example of calculation of heat transfer coefficients used in the numerical simulations. The example is shown for the case with heat input of $75\ W$ in the heaters and heat pipe being cooled by natural and forced convection. The coefficients calculated are the same presented in Table 6.2.

B.1 Heat transfer coefficient between wall and ambient on the forced convection zone

The heat transfer coefficient between wall and ambient on the forced convection zone, h_f, is calculated using the properties of air at $26\ ℃$. First, the Reynolds number is calculated for the air flow around the pipe:

$$Re = \frac{\rho_{air} u_{air} B_{side}}{\mu_{air}} = \frac{1.184\ \cdot 6.01\ \cdot 0.019}{1.85x10^{-5}} = 7308.16. \qquad \text{(B.1)}$$

The Reynolds number is used to calculate Nusselt number:

$$Nu_f = 0.102\ Re^{0.675} Pr^{1/3} = 0.102\ (7308.16)^{0.675} (0.707)^{1/3}, \qquad \text{(B.2)}$$

which is used to calculate the heat transfer coefficient on the forced convection zone:

$$h_f = \frac{Nu_f\ k_{air}}{B_{side}} = \frac{36.85 \cdot 0.0259}{0.019} = 50.23\ W/m^2K \qquad \text{(B.3)}$$

B.2 Heat transfer coefficient between wall and ambient on the free convection zone

The heat transfer coefficient between wall and ambient on the free convection zone, h_{nat}, using the properties of air at $26\ ℃$. The coefficient is calculated at each time step because its value is dependent of the difference in temperature from wall and ambient. In the example the heat transfer coefficient is calculated for temperatures in steady-state. First, the Rayleigh number is calculated with air properties at $26\ ℃$, and wall at $74\ ℃$:

$$Ra = \frac{g\beta(T_s - T_{amb})B^3}{\nu\alpha} = \frac{9.8\ \cdot \left(\frac{1}{299}\right) \cdot (347 - 299) \cdot (0.019)^3}{1.62x10^{-5} \cdot 22.39x10^{-6}} = 29750. \qquad \text{(B.4)}$$

The Rayleigh number is used to calculate the Nusselt number in each external face of the pipe. The Nusselt number for upper face:

$$Nu_{up} = 0.54\, Ra^{1/4} = 0.54 \cdot 29750^{\frac{1}{4}} = 7.09.. \tag{B.5}$$

The Nusselt number for lower face:

$$Nu_{down} = 0.27\, Ra^{1/4} = 0.27 \cdot 29750^{\frac{1}{4}} = 3.54.. \tag{B.6}$$

The Nusselt number for side faces:

$$Nu_{side} = \left\{0.825 + \frac{0.387 Ra^{1/4}}{\left[1+\left(\frac{0.492}{Pr}\right)^{9/26}\right]^{8/27}}\right\}^2 = \left\{0.825 + \frac{0.387(29750)^{1/4}}{\left[1+\left(\frac{0.492}{0.707}\right)^{9/26}\right]^{8/27}}\right\}^2 = 25.8. \tag{B.7}$$

The heat transfer coefficient is calculated using the Nusselt numbers:

$$h_{nat} = \frac{\left(Nu_{up}+Nu_{down}+2Nu_{side}\right)k_{air}}{\left(B_{up}+B_{down}+2B_{side}\right)} = \frac{(7.09+3.54+25.8)0.0259}{(0.019+0.019+2\cdot 0.019)} = 21.2\ W/m^2K. \tag{B.8}$$

B.3 Heat transfer coefficient between wick and wall

The heat transfer coefficient between wick and wall, $h_{wick,w}$, is estimated from the thermal conductivity of the wall and the distance of the centerlines of both strucutures:

$$h_{wick,w} = \frac{k_w}{\delta_{wick,w}} = \frac{180}{\left(\frac{0.00181+0.00144}{2}\right)} = 110769\ W/m^2K. \tag{B.9}$$

B.4 Heat transfer coefficient between wick and vapor

The heat transfer coefficient between wick and vapor, $h_{evap/cond}$, is estimated from the experimental wall temperatures in steady-state and is calculated for three different regions, for evaporator, for free convection zone and forced convection zone.

From the experimental results, it was calculated that from the $75\,W$ applied to the heaters, an effective power of $56.8\,W$ goes to the heat pipe. With this effective power input, the heat transfer coefficient at evaporator is calculated:

$$h_{evap/cond} = \frac{Q}{A_{wick,v}(T_{wick} - T_{mix})} = \frac{56.8}{2\pi \cdot 0.0125 \cdot 0.048\ (74.22 - 73)} = 12349\ W/m^2K. \qquad \text{(B.10)}$$

Using the heat transfer coefficient between wall and ambient at free convection zone, h_{nat}, it was calculated a heat output of $23.25\ W$ on the free convection zone, wich is used with experimental results of wall temperature to estimate the heat transfer coefficient between wick and vapor, $h_{evap/cond}$ on the free convection zone:

$$h_{evap/cond} = \frac{Q}{A_{wick,v}(T_{wick} - T_{mix})} = \frac{23.25}{2\pi \cdot 0.0125 \cdot 0.32\ (73.37 - 72.72)} = 1424\ W/m^2K. \qquad \text{(B.11)}$$

In a similar manner, the heat transfer coefficient between wick and vapor, $h_{evap/cond}$ on the forced convection zone was estimated:

$$h_{evap/cond} = \frac{Q}{A_{wick,v}(T_{wick} - T_{mix})} = \frac{33.55}{2\pi \cdot 0.0125 \cdot 0.22\ (71.35 - 69.75)} = 1214\ W/m^2K. \qquad \text{(B.12)}$$